ABSTRACT

PROTON SPIN FLIP IN THE REACTIONS $^{12}C(p,p')^{12}C^*(4.44)$ AND $^{120}Sn(p,p')^{120}Sn^*(1.17)$

By

James J. Kolata

The spin-flip probability for protons inelastically scattered from the first 2^+ state in ^{12}C and ^{120}Sn has been measured at incident proton energies of 26.2 and 40.0 MeV for ^{12}C, and 30.0 MeV for ^{120}Sn. The experimental method involved the detection of inelastically scattered protons in coincidence with de-excitation gamma radiation emitted along the normal to the scattering plane. It can be shown that this correlation is directly proportional to the spin-flip probability in the reaction.

Angular distributions were obtained over an angular range of 25° to 155° in the laboratory system for the ^{12}C target, and from 30° to 155° for the ^{120}Sn target. The data display prominent backward peaks similar to previous observations at lower energies and for other nuclei. The magnitude of this peak in the spin-flip probability was about 0.30 for ^{12}C and 0.50 for ^{120}Sn and the location of its rapidly rising edge seems to be correlated with the

target mass number. The total spin-flip probability is only about 0.03 for ^{12}C and 0.08 for ^{120}Sn despite the large backward peak in the angular distribution, because the inelastic cross section is largest at the forward angles where the spin-flip probability is small ($\lesssim$ 0.10 for both targets). Distorted-wave calculations were performed with collective-model and microscopic-model form factors in an attempt to determine the type of information about spin-dependent nucleon-nucleus forces which can be extracted from spin-flip data. The theoretical predictions were in semi-quantitative agreement with experiment at the peak of the distribution. The most serious failure in this regard occurred for the ^{12}C data at 40.0 MeV where the predicted peak spin-flip probability was 0.20 compared to the measured value of about 0.30. Larger differences were observed for the forward angle data. In the case of ^{12}C, these discrepancies were associated with the failure of the optical model for this light nucleus, and no definite conclusions could be reached regarding the spin-dependent part of the inelastic interaction. For the ^{120}Sn data, however, there is some evidence that the observed discrepancies are related to the spin-dependence of the inelastic interaction. If this is the case, a more adequate treatment of this interaction may significantly improve the agreement between theory and experiment.

PROTON SPIN FLIP IN THE REACTIONS $^{12}C(p,p')^{12}C^{*}(4.44)$ AND $^{120}Sn(p,p')^{120}Sn^{*}(1.17)$

By

James J. Kolata

A THESIS

Submitted to
Michigan State University
in partial fulfillment of the requirements
for the degree of

DOCTOR OF PHILOSOPHY

Department of Physics

1969

ACKNOWLEDGMENTS

I wish to express my deepest appreciation to my thesis adviser, Dr. Aaron Galonsky, for his guidance and continuing help and encouragement throughout the course of this work.

I am grateful to Dr. Barry Preedom for his invaluable assistance in the optical-model analysis, and for a careful and critical reading of this paper.

To the members of the Cyclotron Laboratory technical staff, and especially to Mr. Norval Mercer, go my thanks for their assistance in the design and construction of much of the apparatus used in the course of this experiment.

Special thanks go to Richard Howell and Ronald Sager for their help in taking the data, and to Dr. Hugh McManus and the members of the professional staff of the Cyclotron Laboratory for their helpful advice and assistance.

I also acknowledge the financial support of the National Science Foundation for the experimental program, and for the personal support provided by a two-year Co-operative Graduate Fellowship.

Very special thanks go to my wife, Ann, for her encouragement, understanding, and support during the past year, and for typing this thesis.

TABLE OF CONTENTS

LIST OF TABLES

Table

LIST OF FIGURES

Figure

CHAPTER I

INTRODUCTION

Several experimental techniques are available for studying the spin dependence of the nucleon-nucleus reaction. In particular, one might investigate the inelastic scattering of polarized protons (Fr 67,Gl 67) or the effects of target polarization on a given reaction (Go 62). Either of these methods involves the preparation of an initial system with known spin orientation; the relative scarcity of such data reflects the experimental difficulties encountered. Alternatively, it is possible to determine the angular dependence of polarization of the residual nucleus, when the initial system is completely unpolarized. Usually, one observes the angular correlation involving the scattered particle and the de-excitation gamma radiation. It can be shown (Go 62,Sa 64), in the context of the distorted-wave Born approximation (DWBA) with unique total transferred angular momentum, that the information obtained by this method is the same as that obtained by scattering from polarized targets. Therefore, such measurements can provide valuable data concerning the spin dependence of nuclear reaction mechanisms for the wide range of nuclei for which polarized targets are unavailable (as, for example, if the nucleus to be studied has zero ground state spin). In addition, they can provide supplementary information in those cases for which the inelastic scattering of polarized protons has been measured. The chief disadvantage of the method lies in the need to perform a coincidence experiment.

The angular correlation function for the case in which gamma radiation is detected in the plane determined by the incident beam and the scattered particle (in-plane correlation) has been analyzed in the DWBA by several authors (Sa 55, Bl 61, Ba 57). Banerjee and Levinson (Ba 57) predicted the form:

$$W(\theta_\gamma) = A + B\sin^2 2(\theta_\gamma - \epsilon_1) + C\sin^2(\theta_\gamma - \epsilon_2) \quad (I.1)$$

and associated the last term with the presence of spin flip in the interaction. Such a term has been observed (Yo 60, Br 61), but it has proved to be very difficult to extract the relevant spin-flip probability, which is expected to be quite sensitive to the spin dependence of the nucleon-nucleus interaction.

Recently, Schmidt et.al. (Sc 64) have pointed out that spin flip could be more easily studied through an angular correlation in which the gamma radiation is detected along the normal to the scattering plane (gamma-perpendicular correlation). They were able to show that this correlation is directly proportional to the spin-flip probability for the case of a $0^+ - 2^+$ transition, independent of the reaction mechanism assumed. The argument may be extended with minor modification to the excitation of a $1^\pm$ or 2^- state from a 0^+ ground state.

We have used this method to investigate proton spin flip in the excitation of the first 2^+ state of ^{12}C and ^{120} Sn. These targets were chosen for several reasons. First of all, ^{12}C is a nominally 'closed shell' nucleus on which numerous theoretical calculations have been done. In addition, the relatively small number of open reaction channels and the well-separated energy levels are non-trivial experimental advantages. Unfortunately, ^{12}C is also a notoriously poor 'optical-model' nucleus, in that it is extremely difficult to extract optical model parameters which accurately describe the elastic scattering (Sa 67). When it became clear that good optical parameters were necessary for the interpretation of the data, it was decided to investigate ^{120}Sn which is not plagued by this problem, though it is experimentally more difficult because of the high background of gamma radiation from various reactions in the target.

The data have been analyzed in the DWBA, with several different reaction models, in an attempt to determine the type of information about spin-dependent nucleon-nucleus forces which can be extracted from spin-flip measurements. Chapter II is devoted to a discussion of the DWBA method, and of the particular reaction models used. The experimental method and techniques are described in Chapter III, followed by a short discussion of the optical model and the extraction of the parameters in Chapter IV. The theoretical predictions are compared to the experimental data in Chapter V, and the resulting conclusions which can be reached from this comparison regarding the value of spin-flip measurements in the investigation of spin-dependent forces are summarized in Chapter VI.

CHAPTER II

DWBA THEORY OF ANGULAR CORRELATIONS

The theoretical formalism of the distorted-wave Born approximation (DWBA) for inelastic scattering has been treated in detail by Satchler (Sa 64) and by Tobocman (To 61). The basic assumption made in the development of the theory is that of 'weak coupling'; that is, it is assumed that elastic scattering is the most important process that occurs, and that the inelastic event can be treated as resulting from a perturbation which causes transitions between elastic scattering states. The elastic scattering itself is treated 'exactly', in the sense that it is calculated from an optical model potential using parameters which fit the elastic data.

In the following sections, some of the more important results in the development of the DWBA theory, and its application to the prediction of angular correlations, are discussed. The treatment followed is that due to Satchler (Sa 64).

II.A. Transition Amplitude

II.A.1. General Form of the Transition Amplitude for Inelastic Scattering

In the DWBA theory of inelastic scattering, the transition amplitude takes the form:

$$T_{fi} = J \sum_{\substack{m_i m_f \\ m_i' m_f'}} \iint \chi^{(-)*}_{m_f' m_f}(\vec{k}_b, \vec{r}_b) \langle \psi_f | V | \psi_i \rangle \chi^{(+)}_{m_i' m_i}(\vec{k}_a, \vec{r}_a)\, d\vec{r}_a\, d\vec{r}_b \qquad \text{(II.1)}$$

where $\vec{r}_a$ and $\vec{r}_b$ are the coordinates of the projectile relative to the target in the initial and final state, and J is the Jacobian of the transformation to these coordinates.

The functions χ_i and χ_f are the distorted waves, which are eigenstates of elastic scattering from the target in its initial and final states, respectively. They are usually generated from an optical model potential using parameters which fit the elastic scattering data (see Chapter IV). The superscript (+) or (-) denotes outgoing or incoming boundary conditions, and the subscript m refers to the z-component of the projectile spin. The two boundary conditions are related by time reversal invariance:

$$\chi^{(-)*}_{m'm}(\vec{k}, \vec{r}) = (-)^{m-m'} \chi^{(+)}_{-m',-m}(-\vec{k}, \vec{r}) \qquad \text{(II.2)}$$

Since the spin-orbit term in the usual optical model potential (see Chapter IV) can couple different spin projections, the distorted waves are, in general, non-diagonal matrices in spin space. The off-diagonal terms ($m \neq m'$) can lead to a nonzero spin-flip amplitude.

The remaining factor in the expression for the transition amplitude is the matrix element of the interaction causing the transition, taken between the initial and final internal states of the scattering system. It contains all of the information about the structure of these states and the mechanism which couples them, and can be looked upon as producing transitions between the elastic scattering eigenstates χ_i and χ_f . Since this matrix element will, in general, be spin dependent, it can also couple different spin projections and therefore produce a nonzero spin-flip amplitude.

II.A.2. Zero-Range Approximation

The general form of the transition amplitude (II.1) involves a six dimensional integration over the space of $\vec{r}_a$ and $\vec{r}_b$. Since the numerical evaluation of such an integral is difficult and time consuming, the 'zero-range' approximation is usually introduced. The physical assumption behind this approximation is that the scattered particle is emitted at the same point at which the incident particle is absorbed, so that $\vec{r}_b = (\frac{A}{B})\,\vec{r}_a$ (where A and B are the masses of the target nucleus in the entrance and exit channel). The introduction of the zero-range approximation reduces the transition amplitude to a three-dimensional integral which is much easier to compute. The price paid for this simplification is that the effects of particle exchange are neglected, and possible nonlocal inelastic interaction potentials cannot be introduced exactly. However, both these cases can be treated in some approximation by replacing the interaction potential by an equivalent local but momentum dependent pseudo-potential (Pe 64).

II.A.3. Reduced Amplitudes

The transition amplitude T_{fi} is usually expanded in terms of 'reduced amplitudes' corresponding to the transfer of a definite total angular momentum $\vec{j}$, orbital angular momentum $\vec{l}$, and spin angular momentum $\vec{s}$ to the nucleus during the inelastic event. In the zero-range approximation, this expansion takes the form:

$$T_{fi} = \sum_{\substack{lsj \\ m\, m_i\, m_f}} (2j+1)^{1/2} \langle J_i\, j\, M_i\,, M_f - M_i | J_f M_f \rangle\, \beta_{lsj}^{m\, m_f\, m_i}(\vec{k}) \qquad \text{(II.3)}$$

where $m = M_f - M_i + m_f - m_i$, and J and M are the total angular momentum of the target nucleus, and its z-component. The expression for the reduced amplitude $\beta_{lsj}^{m\, m_f\, m_i}$ in terms of previously defined quantities appears in Ref. (Sa 64).

The transferred angular momenta $(\vec{l}, \vec{s}, \vec{j})$ are determined from the relationships:

$$\vec{j} = \vec{J}_f - \vec{J}_i \qquad \vec{s} = \vec{s}_i - \vec{s}_f \qquad \vec{l} = \vec{j} - \vec{s}$$

and, in the zero-range approximation: (II.4)

$$\pi_i \pi_f = (-)^{l}$$

where the transition is $(J^{\pi})_i \rightarrow (J^{\pi})_f$ and $\vec{s}_i(\vec{s}_f)$ is the spin of the incident (scattered) particle. It is important to notice that the value of each of these angular momenta during the inelastic event is to be used; this is not necessarily the same as the asymptotic value. For example, a reduced amplitude labeled by s=0 may still contribute to spin flip (s=1 asymptotically) through the distortions introduced into χ_i and χ_f by the spin-orbit term in the optical potential.

II.B. Cross Sections, Polarization, and Angular Correlation

II.B.1. Scattering Cross Section, and the Polarization of the Scattered Particles

The differential cross section for an unpolarized projectile and target is proportional to the square of the transition amplitude and can be written in terms of the reduced amplitudes as:

$$\frac{d\sigma}{d\Omega}(\theta) = \frac{\mu_a \mu_b}{(2\pi \hbar^2)^2} \frac{k_b}{k_a} \frac{2J_f+1}{(2J_i+1)(2S_i+1)} \sum_{\substack{j \\ m m_f m_i}} \left| \sum_{ls} \beta_{lsj}^{m m_f m_i} \right|^2 \qquad \text{(II.5)}$$

where μ_a and μ_b are the reduced masses in the entrance and exit channels. Note that the sum on j is incoherent, although the possibility of interference terms between different l and s remains.

The vector polarization of the scattered particle is defined as the expectation value $\langle \hat{s}_f \rangle / s_f$. If the z-axis is chosen along $\vec{k}_a$ and the y-axis along $\vec{k}_a \times \vec{k}_b$, the expression for the polarization is:

$$P(\theta) = \frac{\sum[(s_f - m_f)(s_f + m_f + 1)]^{\frac{1}{2}}\ \mathcal{I}m\left[\beta_{\ell s j}^{m\, m_f\, m_i}\left(\beta_{\ell' s' j}^{m+1,\, m_f+1,\, m_i}\right)^{*}\right]}{s_f \sum \beta_{\ell s j}^{m\, m_f\, m_i}\left(\beta_{\ell' s' j}^{m\, m_f\, m_i}\right)^{*}} \qquad \text{(II.6)}$$

where the sums are taken over l,l',s,s',j, and all the projection quantum numbers. Here again the coherent sum on l and s appears.

The differential cross section for the inelastic scattering was calculated using a computer code written by T. Tamura and R.M. Haybron of the Oak Ridge National Laboratory. This code was modified to perform additional calculations and was reprogrammed to run on the Σ 7 computer at the cyclotron laboratory. In the final version, an option allowing the coherent sum over l and s was implemented, and the expression (II.6) for the polarization was programmed. In addition, a subroutine to calculate the spin flip was added; this particular routine will be briefly described below.

II.B.2. <u>Statistical Tensors</u>

It is convenient to describe the polarization of the residual nucleus in terms of the density matrix (Br 62) in M_f for the residual nuclear spin, which is constructed from the reaction amplitudes:

$$\rho_{M_f M_f'} = \sum_{m_i m_f M_i} T_{fi}(m_i M_i m_f M_f)\ T_{fi}^{*}(m_i M_i m_f M_f') \qquad \text{(II.7)}$$

This in turn may be expanded in polarization moments or 'statistical tensors' ρ_{KQ} of rank K $\leq 2J_f$:

$$\rho_{M_f M_f'} = \sum_{KQ} (-)^{J_f - M_f + Q} \langle J_f J_f M_f, Q-M_f | KQ \rangle \rho_{KQ} \qquad \text{(II.8)}$$

After a moderate amount of algebra, we find for the statistical tensors:

$$\rho_{KQ} = (2J_f+1) \sum_{\substack{\ell s j \\ \ell' s' j' \\ m\, m_f\, m_i}} (-)^{J_f - J_i + j + j' - K + Q - \mu} \sqrt{(2j+1)(2j'+1)}\; W(jj'J_fJ_f;KJ_i)$$

$$\times \langle jj'\mu, Q-\mu | KQ \rangle \beta_{\ell s j}^{m m_f m_i} \left(\beta_{\ell' s' j'}^{m-Q, m_f m_i}\right)^* \qquad \text{(II.9)}$$

where $\mu = m+m_i-m_f$. In contrast to the expressions for the differential cross section and polarization, the sum on j is coherent, so that amplitudes with different total transferred angular momenta can interfere.

The ρ_{KQ} are constructed so as to behave under rotations like spherical tensors of rank K. In addition, when referred to $\vec{k}_a$ as the z-axis and $\vec{k}_a \times \vec{k}_b$ as the y-axis, they satisfy the symmetry relation:

$$\rho_{KQ} = (-)^{K-Q} \rho_{K,-Q} \qquad \text{(II.10)}$$

so that the ρ_{KQ} are real (imaginary) for K even (odd). In particular, ρ_{K0} vanishes for K odd.

The spin-flip subroutine calculates the ρ_{KQ} for unique total transferred angular momentum $j \leq 2$ and the possibility of coherent sums on l and s is retained. Thus, it is sufficiently general for inelastic proton scattering to a 2^+ level from a 0^+ ground state, where the only allowed values of the transfer quantum numbers are $(l,s,j) = (202)$ or (212) (see II.4 above). The statistical tensors are computed for all K,Q satisfying:

$$0 \leq K \leq 2J_f \qquad \text{(II.11)}$$
$$-K \leq Q \leq K$$

Therefore, the accuracy of the calculation may be checked by verifying that the symmetry relation (II.10) is obeyed.

II.B.3. Angular Correlation Function and Spin Flip

The angular correlation of the de-excitation gamma radiation with respect to the direction of the scattered particle has the form (Sa 60, Br 62, Go 62):

$$W(\theta\phi, \theta_\gamma \phi_\gamma) = \sum_{KQ} \sqrt{\frac{4\pi}{2K+1}}\, \rho_{KQ}\, F_K\, Y_K^Q(\theta_\gamma, \phi_\gamma) \qquad \text{(II.12)}$$

where Y_K^Q is the usual spherical harmonic. The parameters F_K can be written in terms of tabulated (Bi 53) correlation coefficients:

$$F_K = \sum_{LL'} C_L C_{L'} F_K(LL' J_c J_f) \qquad \text{(II.13)}$$

Here, J_c is the nuclear spin after the emission of the gamma ray and L,L' are its multipole orders. C_L is the probability amplitude for 2^L - pole emission and the normalization is:

$$F_0 = \sum_L |C_L|^2 = 1 \tag{II.14}$$

The spin flip subroutine calculates $W(\Theta, 0^\circ, 90^\circ, 90^\circ)$ for the case of a $2^+ - 0^+$ transition. Only one multipole order ($l=2$) can contribute, so that the computation of F_K is considerably simplified. The spin-flip probability is directly proportional to this correlation. The constant of proportionality is derived in Appendix B.

II.C. Nuclear Reaction Models

The model dependence of the DWBA transition amplitude is contained in the matrix element of the interaction potential V taken between the wave function for the internal states of the colliding pair. If V is static (i.e., if it is local and does not contain gradient operators), it may be expanded in a multipole series of the form (Sa 66):

$$V(\vec{r}, \xi_a, \xi_A) = \sum_{\ell s j, \mu} (-)^{j-\mu} V_{\ell s j, \mu}(r, \xi_A)\, T_{\ell s j, -\mu}(\theta\phi, \xi_a) \tag{II.15}$$

where ξ_A represents the internal coordinates of the target, and ξ_a those of the projectile. The 'spin-angle' tensor T is given by:

$$T_{\ell s j, \mu}(\theta\phi, \xi_a) = \sum_m \langle \ell s\, m, \mu-m | j\mu \rangle Y_\ell^m(\theta\phi)\, S_{s, \mu-m}(\xi_a) \tag{II.16}$$

where S_s is a tensor of rank s in the projectile spin space (for inelastic proton scattering, s=0 or 1). Taking the matrix element of V, we get (Sa 66):

$$< s_i m_f J_f M_f | V | s_i m_i J_i M_i > = \sum_{\ell s j, \mu} F_{\ell s j}(r) \, Y_\ell^{m*}(\theta\phi)$$

$$\times (-)^{s_i - m_f} < s_i s_i m_i, -m_f | s, m_i - m_f > \qquad \text{(II.17)}$$

$$\times < J_i j M_i, M_f - M_i | J_f M_f > < \ell s m, m_i - m_f | j M_f - M_i >$$

where the dependence on the projection quantum numbers has been factored out using the Wigner-Eckart theorem. The radial function $F_{lsj}(r)$, or 'form factor', contains the reduced matrix elements of the interaction:

$$F_{\ell s j}(r) = \sqrt{\frac{2s_i+1}{2s+1}} < s_i \| S_s \| s_i > < J_f \| V_{\ell s j}(r) \| J_i > \qquad \text{(II.18)}$$

The form factor is to be computed in the context of a particular reaction model. In the present section, we discuss three models which have been used to interpret the experimental data. The first of these is a collective model in which the nuclear wave functions are taken to be the rotational eigenstates of the total angular momentum of the nucleus, and the interaction is generated from a deformed optical model potential. The other two are microscopic models, in which the nuclear wave functions are shell model states and the effective interaction potential is the sum of two-body forces.

II.C.1. Collective Model

We consider first the spin-independent term in the optical potential; in this case, only the spin-independent (s=0) form factor is nonvanishing. It is assumed that the potential depends only on the distance from the nuclear surface, which is allowed to be nonspherical. Let the nuclear surface be defined in body-fixed axes by r = $R(\theta', \phi')$ and expand in spherical harmonics:

$$V = V(r - R(\theta', \phi')) = V\left(r - R_o[1 + \sum_{\ell m} a_{\ell m} Y_\ell^m(\theta'\phi')]\right) \tag{II.19}$$

The multipole order of the deformation is determined by the quantum number l. For an axially symmetric deformation, the only nonvanishing parameter is $a_{\ell o} \equiv \beta_\ell$.

The next step is to expand the potential in a Taylor series about R = R_0:

$$V = V(r - R_o) - \delta R \frac{d}{dr} V(r - R_o) + \cdots$$

where: (II.20)

$$\delta R = R_o \sum_{\ell m} a_{\ell m} Y_\ell^m(\theta'\phi')$$

The first term in (II.20) is the spherical optical potential which describes the elastic scattering. In the first approximation, the interaction is taken to be that part of the expansion which occurs to first order in the deformation parameters:

$$V_{int.} = -R_0 \frac{dV(r-R_0)}{dr} \sum_{\ell m} a_{\ell m} Y_\ell^m(\theta'\phi') \qquad \text{(II.21)}$$

We now compare with (II.15), which, in the special case s=0, takes the form:

$$V_{int.} = \sum_{\ell\mu} (-)^{\ell-\mu} V_{\ell o \ell,\mu} Y_\ell^{-\mu}(\theta\phi) \qquad \text{(II.22)}$$

Let R be the rotation which takes body-fixed axes ($\theta' \phi'$) into space-fixed axes (θ ϕ). The transformation is (Ba 62):

$$Y_\ell^m(\theta\phi) = \sum_{m'} D^\ell_{m'm}(R) Y_\ell^{m'}(\theta'\phi') \qquad \text{(II.23)}$$

where D is the usual rotation matrix. Substituting into (II.22):

$$V_{int.} = \sum_{\ell\mu m} (-)^{\ell-\mu} V_{\ell o \ell,\mu} D^\ell_{m,-\mu} Y_\ell^m(\theta'\phi') \qquad \text{(II.24)}$$

Comparing with (II.21) above:

$$\sum_\mu (-)^{\ell-\mu} V_{\ell o \ell,\mu} D^\ell_{m,-\mu} = -R_0 \frac{dV(r-R_0)}{dr} a_{\ell m} \qquad \text{(II.25)}$$

Using the orthogonality relation $\sum_q D^\ell_{qm} D^{\ell *}_{qm'} = \delta_{mm'}$:

$$V_{\ell o \ell,\mu} = -\left[(-)^{\mu-\ell} \sum_m a_{\ell m} D^{\ell *}_{m,-\mu}\right] R_0 \frac{dV(r-R_0)}{dr} \qquad \text{(II.26)}$$

Finally, we have the symmetry relation $D^{\ell *}_{mm'} = (-)^{m-m'} D^{\ell}_{-m,-m'}$ and, since l is integral:

$$V_{\ell 0\ell,\mu} = -\left[\sum_m (-)^{\ell+m} a_{\ell m} D^{\ell}_{-m,\mu}\right] R_0 \frac{dV(r-R_0)}{dr} \qquad \text{(II.27)}$$

The form factor is proportional to the reduced matrix element of (II.27) taken between the initial and final nuclear states. Here, we shall only consider axially symmetric states, for which the wave function is (Ba 62,Da 58):

$$\psi_{JM} = \sqrt{\frac{2J+1}{8\pi^2}}\, D^{J}_{0M} \qquad (J=0,2,4,\cdots) \qquad \text{(II.28)}$$

The matrix element of $V_{101,\mu}$ between states with spin J_i and J_f is:

$$\begin{aligned}\langle J_f M_f | V_{\ell 0\ell,\mu} | J_i M_i\rangle &= \frac{(-)^{\ell+1}}{8\pi^2}\beta_\ell R_0 \frac{dV(r-R_0)}{dr}\sqrt{(2J_i+1)(2J_f+1)} \\ &\quad \times \int D^{J_f *}_{0M_f} D^{\ell}_{0\mu} D^{J_i}_{0M_i}\, d\Omega \qquad \text{(II.29)} \\ &= (-)^{J_i-J_f+1}\beta_\ell R_0 \frac{dV(r-R_0)}{dr}\langle \ell J_i 0 0 | J_f 0\rangle\langle J_i \ell M_i \mu | J_f M_f\rangle\end{aligned}$$

For even-even nuclei, $J_i=0$ and:

$$\langle J_f \| V_{\ell 0\ell} \| 0\rangle = -\frac{\beta_\ell R_0}{\sqrt{2\ell+1}}\frac{dV(r-R_0)}{dr} \qquad (\ell=0,2,4\cdots) \qquad \text{(II.30)}$$

Hence, the final expression for the collective model form factor:

$$F_{\ell 0 \ell}(r) = -\sqrt{\frac{2}{2\ell+1}}\;\beta_\ell R_0 \frac{dV(r-R_0)}{dr} \qquad (\ell = 0,2,4\cdots) \tag{II.31}$$

It has been customary to deform only the real part of the optical potential (Ba 62a); more recent studies (Fr 67,Gl 67), however, indicate that the imaginary terms must also be deformed to account for the observed polarization in inelastic proton scattering. A Fortran IV code has been written (Lo 68) to compute this (complex) form factor from optical model parameters which fit the elastic scattering data. The deformation parameter β_ℓ is treated as an arbitrary normalization constant, which is assumed to be the same for both the real and imaginary parts of the optical model potential.

In the previous discussion, we have considered only the spin-independent part of the interaction. It is possible to introduce spin dependence by deforming the spin-orbit term in the optical potential. The resulting interaction is extremely difficult to handle (Sa 66) since it is nonstatic (gradient operators appear in the expansion of $\vec{L}\cdot\vec{S}$). For this reason, all of the collective model results were computed with spin-independent interactions, which contribute no s=1 amplitude. In this model, then, the entire spin-flip cross section is due to spin-orbit distortions in the elastic channel wave functions.

II.C.2. Microscopic Models

Assuming that the projectile interacts with the target through a sum of two-body forces, and that multiple scattering processes are unlikely, the interaction potential may be written (Sa 66):

$$V = \sum_i v_{ip} - U \tag{II.32}$$

where U is the optical model potential which generated the distorted waves, and v_{ip} is the two-body interaction between the projectile and the i^{th} target nucleon. Furthermore, v_{ip} is usually approximated by (Sa 67a,Ke 59,Jo 66):

$$v_{ip} = V_0(|\vec{r}_i - \vec{r}_p|) + V_1(|\vec{r}_i - \vec{r}_p|)\,\vec{\sigma}_i \cdot \vec{\sigma}_p \tag{II.33}$$

where $\vec{\sigma}_i\ (\vec{\sigma}_p)$ is the spin operator for the target (projectile) nucleon. This expression neglects the tensor and spin-orbit forces known to be present in the interaction between free nucleons (La 62,Ha 62). The main justification for this truncation is simplicity; non-central two body forces are much more difficult to work with (Sa 66).

Equation (II.33) can be written in terms of the spherical tensor $\widetilde{S}$, where $S_0 = 1$ and $\vec{S}_1 = \vec{\sigma}$:

$$v_{ip} = \sum_{s\lambda} (-)^{\lambda} S_{s\lambda}^{(i)} S_{s,-\lambda}^{(p)} V_s(|\vec{r}_i - \vec{r}_p|) \tag{II.34}$$

The radial dependence of the interaction potential may now be expanded in multipoles:

$$V_s(|\vec{r}_i - \vec{r}_p|) = \sum_{lm} V_{ls}(r_i, r_p)\, Y_{lm}(\hat{r}_i)\, Y^*_{lm}(\hat{r}_p) \qquad \text{(II.35)}$$

Substituting this result into (II.15) and applying the definition (II.16) of the spin-angle tensor T_{lsj}, the two-body potential becomes:

$$\mathcal{V}_{ip} = \sum_{lsj,\mu} (-)^{j-\mu}\, V_{ls}(r_i, r_p)\, T^{(i)}_{lsj,\mu}\, T^{(P)}_{lsj,-\mu} \qquad \text{(II.36)}$$

The form factor is then obtained from (II.17) and (II.18):

$$F_{lsj}(r_p) = \sqrt{2}\, \langle J_f \| \sum_i V_{ls}(r_i, r_p)\, T^{(i)}_{lsj} \| J_i \rangle \qquad \text{(II.37)}$$

In order to calculate the form factor from (II.37), it is necessary to determine the initial and final state nuclear wave functions, and the interaction potentials $V_{ls}(r_i, r_p)$, from some nuclear models. The interaction potentials will be discussed in this section, and the discussion of the nuclear wave functions will be deferred to the next section.

Two different interaction potentials were used in the calculation of the form factor. The first of these was a Yukawa interaction:

$$V_s(|\vec{r}_i - \vec{r}_p|) = V_s\left(e^{-m_s R}/m_s R\right) \quad (R = |\vec{r}_i - \vec{r}_p|) \qquad \text{(II.38)}$$

where the strength V_s and the inverse range m_s were determined in the impulse approximation by McManus and Petrovich (Mc 67,Pe 67). They fitted the Fourier transform of a single Yukawa to the nucleon-nucleon scattering amplitude calculated from the central part of the Hamada-Johnson potential (Ha 62). The interaction so determined is complex and spin-dependent, and both the range and strength parameters vary with the incident proton energy. The particular virtue of the Yukawa-type interaction is that a closed form for the multipole expansion exists (Me 65):

$$e^{-m_s R}/m_s R = 4\pi i \sum_{\ell m} j_\ell(i m_s r_<)\, h_\ell^{(+)}(i m_s r_>)\, Y_{\ell m}(\hat{r}_i)\, Y^*_{\ell m}(\hat{r}_p) \qquad \text{(II.39)}$$

where j_l and h^+_l are the spherical Bessel and Hankel functions, $r_>(r_<)$ refers to the greater (lesser) of r_i and r_p, and $R = |\vec{r}_i - \vec{r}_p|$. Then:

$$V_{\ell s}(r_i, r_p) = 4\pi i\, V_s\, j_\ell(i m_s r_<)\, h_\ell^{(+)}(i m_s r_>) \qquad \text{(II.40)}$$

The second form for the interaction potential was derived by McManus and Petrovich (Mc 69) from the Kallio-Kolltveit shell-model effective interaction (Ka 64). The resulting interaction was real, spin-dependent, and independent of energy. In addition, it also included a factor depending on the two-thirds power of the nuclear matter density, which seems to improve the agreement between theory and experiment (Gr 67,La 67). The radial dependence is an exponential form, so that the multipole expansion is somewhat more complicated. For an arbitrary function of $R = |\vec{r}_i - \vec{r}_p|$:

$$V_s(R) = \frac{1}{4\pi} \sum_{\ell} (2\ell+1)\, V_{\ell s}(r_i, r_p)\, P_\ell(\cos\alpha) \qquad \text{(II.41)}$$

where α is the angle between $\hat{r}_i$ and $\hat{r}_p$. Using the properties of the Legendre polynomials (Me 65):

$$\begin{aligned} \int P_{\ell'}(\cos\alpha)\, V_s(R)\, d(\cos\alpha) &= \frac{1}{4\pi} \sum_{\ell} (2\ell+1)\, V_{\ell s}(r_i, r_p) \int P_\ell(\cos\alpha)\, P_{\ell'}(\cos\alpha)\, d(\cos\alpha) \qquad \text{(II.42)} \\ &= \frac{1}{2\pi} V_{\ell s}(r_i, r_p) \end{aligned}$$

Next, make a change of variable, noting that $R = (r_i^2 + r_p^2 - 2 r_i r_p \cos\alpha)^{\frac{1}{2}}$:

$$V_{\ell s}(r_i, r_p) = \frac{2\pi}{r_i r_p} \int_{|r_i - r_p|}^{r_i + r_p} P_\ell(R)\, V_s(R)\, R\, dR \qquad \text{(II.43)}$$

Thus, the evaluation of the multipole coefficients of the potential introduces an additional integration which must be performed numerically. A computer code has been written (Pe 68) to calculate the form factor in this case.

II.C.3. Nuclear Wave Functions

The excited states of doubly-closed-shell nuclei such as ^{12}C may be expressed as coherent superpositions of particle-hole states obtained by promoting a nucleon from a closed shell j_h to an empty shell j_p. We define the particle-hole state by (Sa 66):

$$\begin{aligned} |(j_h^{-1} j_p) JM\rangle = \sum_m &\langle j_h\, j_p\, M-m, m | JM\rangle \qquad \text{(II.44)} \\ &\times (-)^{j_h + M - m}\, a_{j_h, m-M}\, a^{+}_{j_p m} |0\rangle \end{aligned}$$

where $|0\rangle$ is the particle-hole vacuum wave function and a^+_{jm} (a_{jm}) creates (destroys) a particle in the shell model orbital j,m. The excited state $|JM\rangle$ is then:

$$|JM\rangle = \sum_{j_h j_p} C_{j_h j_p} \, |(j_h^{-1} j_p) JM\rangle \tag{II.45}$$

where the coefficient $C_{j_h j_p}$ is the amplitude for the corresponding particle-hole pair in the excited state wave function. The amplitudes we used were those computed in the random phase approximation (RPA) by Gillet and Vinh Mau (Gi 64), which include the effects of ground state correlations.

The form factor is proportional to the reduced matrix element:

$$M = \langle J_f \| \sum_i V_{ls} T_{lsj}(i) \| 0\rangle \tag{II.46}$$

In second quantization notation:

$$\sum_i V_{ls} T_{lsj}(i) = \sum_{\alpha\beta} \langle j_\beta m_\beta | V_{ls} T_{lsj} | j_\alpha m_\alpha \rangle a^+_{j_\beta m_\beta} a_{j_\alpha m_\alpha} \tag{II.47}$$

where the summation extends over all shell-model states. Taking the matrix element of this operator between the states (II.45), and using the commutation properties of the creation-annihilation operators (DeB 64), one obtains:

$$M = \sum_{j_h j_p} \hat{j}_h \hat{j}^{-1} C_{j_h j_p} \langle j_h \| T_{lsj} \| j_p \rangle \langle j_h | V_{ls}(r_i, r) | j_p \rangle \tag{II.48}$$

where $\hat{j} = \sqrt{2j+1}$. Expressions for the single-particle matrix elements $\langle j_h \| T_{lsj} \| j_p \rangle$ are found in Satchler (Sa 66). The radial integrals are:

$$\langle j_h | V_{ls}(r_i, r) | j_p \rangle = \int V_{ls}\, u_{j_h}(r_i)\, u_{j_p}(r_i)\, r_i^2\, dr_i \qquad \text{(II.49)}$$

where u_j is the radial part of the shell model bound state wave function, and j stands for the quantum numbers (N,l,j) where N is the principle quantum number, l the orbital angular momentum, and j the total angular momentum of the shell model orbital. We have used harmonic oscillator bound state wave functions, which seem to give an adequate representation of the shell-model states (Mc 69a) and have the advantage of being analytic.

The nucleus ^{120}Sn has been studied in the quasi-particle model by Yoshida (Yo 62). Since a quasi-particle is a mixture of a particle and a hole state, the expression for the matrix element M in this model is very similar to the preceding results for particle-hole excitations. In the notation of Yoshida:

$$M = \sum_{j_1 j_2} \hat{j}_1\, \hat{j}^{-1} \langle j_1 \| T_{lsj} \| j_2 \rangle \langle j_1 | V_{lsj} | j_2 \rangle \left[\psi^j_{j_1 j_2} U_{j_1} V_{j_2} + \phi^j_{j_1 j_2} V_{j_1} U_{j_2} \right] \qquad \text{(II.50)}$$

where expressions for the normalization coefficients $\psi^j_{j_1 j_2}$ and $\phi^j_{j_1 j_2}$ are given in Ref. (Yo 62) and U_j and V_j are the usual occupation parameters (Ba 63). A derivation of this result is given in Appendix C.

CHAPTER III

EXPERIMENTAL METHOD

III.A. Beam Line

III.A.1. Cyclotron and Beam Analysis System

All experimental data were taken using proton beams from the Michigan State University sector-focused cyclotron. The design and operating characteristics of this machine have been described in detail elsewhere (Bl 66). It is capable of producing high quality beams of several different projectiles over a wide energy range. For protons, this range extends from 20 to 50 MeV, although lower energy beams have been produced by accelerating molecular hydrogen (Pa 69).

A schematic diagram of the beam transport and energy analysis system appears in Figure III-1. The extracted proton beam was focused on the object slit S1 by a set of quadrupole doublets. Protons passing through this slit and the divergence limiting slit S2 are bent through 90° by the energy analyzing magnets M3 and M4, and then strike the image slit S3.

The properties of this beam transport system have

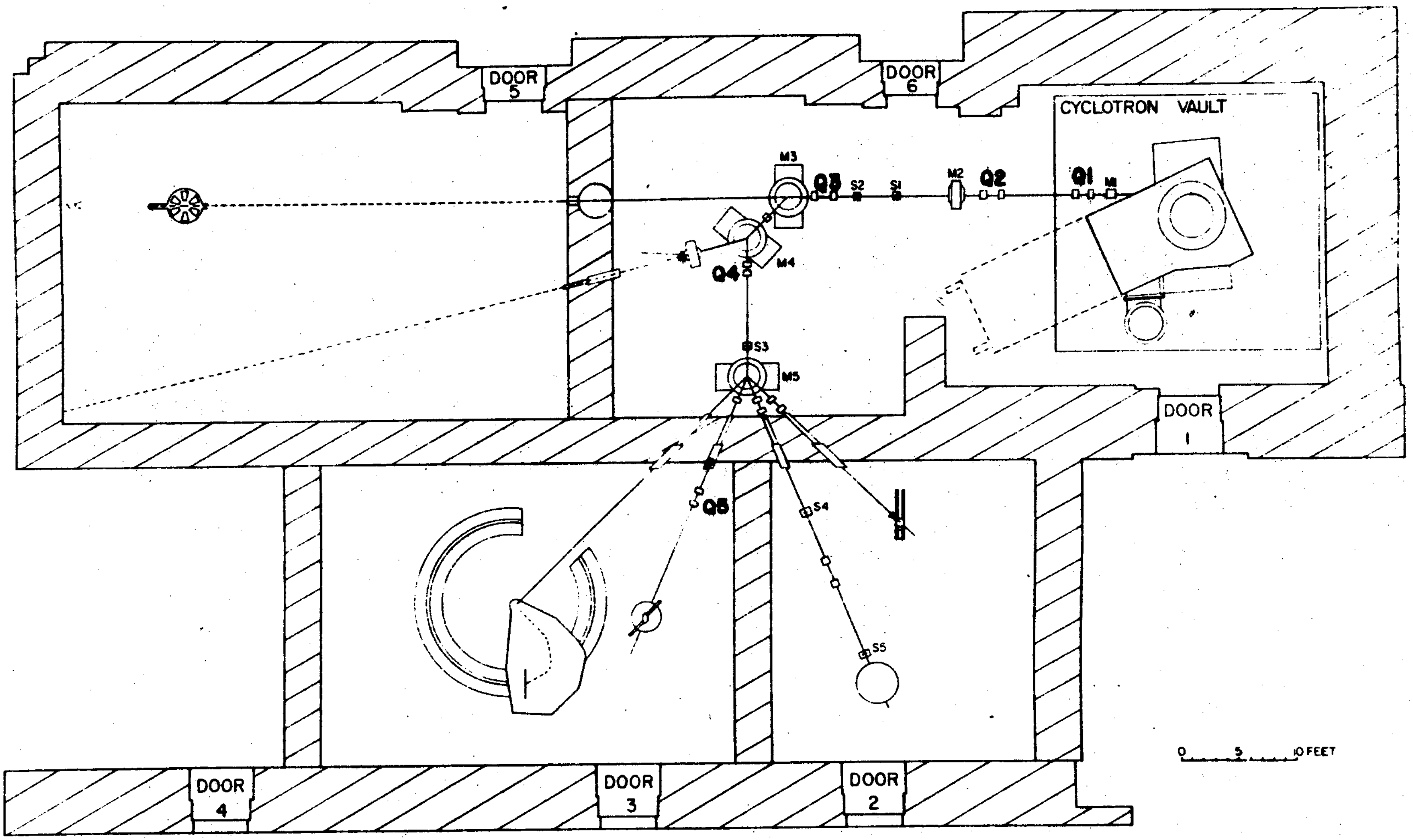

Figure III-1. Experimental area of the Michigan State University Cyclotron Laboratory.

been investigated previously. In particular, the energy resolution of the transmitted beam as a function of slit widths (Ma 67), and the energy of the analyzed beam as a function of magnet field strength (Sn 66) have been calculated. Typical slit openings used in this experiment were 0.25 cm for the object and image slits, and 0.30 cm for the divergence limiting slit. This corresponds to an energy resolution of 8 parts in 10^4 full width at half maximum (FWHM). The energy of the transmitted beam was calculated to within ±0.1 MeV from the measured field strengths.

III.A.2. Beam Alignment

The analyzed beam was deflected into the appropriate experimental area by magnet M5, and was focused on the target by the final quadrupole doublet Q5. No collimating slits were used near the target in order to keep background radiation in the experimental area to a minimum. Instead, the beam was positioned by observing a 0.125 mm thick piece of Pilot-B plastic scintillator* at the target position using a closed circuit television system.

In practice, the excitation of magnet M5 was set to the calculated value appropriate to the particle and energy required (Sn 66). Fine adjustments were then made to center the beam spot on fiducial marks inscribed in the plastic scintillator. In this way, the beam could be centered to within 1 mm. The scintillator was inserted into the beam

---

*Pilot Chemical, Watertown, Mass.

line several times during the course of a run to check against centering drifts, which did not occur. During the later runs with the tin target, the fields at magnets M3 - M5 were monitored with NMR fluxmeters.

Beam spots were typically rectangular, with a height of 2 mm and a width of 4 mm. Angular divergence was less than ±0.5°, as determined from the maximum possible beam diameter at the quadrupole doublet Q5.

III.A.3. Targets

The target used for the ^{12}C experiment was a 26.5 mg/cm^2 graphite foil*. Its uniformity was determined to be better than ±1% by monitoring elastic proton scattering from various areas of the sample. The tin target was a 9.9 mg/cm^2 foil rolled from 98.4% enriched ^{120}Sn obtained from the isotopes division of Oak Ridge National Laboratory.

The energy loss ΔE in the graphite target was 500 keV at 26 MeV, and 350 keV at 40 MeV. The corresponding value for the tin target was 100 keV at 30 MeV. The mean proton energy E_p was determined by subtracting $\Delta E/2$ from the energy determined by the beam transport system.

III.A.4. Target Chamber

The targets were mounted in a small Al chamber in which provisions were made to mount two targets. The angle

---

*Speer Carbon Co.,Inc., Carbon Products Div., St. Marys, Pa., Shield Grade 9326.

of the target frame relative to the beam line could be remotely adjusted and read out to within ±1°. Scattered protons passed through a 0.125 mm thick Mylar window in the side of the chamber. Energy-loss straggling in this window was approximately 180 keV. Because the states of interest are well separated ($>$ 1 MeV in the case of ^{120}Sn and $>$ 3 MeV in the case of ^{12}C), this broadening is quite acceptable, particularly since the use of a window leads to major design simplifications in the apparatus which positions the proton detector. For example, the arm on which this detector is mounted does not have to be inside a large vacuum chamber.

The counter arm could be remotely positioned to within ±0.1° over the angular range from 25° to 155°. The limits of this range are determined by the geometry of the target chamber and beam line, and by the size of the detector package. The center of rotation of this arm coincides with the center of the target frame to within 0.05 mm, and the maximum backlash in the positioning apparatus has been measured to be ±0.1° when the drive mechanism is properly adjusted.

III.A.5. Charge Integration

Protons passing through the target were collected in a 7.5 cm diameter by 1.5 m long Faraday cup located so that the beam stop was 2 m beyond the target position. This distance was chosen to enable the elimination of chance coincidences with background radiation coming from the

Faraday cup (see Sec. III.D.4). The length of the cup ensures that protons which suffer multiple collisions in the target will still be collected, and it also reduces the probability that electrons produced in the cup will leave it.

A study of the background radiation produced by various beam stop materials indicated that graphite was best suited for this purpose. The observed reduction in background (about a factor of 2.5 compared to Al, for 30-MeV protons) overweighed considerations of the additional radiation hazard posed by the production of relatively long-lived (~20 min.) activity in the beam stop. However, Al was used for the beam stop in the ^{12}C runs to avoid possible confusion of 4.44 MeV gamma rays from the target and the beam stop.

The beam current and integrated charge were measured using an Elcor Model A310B current integrator. The accuracy of this instrument has been measured to be within ±1% (Ko 67).

III.B. Detectors

III.B.1. Gamma-ray Detector Assembly

The gamma-ray detector used throughout this experiment was a 5 cm diameter by 7.5 cm long NaI (Tl) scintillator mounted on a RCA 8575 photomultiplier*. The energy resolution of this detector has been measured to be 7.6% for the 662 keV gamma line from ^{137}Cs.

---

*Obtained from the Harshaw Chemical Co.; Cleveland, Ohio.

The proper distribution of bias voltage to the dynodes of the photomultiplier was maintained by an ORTEC 265 phototube base. A schematic diagram for this unit appears in Figure III-2. One important feature of the design is the fact that the anode is operated at ground potential. This means that the fast output can be direct-coupled and therefore that the rise time of this signal is not limited by the time constant of a coupling capacitor. A minor disadvantage of this arrangement is that the photocathode is operated at a high negative potential with respect to ground so that the outer glass envelope of the phototube must be well insulated.

A major problem associated with the photomultipliers used in this experiment was the gain shifts observed at high count rates. The additional current drawn through the voltage divider string during a pulse causes an increase in the dynode potentials with respect to the photocathode, resulting in a net increase in the effective gain of the system. Since the current amplification of photomultiplier tubes is proportional to a very high power of the interdynode potential (Ch 61), this effect can place rather severe limits on the allowable variations in count rate. The problem can be eliminated for short term fluctuations, such as those due to the pulsed nature of the cyclotron beam, simply by connecting rather large capacitors across the latter stages of the tube to serve as 'charge reservoirs'. This method is effective in eliminating fluctuations with time constants of several milliseconds. It becomes quite

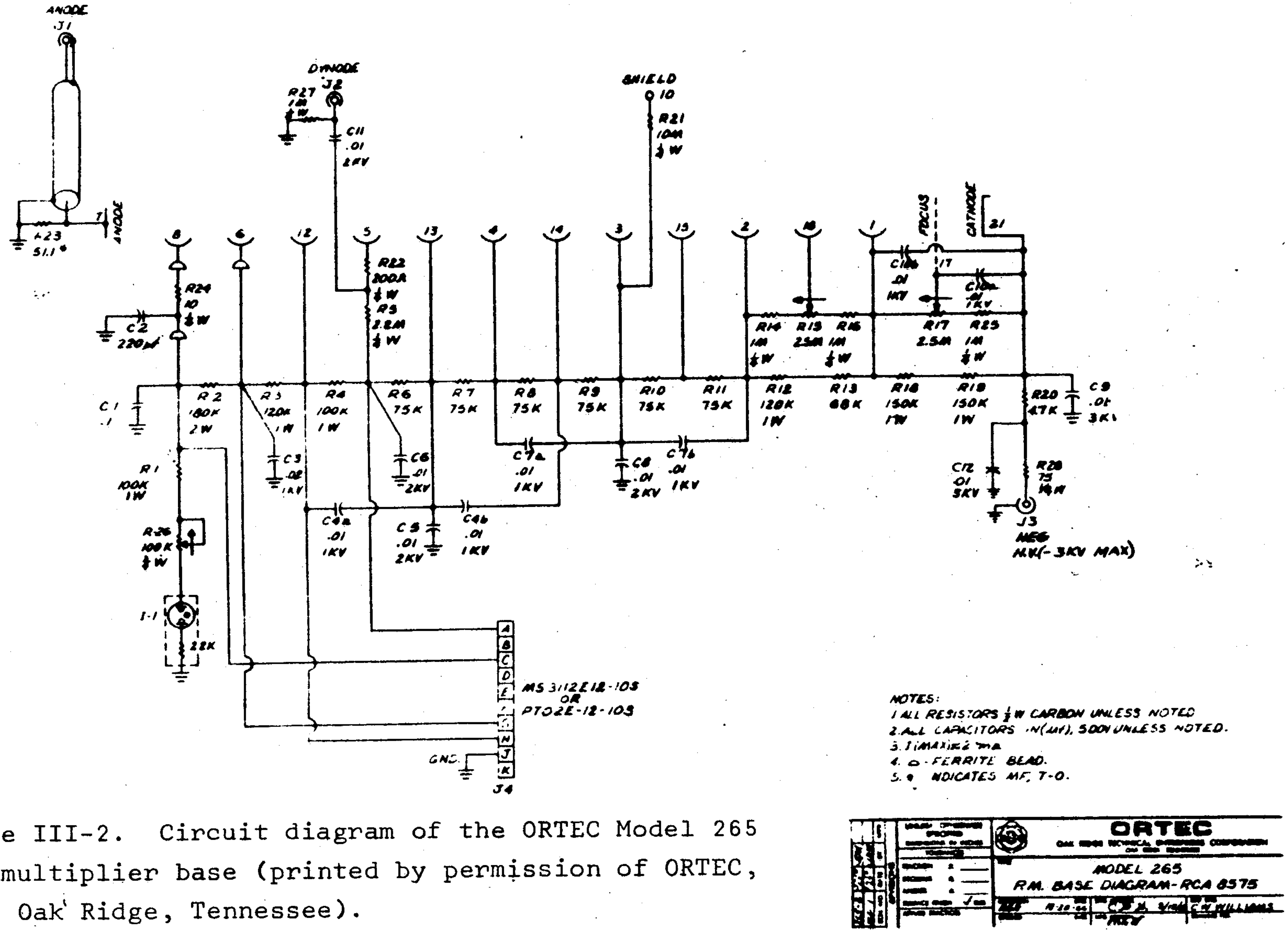

Figure III-2. Circuit diagram of the ORTEC Model 265 photomultiplier base (printed by permission of ORTEC, Inc.; Oak Ridge, Tennessee).

impractical, however, if variations in average beam intensity can occur over a time interval of minutes, as was often true in this experiment. We have substantially reduced the observed gain shifts in the latter case by employing zener diode voltage stabilization on the last four dynodes (Figure III-3). The increased stability comes at the expense of flexibility in the selection of photomultiplier gain, since the stabilizer must be designed for a particular dynode voltage distribution. The operating voltage for the gamma detector was -2400V.

The gamma-ray detector was contained in a 130 kg. cylindrical Pb shield supported below the target chamber. This shield was quite effective in reducing the count rate in the detector due to general room background. The entire assembly was centered on the normal to the scattering plane to within 4 mm and the distance from the beam line to the center of the detector was variable between 12.5 and 45 cm. Scattered protons were kept out of the gamma-ray detector by the 1.27 cm thick Al floor of the target chamber.

III.B.2. Proton Detector for the ^{12}C Experiment

The proton detector for the ^{12}C experiment was a 3.8 cm diameter by 1.9 cm thick NaI (Tl) scintillator mounted on an RCA 8575 photomultiplier tube. This unit was packaged at the cyclotron laboratory. A diagram of the completed assembly appears in Figure III-4. Because of the hygroscopic properties of NaI, the packaging was carried

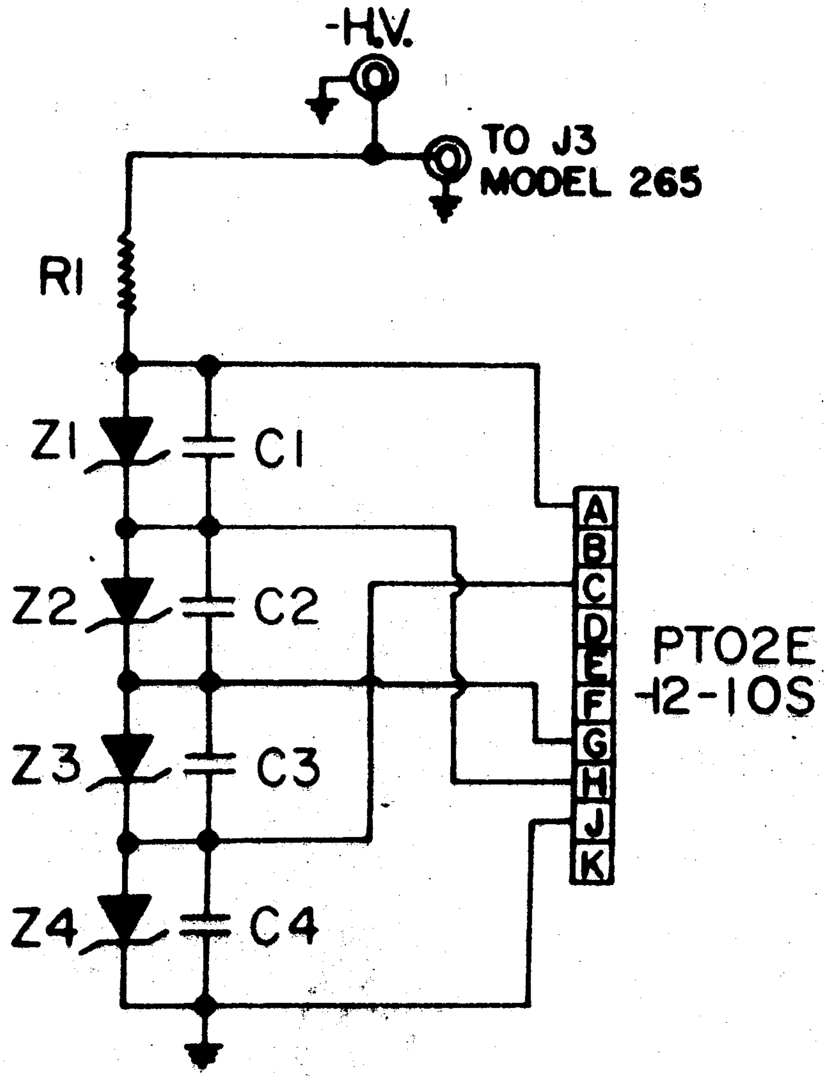

VOLTAGE STABILIZER

H.V.	1800V.	2400V.
RI	1.625Meg,2W	2.18Meg,2W
ZI	IN965+IN985	IN976+IN985
Z2	IN975+IN985	IN984+IN985
Z3	IN970+IN991	IN984+IN991
Z4	IN986+IN991	IN992+IN991

CI-C4 0.5μf., 600V.

Figure III-3. Diagram of a zener-diode voltage regulator for the last four dynodes of the photomultiplier.

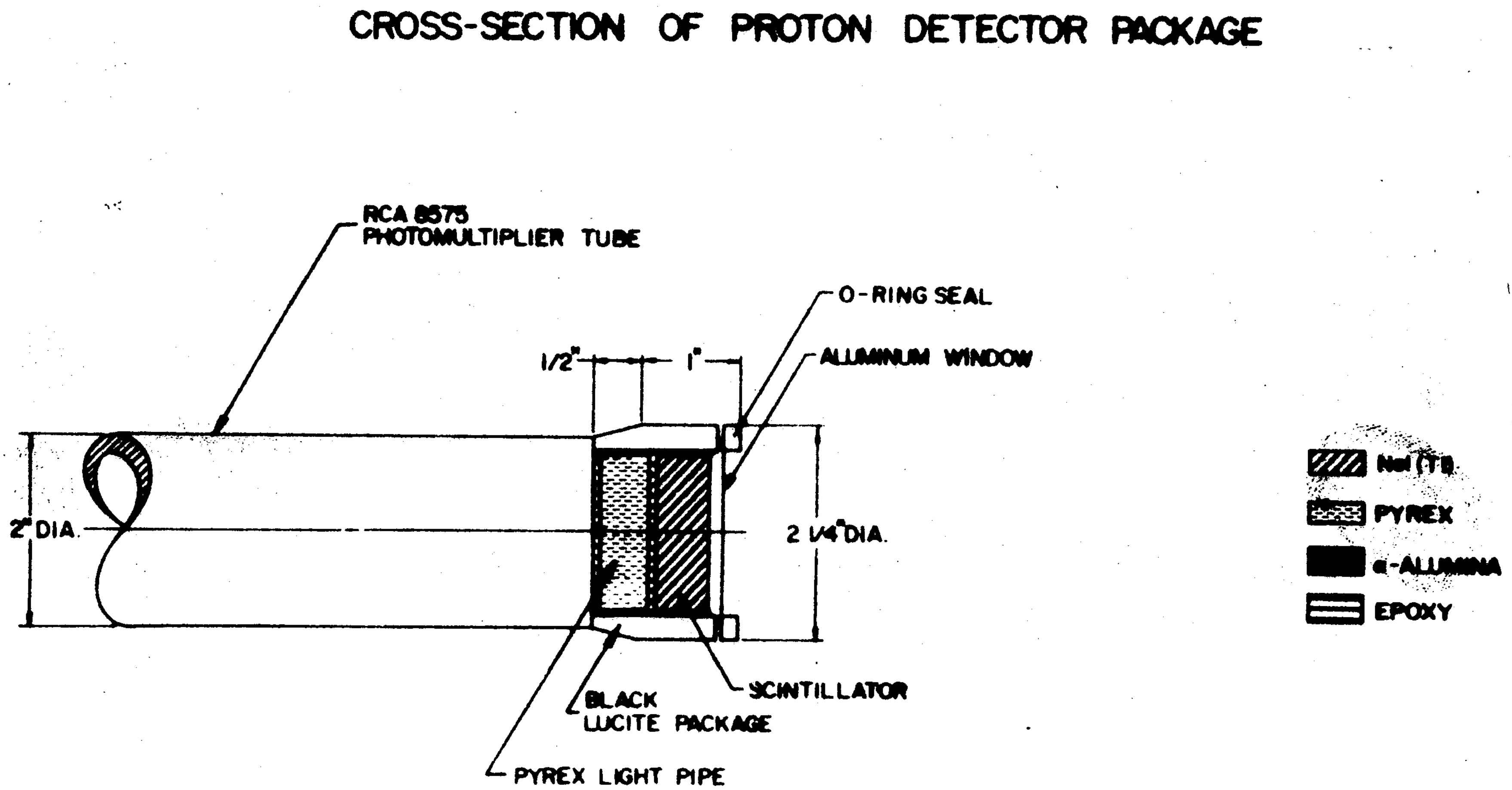

Figure III-4. Cross section of proton detector package.

out in a low humidity atmosphere, and careful attention was paid to the problem of eliminating moisture leakage into the container.

It was previously mentioned in connection with the gamma-ray detector that the cathode of the photomultiplier tube is operated at a high negative potential with respect to local ground. Care must be taken to insure that this high voltage is not dropped across the glass envelope of the tube. For this reason, the detector package was machined from black Lucite plastic. The interior surface of this container was covered with a reflecting coating of #1000 α-alumina (Al_2O_3) using the following technique: a thin layer of clear acrylic lacquer was sprayed onto the surface to be coated, and the alumina powder was immediately dusted on. Several repetitions of the process were necessary to build up a uniform reflecting layer.

The NaI (Tl) scintillator was carefully polished, and then bonded to a 3.8 cm diameter by 1.27 cm thick Pyrex light pipe using R-313 epoxy*. This subassembly was tightly clamped together until the epoxy set to prevent the formation of bubbles which would spoil the optical contact and therefore the energy resolution. The advantage of using epoxy, of course, is the simplification introduced by not having to use clamps to maintain optical contact once the bond is set. An experiment was performed in an attempt to determine whether a scintillator mounted in this way would show any

---

*C.H. Biggs Co.; Santa Monica, California degradation in performance as compared to one mounted in the more conventional way using DC-200 silicone grease[*], with spring clamps to maintain optical contact. No significant difference was observed.

The scintillator-light pipe subassembly was bonded to the face of the phototube, again maintaining pressure until the bond had set. Extra epoxy which was squeezed out from under the light pipe was carefully trimmed away to prevent light leakage, and then the detector package was epoxyed to the phototube around the scintillator. A 0.0025 cm Al entrance window was placed over the detector and sealed in place using an o-ring. The packaging was completed by wrapping the phototube with several layers of black electrical tape (10 kV per layer), which served both as a light shield and as electrical insulation for the phototube envelope.

The RCA 8575 photomultiplier tube has the unfortunate characteristic of a clear glass base. The following technique was used to eliminate troublesome light leaks: the base was covered with a coating of G.C. 47-2 black corona dope[**], which was thinned to a watery consistency using G.C. 28 solvent[**] and then applied in successive layers until no light could be seen through the base. This treatment was used successfully for both the proton and

---

[*] Dow Corning Co.; Midland, Michigan

[**] G.C. Electronics Co.; Rockford, Illinois

gamma-ray detectors; no evidence of current leakage between connector pins has been observed over the course of one year.

The completed proton detector had a measured energy resolution of 600 keV (FWHM) for 30-MeV protons when a 1.9 cm diameter circular collimator was used (Figure III-5). The resolution improved to 400 keV when a 0.63 cm diameter collimator was used. It is assumed that the latter effect is due to inhomogeneities in the NaI (Tl) scintillator since the observed output pulse height for a given proton energy depends to some extent on the location of the small collimator relative to the crystal face.

Since the proton detector also suffered from pulse height shifts with fluctuating count rate, a zener diode stabilizer was constructed for it. The circuit appears in Figure III-3. Note that the component values differ somewhat for the proton and gamma-ray detectors since the former was operated at a lower bias voltage (-1800V).

III.B.3. Proton Detectors for the ^{120}Sn Experiment

The average separation between the three lowest lying levels of ^{12}C is about 3 MeV, while for ^{120}Sn it is on the order of 1 MeV. In order to cleanly separate the states in ^{120}Sn, it was necessary to use a solid state detector. We used a 5 mm thick lithium-drifted silicon detector* which

---

*Obtained from the Kevex Co.; Burlingame, California

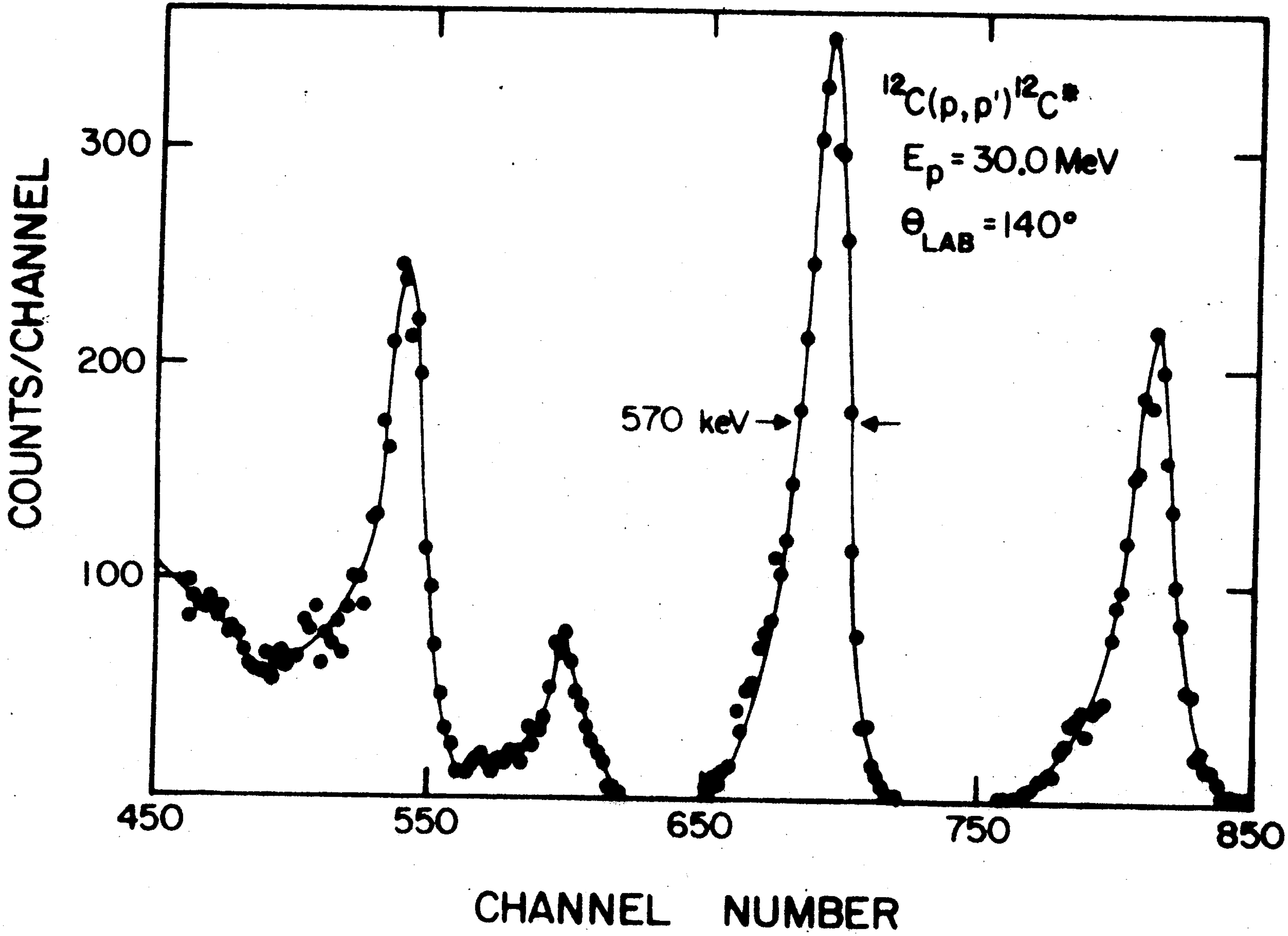

Figure III-5. Typical proton spectrum for ^{12}C experiment.

had an active area of 80 mm^2. To eliminate multiple scattering of protons out of the sensitive volume, a 0.63 cm diameter collimator was used. The detector was operated in vacuum at 1500 V bias, and arrangements were made to cool it to -70 °C with dry ice and methyl alcohol. Under these conditions, a typical value for the measured energy resolution was 170 keV (Figure III-6) which was quite adequate to separate the states of interest.

During the course of the experiment, it was found that the cross-section to the first excited state of ^{120}Sn in the angular region from 100° to 155° was too small to enable the collection of an adequate number of coincidence events in a reasonable time. Physical limitations imposed by the construction of the target chamber and the detector package restricted the minimum target-to-detector distance to 10 cm, and the beam current was limited by pileup losses in the gamma detector (see Sec. III.D.5). Therefore, the NaI detector was used in this angular range, with a 1.26 cm diameter collimator.

III.C. Electronics

A block diagram of the electronics for this experiment appears in Figure III-7. Essentially, it consists of a fast-slow coincidence circuit in which the fast unit is a time-to-amplitude converter (TAC).

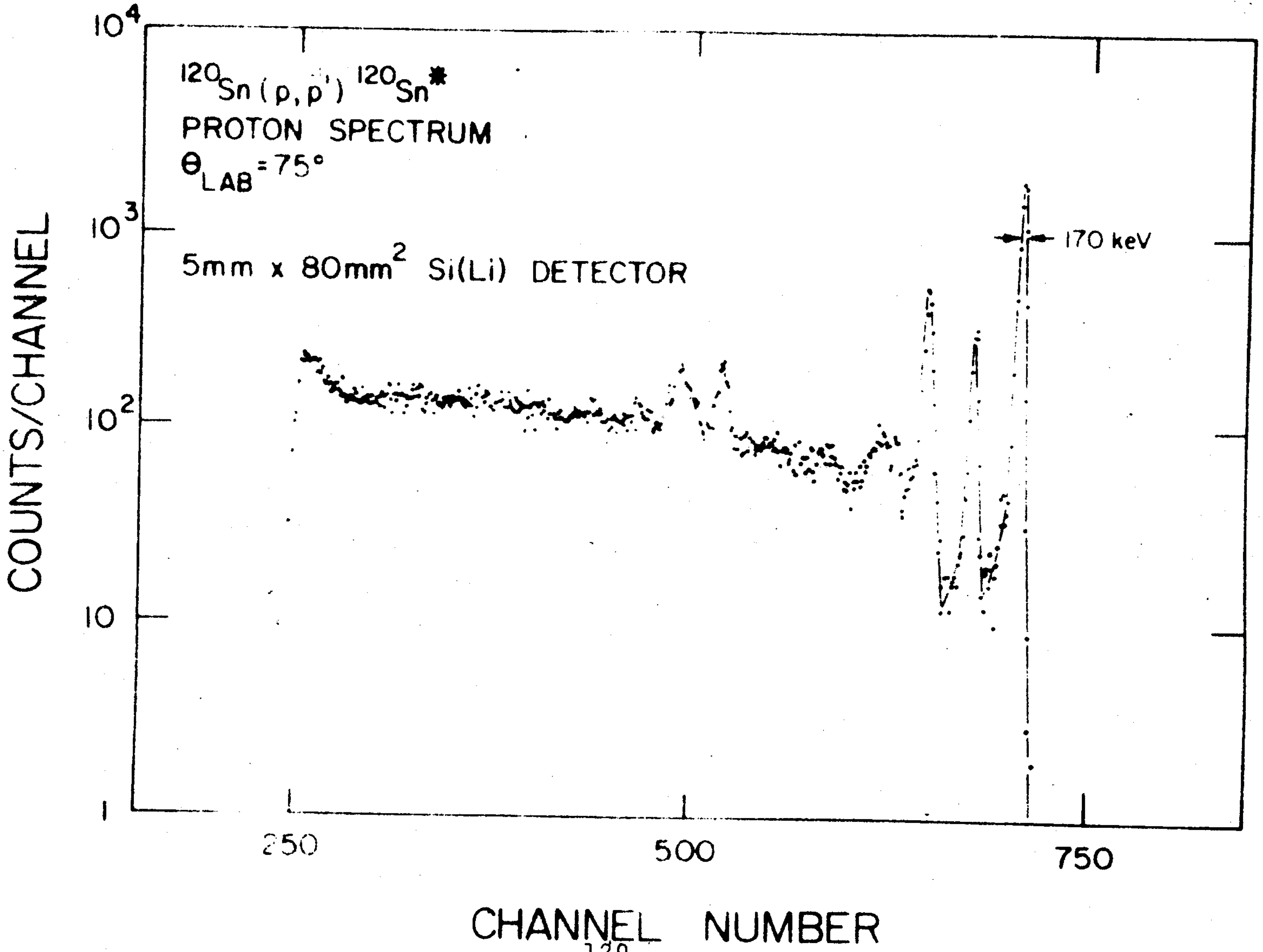

Figure III-6. Typical proton spectrum for ^{120}Sn experiment.

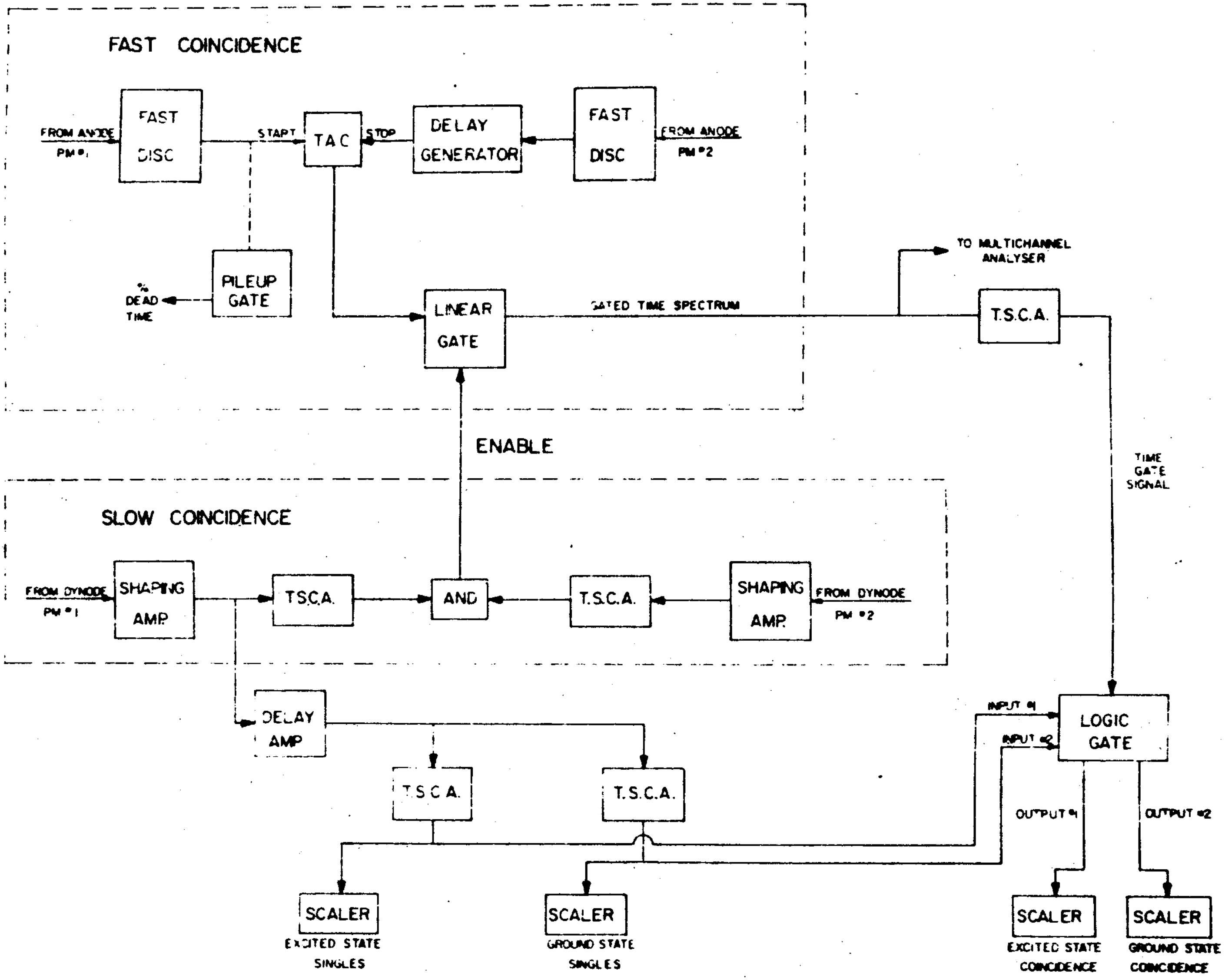

Figure III-7. Block diagram of the coincidence circuit.

III.C.1. Fast Timing Circuitry

Presently, there are three methods of deriving time information from a detector pulse. These are: 1) leading edge trigger, 2) conventional crossover timing, and 3) 'fast' crossover timing. The last method is applicable only to scintillators having a decay time-constant $\tau_d \leq 10$ns, such as Pilot-B plastic scintillator. For this reason, it was not considered for this experiment (τ_d for NaI = 250ns) and it will not be discussed here. Of the remaining methods, which are illustrated in Figure III-8, leading edge trigger is by far the better choice for fast timing since it results in less 'jitter', i.e., time dispersion due to electronic noise and statistical fluctuations in the detector pulses. Recent theoretical studies (Be 66) have shown that leading edge timing is better than the conventional crossover method by about a factor of 14.

A major problem in the use of leading edge timing is the need to restrict the dynamic range of pulse amplitudes accepted to avoid the time resolution problems associated with 'walk' in the low-level discriminator. 'Walk' is defined by the time shift due to a fixed low-level threshold and variable energy pulses (see Figure III-8). For a pulse rise time of 10 nsec., and a ratio $E_{thresh.}/E_0 = 0.2$, which represent typical values for this experiment, the dynamic range must be limited to $D \leq 2$ to obtain the required 1 nsec. resolution (neglecting jitter). This is not a particularly restrictive requirement, but it does mean that

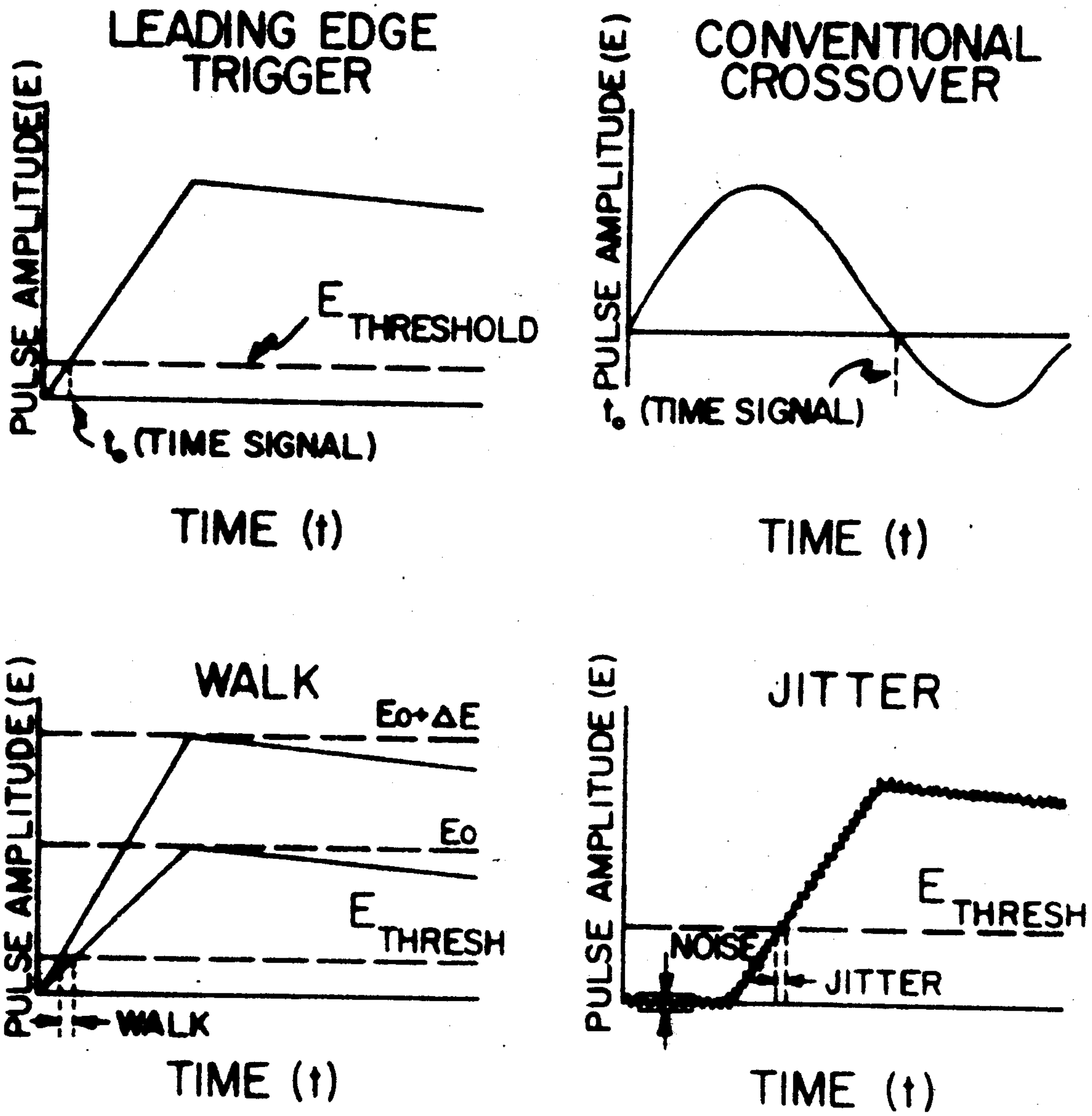

$$\text{DYNAMIC RANGE (D)} = \frac{E_0 + \Delta E}{E_0}$$

$$E(t) = E_{MAX}\ t/\tau \quad (\tau = \text{PULSE RISE TIME})$$

$$\text{WALK} = t_{THRESH}(E_0) - t_{THRESH}(E_0 + \Delta E)$$

$$= \tau\,\frac{E_{THRESH}}{E_0}\left[1 - \frac{1}{D}\right]$$

Figure III-8. Schematic representation of leading-edge and conventional crossover timing, and the definition of 'walk' and 'jitter'.

the fast coincidence measurement must be supplemented by side-channel amplitude analysis. The crossover technique does not suffer from this problem since the crossover time of a double-delay-line clipped pulse is independent of the pulse amplitude, to a very good approximation. Therefore, it is particularly valuable for those applications in which a very large dynamic range is required.

In this experiment, timing information in the fast coincidence channel was obtained by leading-edge timing with suitable low-level discriminators viewing the fast signals from the detectors. The logic signals from these discriminators were used to start and stop the TAC. A variable delay was introduced into the stop side to shift the 'true + chance' peak in the time spectrum to a convenient pulse height. The time spectrum was gated by a logic signal from the slow coincidence unit, thereby restricting the effective dynamic range as discussed below. The gated time spectrum was analyzed using a 1024 channel pulse height analyzer. Typical time spectra are shown in Figures III-9 to III-12.

III.C.2. Side-Channel Amplitude Analysis

The slow coincidence unit, which provided pulse-height information, was a conventional zero-crossover coincidence circuit. The linear signals from the two detectors were converted to bipolar pulses and analyzed for both pulse height and time information using timing single channel

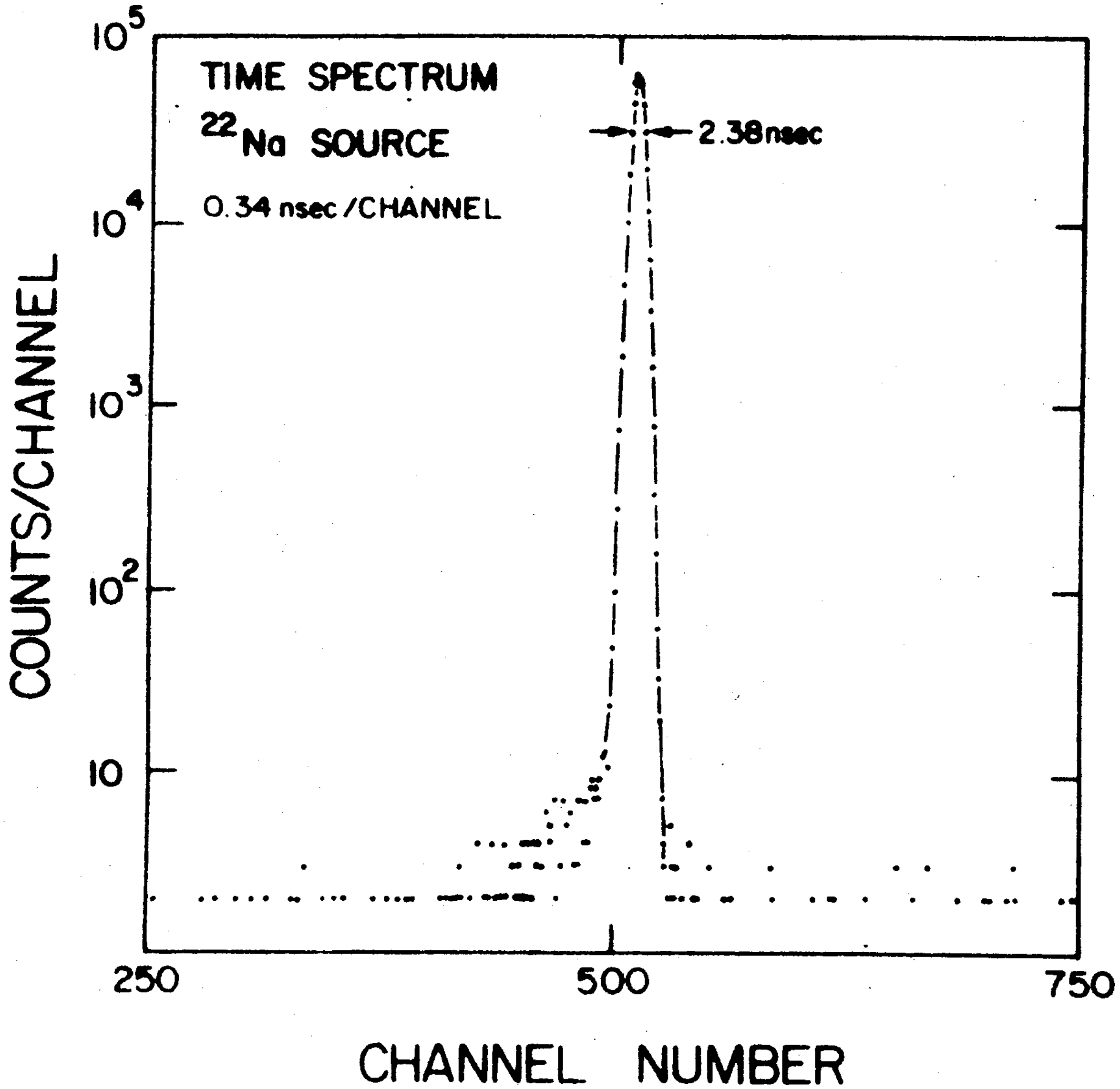

Figure III-9. Typical time spectrum obtained with the circuit of Figure III-7 for the 511 keV gamma-rays from ^{22}Na.

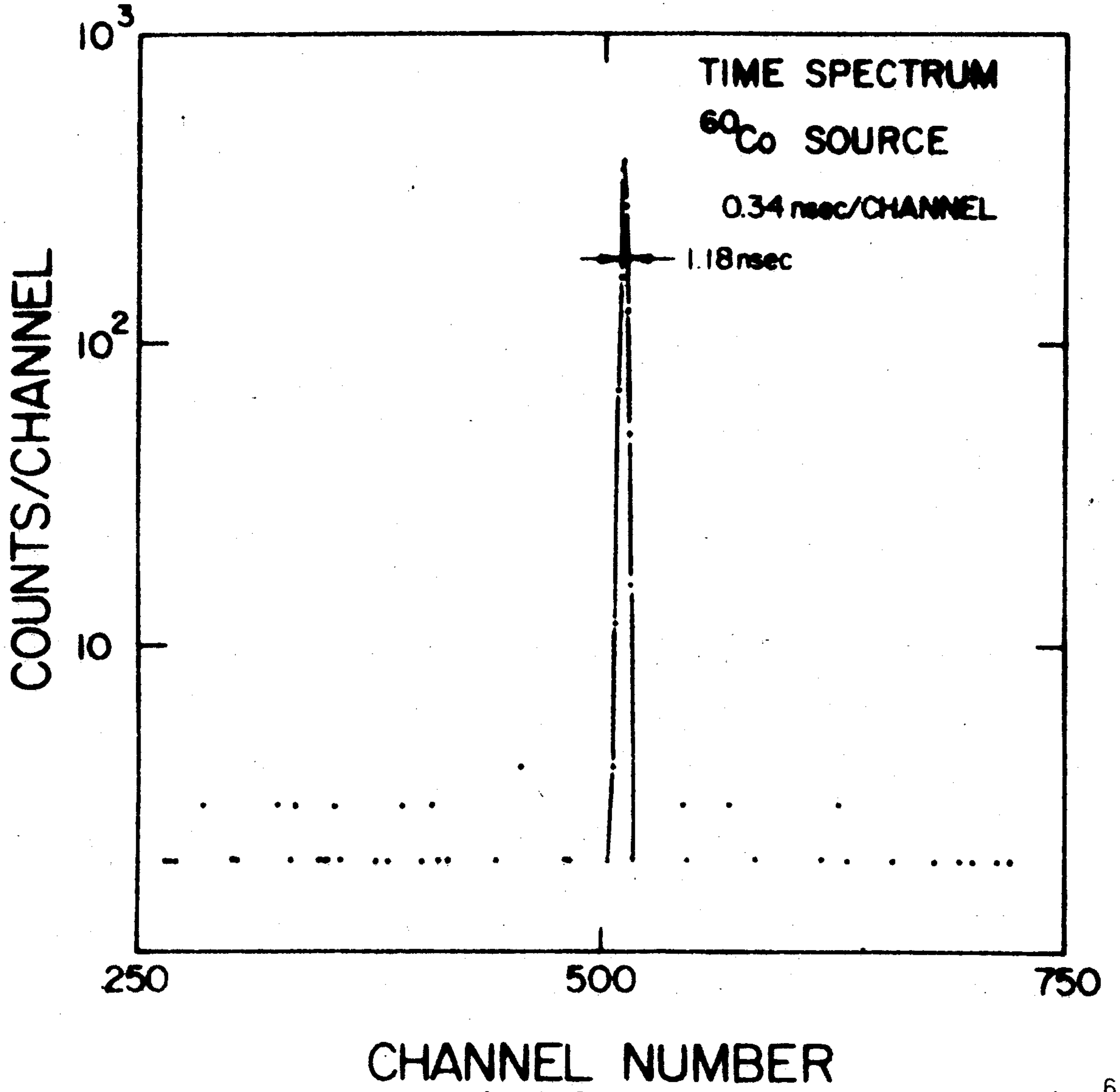

Figure III-10. Typical time spectrum obtained for the gamma-ray cascade in ^{60}Co (E_γ = 1.17 and 1.33 MeV).

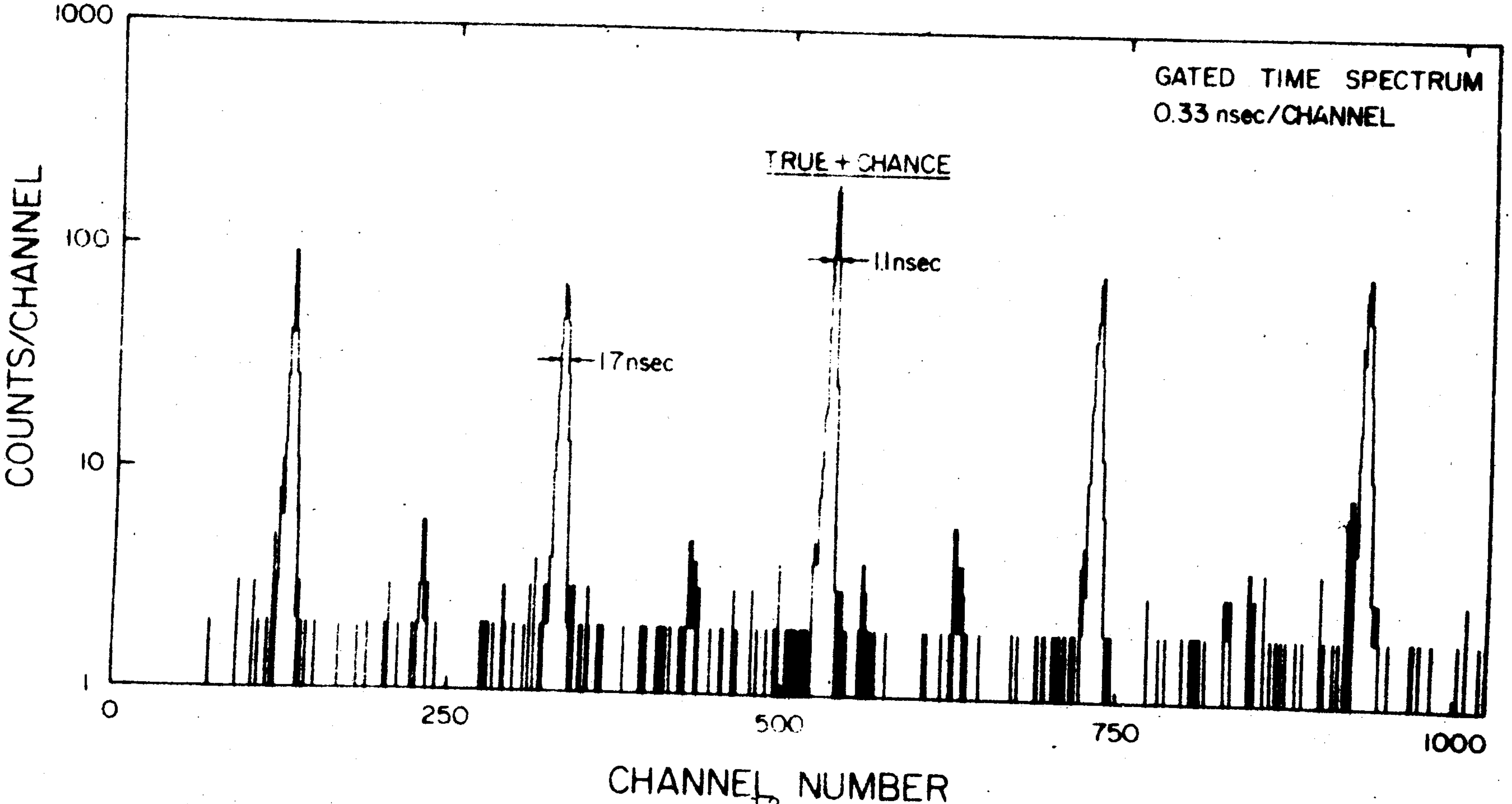

Figure III-11. Typical time spectrum for the ^{12}C experiment. The width of the central ('TRUE+CHANCE') peak is 1.1 nsec (FWHM). The remaining ('CHANCE') peaks are broader due to a contribution from the beam pulse width. Resolving time after subtraction of chance events is 0.9 nsec (FWHM).

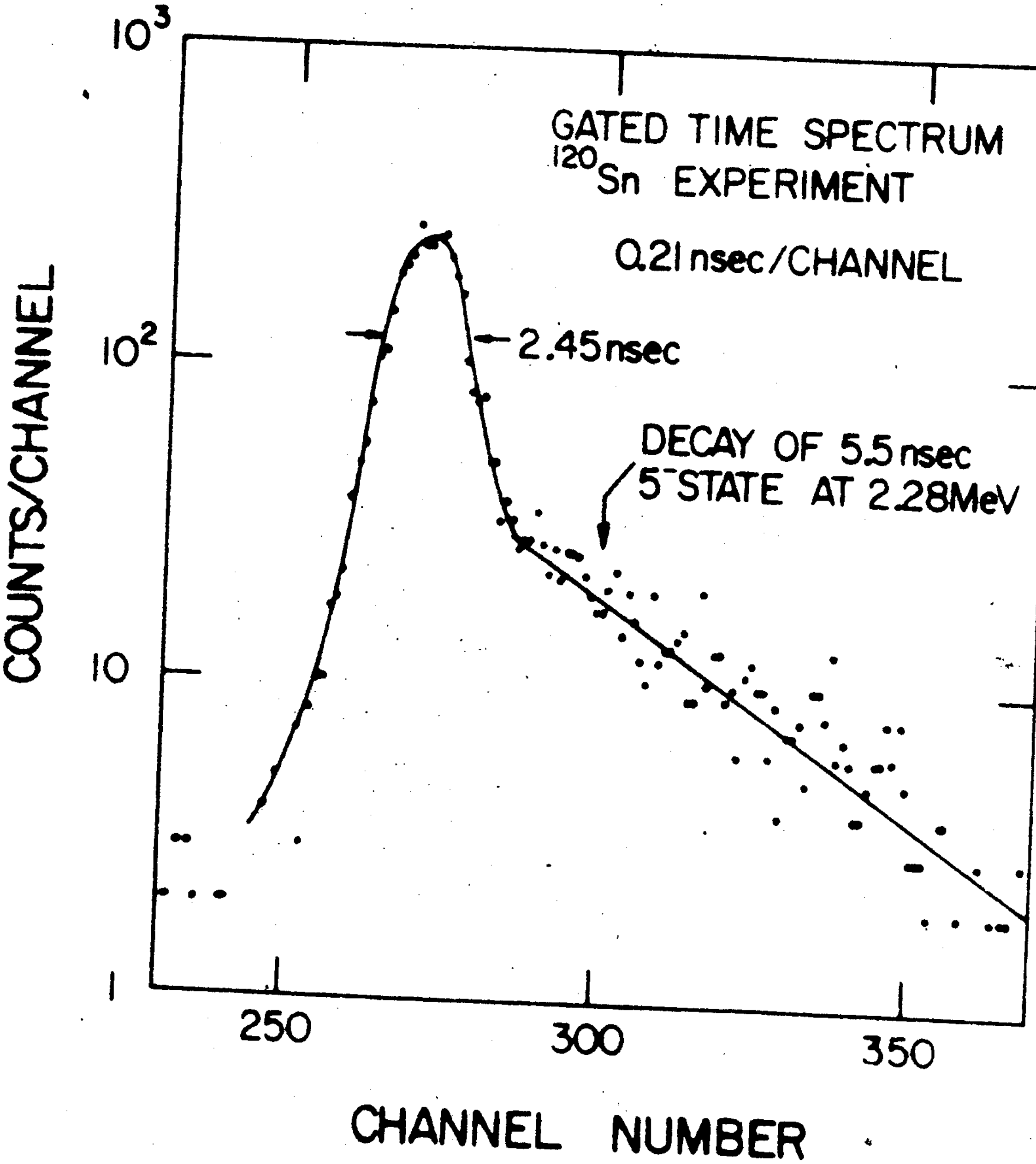

Figure III-12. Typical time spectrum for the ^{120}Sn experiment. The exponentially decaying 'tail' is due to the decay of the 5.5 nsec state at 2.28 MeV (see Figure III-13), which cascades through the 1.17 MeV state.

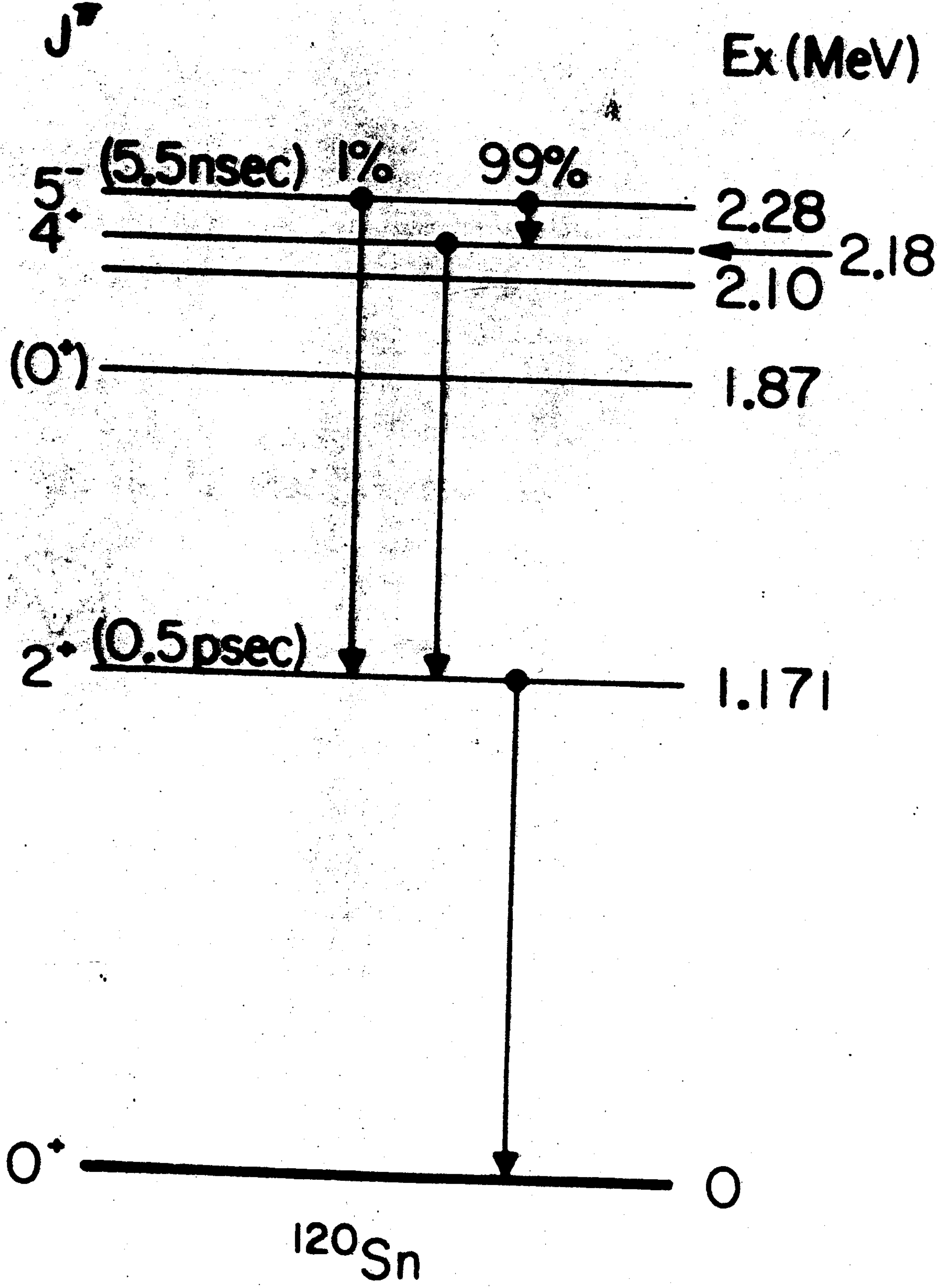

Figure III-13. Energy level diagram for the low-lying excited states of ^{120}Sn.

analyzers (TSCA). These units are designed so that their output occurs at the zero-crossing time of the input signal.

A pulse-height window was set over elastic and first excited state events in the proton channel, and over the relevant portion of the gamma-ray events in the gamma channel. Of course, the efficiency of gamma-ray detection depends on the width of this pulse height window because of the continuous Compton spectrum below the photopeak. The methods used to account for this effect are described in Sec. III.D.2.

Time coincidence between logic pulses from the timing single channel analyzers was determined by a conventional overlap coincidence (logical AND) circuit, which produces an output if the signals at the two inputs overlap in time. Since these signals were each 500 nsec. wide, the effective slow coincidence resolving time (2τ) for this experiment was 1 μsec. The output of this circuit enabled the linear gate in the fast coincidence unit, as previously described. The effect of the slow coincidence requirement on the time resolution is illustrated in Figure III-14.

An alternate arrangement is possible, in which the slow logic signal is used to open a gate on the 'start' side of the TAC, thus enabling time conversion to begin. This method has the possible advantage of reducing the dead time of the TAC, which is only required to convert the relatively few pulses satisfying slow coincidence requirements. However, it is then necessary to delay the fast time signals to the TAC by a rather large amount (of the order of 1 μsec)

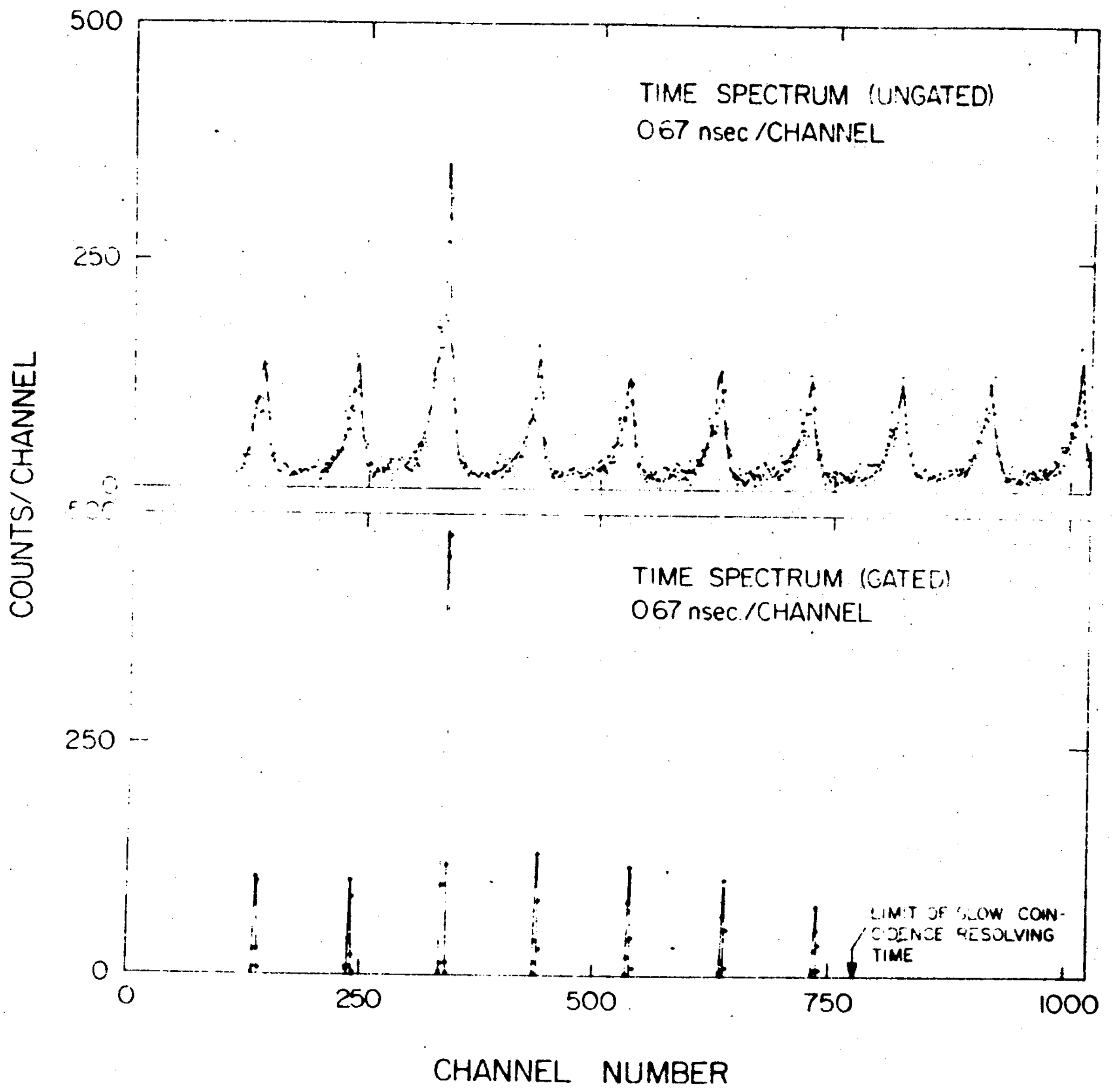

Figure III-14. Effect of the slow-coincidence requirement on the time spectrum for the ^{12}C experiment.

until the slow logic has had time to reach a decision. Cable delays of this length are impractical because of their large attenuation factor, and electronic delays introduce too much jitter into the fast coincidence circuit and are beset by dead time problems of their own. Therefore, this method was not used for the present experiment.

III.C.3. Data Collection Circuitry

The 'true + chance' peak in the gated time spectrum was selected by yet another timing single channel analyzer, as indicated in Figure III-7. The resulting time gate signal opened a logic gate, enabling signals from two more single channel analyzers to be scaled. One of these analyzers was set over the elastic events, and the other analyzed only events corresponding to the excitation of the state being investigated. In addition, the singles events in these two analyzers were simultaneously scaled. The resulting four numbers for each angle enabled us to calculate the spin flip probability, as discussed in Sec. III.D. below.

The ^{120}Sn data was collected in a somewhat different manner, due to the smaller separation between the states. In this case, separate singles and coincidence spectra were taken at each angle with a multichannel analyzer. These spectra were later integrated to determine the number of singles and coincidence events in the elastic peak, and in the peak corresponding to the excitation of the 1.17 MeV first excited state.

III.D. Data Reduction

III.D.1. Angular Correlation Function and Spin-Flip Probability

The connection between the gamma-perpendicular correlation and proton spin-flip probability was first demonstrated by Schmidt, et.al. (Sc 64). They based their result on a theorem due to A. Bohr (Bo 59), which states that for any two-body scattering system which conserves parity and total angular momentum the eigenvalue of the operator:

$$R' = P_n e^{i\pi S_z} \tag{III.1}$$

is a constant of the motion. Here, P_n is the total intrinsic parity of the two-body scattering system and S_z is the projection of the total spin angular momentum onto the normal to the scattering plane. A short proof of the theorem is given in Appendix A.

We now consider the application of the theorem to proton scattering from an even-even nucleus, which has a ground state spin (parity) of 0 (+). Since the intrinsic parity of the proton is positive, the eigenvalue of R' in the initial state is:

$$\text{eigenvalue}\,(R') = e^{i\pi m_p^i} = (-)^{m_p^i} \tag{III.2}$$

where the notation has been simplified by letting m_p^i represent the projection of the proton spin onto the normal to the scattering plane. If the nucleus is excited to a positive parity level, the eigenvalue of R' in the final state is:

$$\text{eigenvalue}\,(R') = e^{i\pi(m_p^f + m_n^f)} = (-)^{m_p^f + m_n^f} \qquad \text{(III.3)}$$

where m_n^f is the projection of the nuclear spin onto the normal to the scattering plane. The Bohr theorem states that this eigenvalue is a constant of the motion, so that:

$$(-)^{m_p^i} = (-)^{m_p^f + m_n^f} \qquad \text{(III.4)}$$

Letting $m_p^i - m_p^f = \Delta m_p$, this becomes:

$$(-)^{m_n^f} = (-)^{\Delta m_p} \qquad \text{(III.5)}$$

The quantity $|\Delta m_p|$ is unity if the proton undergoes spin flip and zero otherwise. If the final state nuclear spin is $J_f = 2$, m_n^f can only take on the values $(\pm 2, \pm 1, 0)$. Of these, only the states $m_n^f = \pm 1$ satisfy the requirements of the Bohr theorem (III.5) if spin flip has occurred. We conclude that spin-flip scattering selectively populates the $m = \pm 1$ magnetic substates of the 2^+ level.

The connection with the gamma-perpendicular correlation comes about because the de-excitation gamma radiation from a nucleus which has been excited to the $m = \pm 1$ magnetic substates has a very distinctive characteristic. The radiation pattern has a maximum along the quantization axis (normal to the scattering plane), where the patterns from the other substates have nodes (see Figure III-15). Therefore, the flux of gamma radiation along the normal to the scattering plane is directly proportional to the spin-flip probability in the interaction. The proportionality constant is derived in Appendix B.

These arguments can be extended with very minor modifications to the case of the excitation of quadrupole states of the opposite parity ($J^{\pi} = 2^-$), or of dipole states ($J^{\pi} = 1^{\pm}$), from a 0^+ ground state. Unfortunately, they cannot be extended to states of higher angular momentum (such as the strong 3^- states observed in ^{16}O and ^{40}Ca) because the higher odd-m substates, which can also be populated by spin-flip reactions, do not have the distinctive signature of the $m = \pm 1$ sublevel (Bl 52). It is also possible to perform the experiment with other spin-1/2 particles. This has already been done for the scattering of ^3He from ^{12}C (Pa 68).

The Bohr theorem itself may be generalized to the case of several particles in the final state, if all the reaction products are confined to a single plane. Possible applications of this extended theorem are given by Bohr (Bo 59), but will not be discussed here.

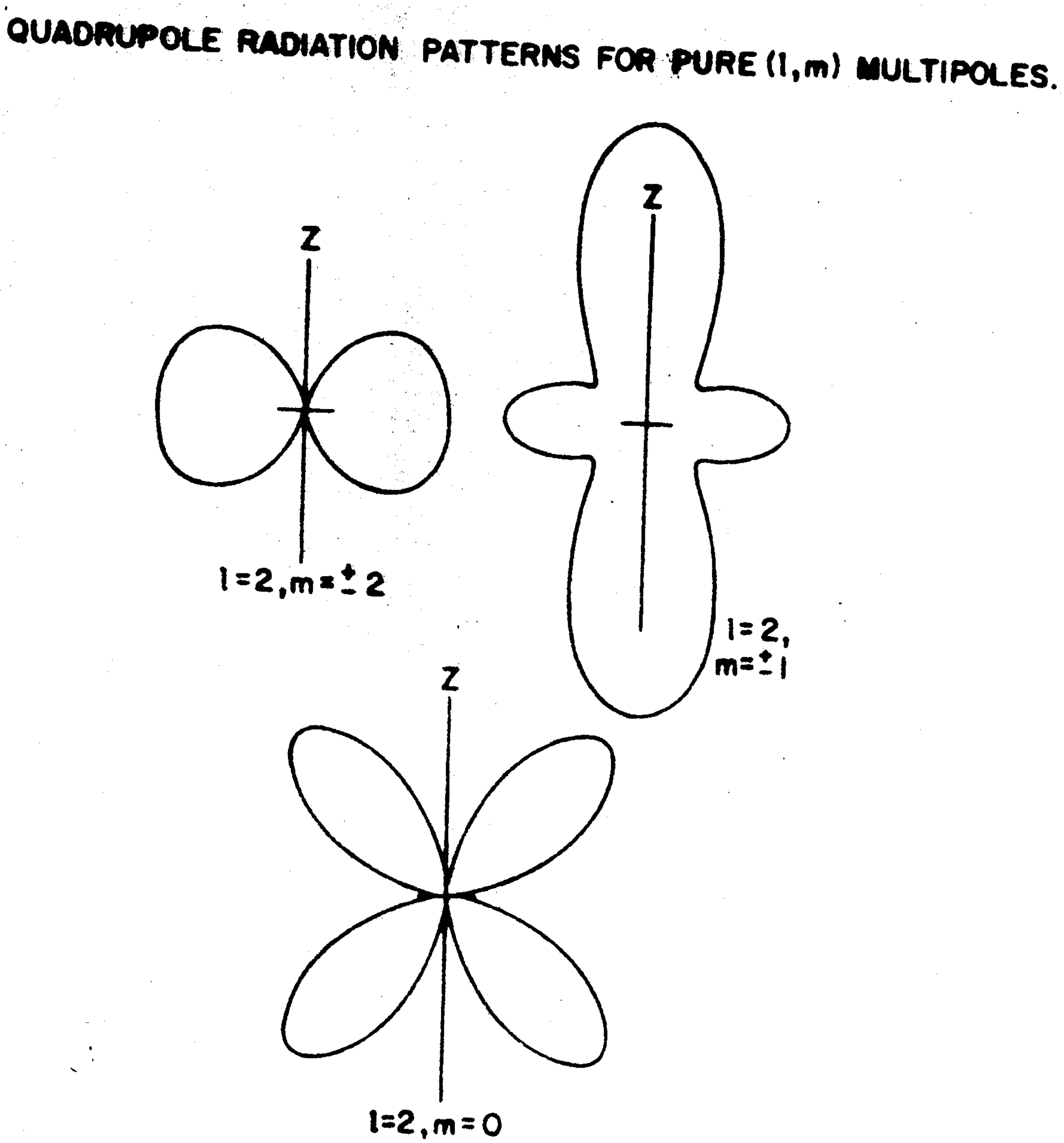

Figure III-15. Quadrupole radiation patterns for pure (l,m) multipoles. These are polar plots of intensity vs. angle relative to the axis of quantization (z-axis).

III.D.2. Gamma Detector Efficiency Measurements

In order to determine the absolute spin-flip probability, it is necessary to know the efficiency for detection of gamma radiation. For a given NaI crystal, this quantity is a function of the energy of the gamma ray, the distance from the source to the detector, and the width of the window set on the gamma-ray pulse height spectrum (see Figure III-16). In addition, it may also depend on the immediate environment of the detector. For example, it is possible that Compton scattering from the Pb shield surrounding the detector could significantly alter the observed pulse-height spectrum.

Several auxiliary experiments were performed in order to determine the efficiency of the gamma detector in the particular geometry used. For the ^{12}C experiment, the total (p,p') cross section to the first excited state was measured for $E_p = 26.2$ and 40.0 MeV. In addition, the gamma-ray angular distributions from the same state at both energies were determined. The integrated gamma-ray distributions were normalized to the total cross sections to obtain absolute gamma-ray differential cross sections. These were subsequently used to determine the efficiency of the NaI detector in the experimental geometry by simply counting the number of 4.44 MeV gamma rays in the pulse-height window, and comparing to the number obtained from the absolute cross sections. The measured efficiencies appear in Table III-1.

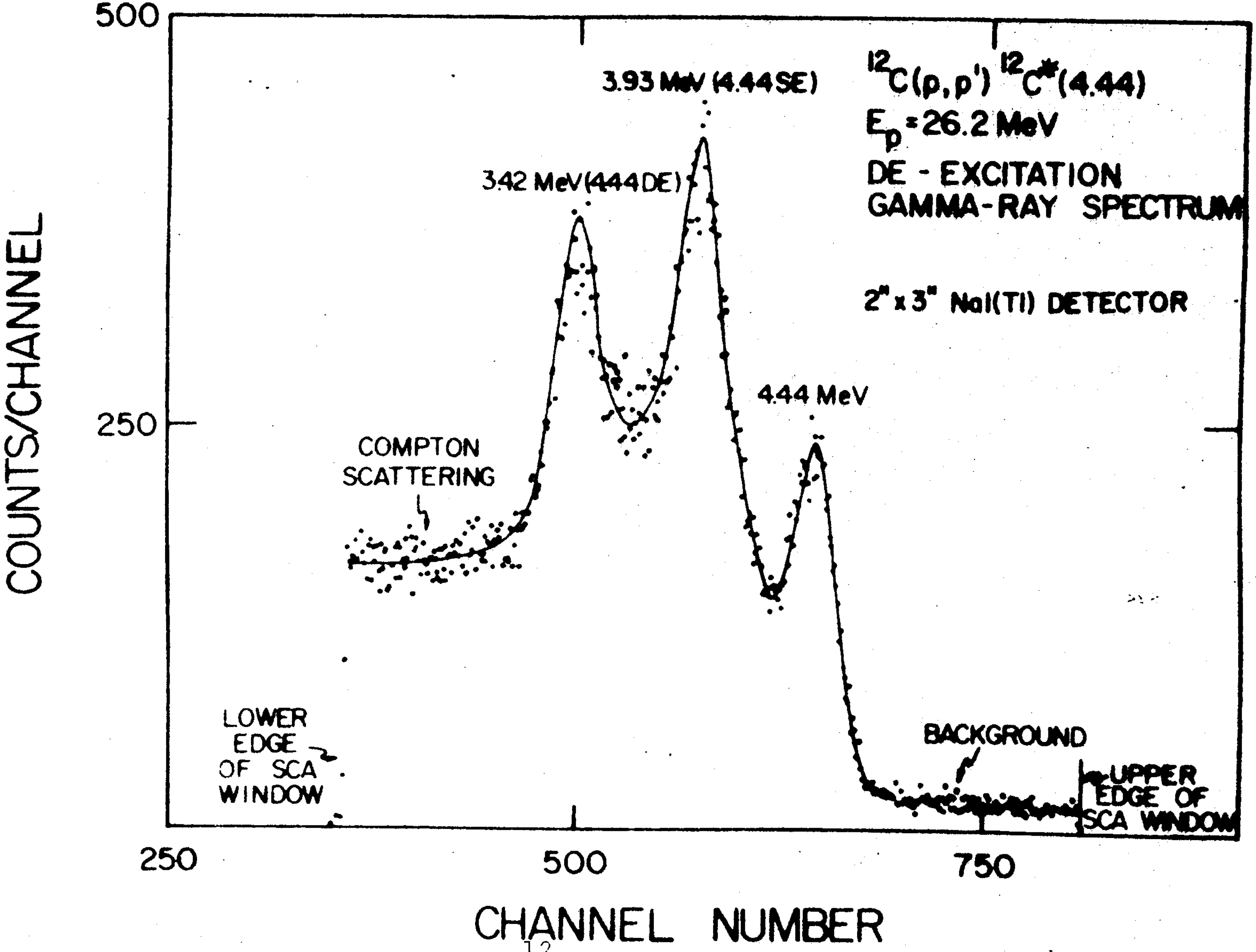

Figure III-16. Gamma-ray spectrum for the ^{12}C experiment, showing a typical setting of the pulse-height window. The Compton-scattering continuum extends to zero pulse-height below the lower edge of the window.

Table III-1. Measured values of the efficiency of the gamma-ray detector for the ^{12}C and ^{120}Sn experiments.

Experiment	E_p(MeV)	E_γ(MeV)	$d\Omega_\gamma$(sr)[a]	$\epsilon_\gamma d\Omega_\gamma$(sr)[b]
^{12}C	26.2	4.44	1.23×10^{-3}	$(6.10\pm0.55)\times10^{-3}$
^{12}C	40.0	4.44	1.23×10^{-3}	$(5.41\pm0.76)\times10^{-3}$
^{120}Sn	30.0	1.17	8.72×10^{-2}	$(2.24\pm0.11)\times10^{-2}$

a) Measured at the center of the 2" x 3" NaI (Tl) scintillator.

b) Efficiency for gamma rays in the pulse-height window.

Table III-2. Measured values for the strength of the ^{60}Co source.

Θ_{12}[a]	Counting Time(hrs)	Source Strength(sec^{-1})
180°	3.5	$(8.44\pm0.20)\times10^5$
180°	3.5	$(8.34\pm0.20)\times10^5$
90°	11.0	$(8.62\pm0.14)\times10^5$
	Average:	$(8.51\pm0.15)\times10^5$

a) Angle between the two detectors, one of which was a 3" x 3" NaI (Tl) scintillator at 18" from the source (measured to the center of the detector). The other detector was a 2" x 3" NaI (Tl) scintillator at 12" from the source.

For the 1.17 MeV gamma line from ^{120}Sn, the well-known method of γ-γ coincidences following the decay of ^{60}Co was used to prepare a standard source. The relevant decay scheme appears in Figure III-17. The 5.26 year ground state of ^{60}Co decays by β^- emission greater than 99% of the time to the 2.50 MeV 4^+ state in ^{60}Ni. This state subsequently decays via a gamma cascade through the 1.33 MeV 2^+ level. The two gamma rays, with energy 1.17 and 1.33 MeV, are always emitted in prompt coincidence. The angular correlation function for this cascade is well known (Kl 53, La 53). Suppose that we now prepare a source of strength S (unknown) and then observe coincidences between two gamma detectors which count the 1.17 and 1.33 MeV gamma rays, respectively. The number of singles events in the two detectors is:

$$N_1 = \epsilon_1 \Delta\Omega_1 \frac{St}{4\pi}$$
$$N_2 = \epsilon_2 \Delta\Omega_2 \frac{St}{4\pi} \qquad \text{(III.6)}$$

in a time t. During the same interval the number of coincidences is:

$$N_c = \epsilon_1 \Delta\Omega_1 \frac{St}{4\pi} \left[W(\theta_{12})\, \epsilon_2 \Delta\Omega_2 \right] \qquad \text{(III.7)}$$

where W(θ_{12}) is the angular correlation function and θ_{12} is the angle between the detectors. These equations may be solved for the source strength in terms of known quantities:

$$S = \frac{4\pi\, W(\theta_{12})}{t} \left[\frac{N_1 N_2}{N_c} \right] \qquad \text{(III.8)}$$

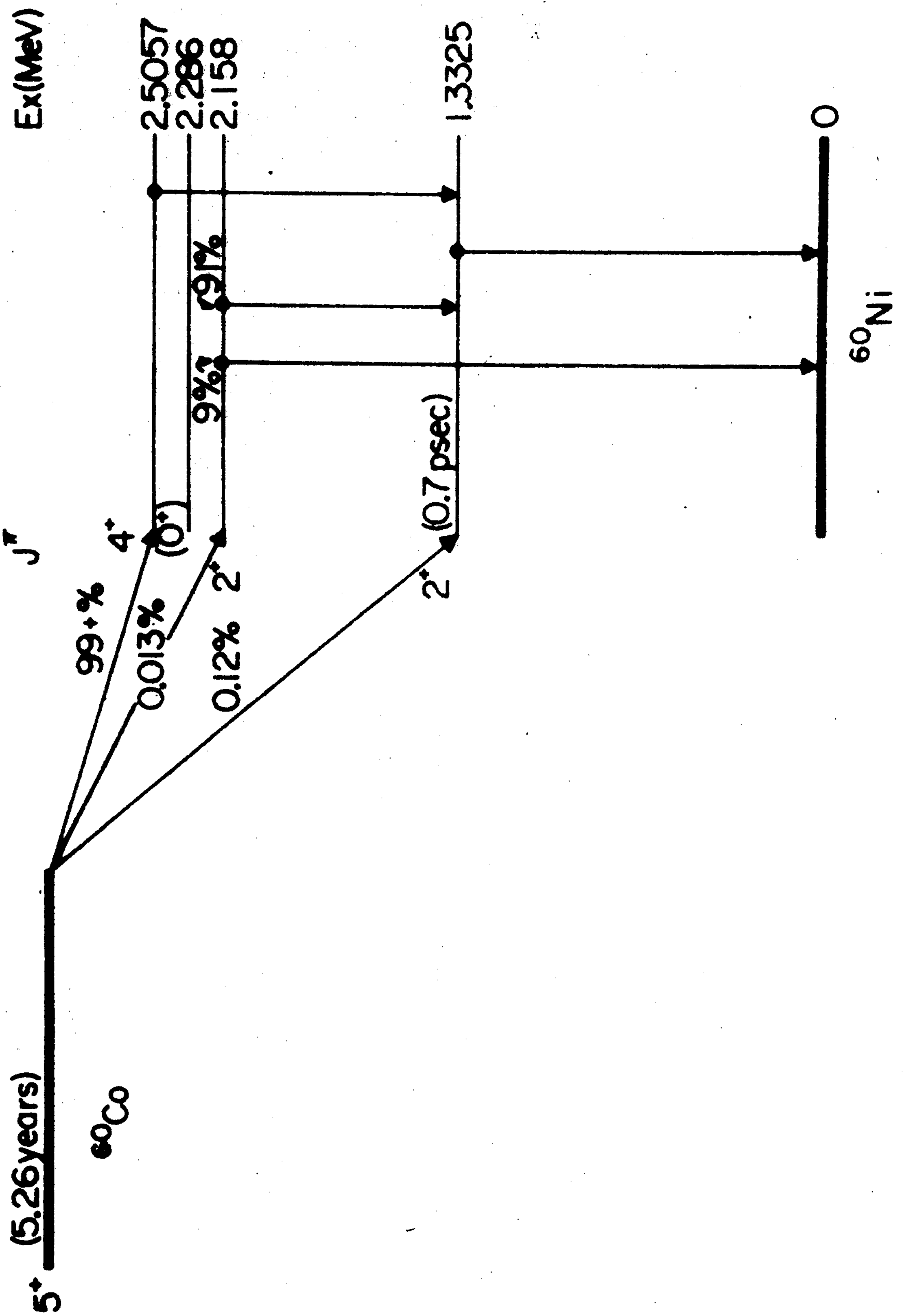

Figure III-17. Decay scheme for ^{60}Co.

The method is potentially quite accurate. The results obtained for two values of Θ_{12} are listed in Table III-2. The calibrated source was then used to determine the efficiency of the gamma detector for the ^{120}Sn experiment; the measured value appears in Table III-1.

III.D.3. Acceptance-Angle Corrections

In any real correlation experiment, the effect of the finite acceptance angles of the detectors on the measured correlation function must be considered. In the case of the present experiment, a gamma-ray detector subtending a finite angular range will accept some radiation from the $\Delta m=0$ and $\Delta m=\pm 2$ transitions (non-spin-flip events). If the proton detector also has finite size, the normal to the scattering plane become somewhat indeterminate since this detector then defines only a range of scattering planes. Corrections can be made for these effects if the complete correlation function $W(\phi_p, \theta_\gamma, \phi_\gamma)$ is known (Sc 64). However, the experimental determination of W is difficult since it requires coincidence measurements as a function of three angular variables. Fortunately, it is possible to deduce minimum and maximum values for the finite-aperture corrections from the gamma-perpendicular correlation alone (see Appendix B). The actual correction is taken to be the average of the maximum and minimum values, with an uncertainty equal to ±34% of the difference between them. That is, in the absence of better information it is assumed that the 'true' correction will be uniformly distributed between the maximum and minimum value.

For angular acceptances which are 'small enough', the correction (and its uncertainty) is also small. The interpretation of 'small enough' depends on the degree of difficulty of the experiment. It is always possible to reduce the angular acceptance to the point at which the correction becomes negligible. However, this involves a decrease in the coincidence count rate which cannot in general be regained by increasing the beam current because of the associated increase in the accidental coincidence rate (see Sec.III.D.4). Therefore, an appropriate balance must be struck between the uncertainty in the acceptance-angle correction and the statistical uncertainty in the number of coincidence events obtained in a given time. In the case of the ^{12}C experiment, it was possible to reduce the angular acceptance of both detectors to ±3° and still maintain a reasonable coincidence count rate. The uncertainty in the acceptance-angle correction was therefore quite small. For example, the correction for a spin-flip probability $S_1=0.10$ was $(-4.8\pm2.3) \times 10^{-3}$. For the more difficult ^{120}Sn experiment, it was necessary to increase the acceptance angle of the gamma detector to ±10° to obtain a reasonable count rate. The proton detector subtended a ±2° angular range because of physical limitations imposed by the small size of the Si(Li) detector. The corresponding correction for $S_1=0.10$ was $-(2.1\pm0.8) \times 10^{-2}$.

All experimental data were corrected for the effects of finite angular acceptance, and the associated uncertainty was included in the quoted experimental uncertainty.

III.D.4. Accidental Coincidences

The accidental coincidence rate between two detectors viewing a continuously radiating source is given by (Gr 66):

$$\langle N_A \rangle = \langle N_1 \rangle \langle N_2 \rangle \tau \tag{III.9}$$

where $\langle N_1 \rangle$ and $\langle N_2 \rangle$ are the average singles count rates in the two detectors and τ is the resolving time of the coincidence circuit. The same formula is applicable to the case of a pulsed source such as a cyclotron beam, except that must be replaced by an 'effective resolving time' $\tau_{eff.}$ which is generally much larger than τ . For example, it can easily be shown (Hr 67) that for a coincidence circuit with resolving time τ which is less than the time T between beam bursts and greater than the beam pulse width b:

$$\tau_{eff.} = T \tag{III.10}$$

Typical values for these parameters in the present experiment are τ = 1 nsec, b = 1 nsec, and T = 60 nsec. Note that $\tau_{eff.}$ is independent of τ if $b \leq \tau \leq T$ so that 50 nsec is 'as good as' 1 nsec. Of course, this is only true if there is no possibility of chance coincidences occurring between beam bursts. Figure III-11 illustrates the fact that this is not generally the case. There is a finite probability for chance coincidences to occur while the beam is off due to stray background radiation between beam bursts. Of particular interest is the small peak occurring midway between the major peaks in the time spectrum, which is due to a component of background radiation coming from the Faraday cup. By adjusting the distance from the target to the beam stop so that these events arrive between beam bursts (see Sec.III.A.5), it is possible to eliminate them from the chance coincidence rate (along with a major portion of the remaining continuous background between bursts) merely by placing a sufficiently small window around the 'true coincidence' peak. However, it is also clear from Figure III-11 that the reduction in the chance rate obtained in this manner is small compared to that which could be obtained if the resolving time were made smaller than the beam-pulse width.

The preceding discussion of the calculation of chance coincidence rates is valid if the beam pulses are perfectly uniform over the counting period. This is in fact not always the case with our cyclotron beam. Modulations with frequencies of 360 Hz and 100 kHz have been observed. Corrections can be made for the effects of these modulations. The result is invariably an increase in the effective resolving time (Hr 67). The formula for $\tau_{eff.}$ in the general case is quite complex, and it includes terms depending on the specific nature of the modulation which are difficult to measure accurately. For this reason, the following method was used to obtain an accurate measure of the number of accidental coincidences in each experimental run. The elastic and first excited state inelastic events were counted in singles and coincidence. Since the elastically scattered protons cannot be in true coincidence with a gamma ray, they provided an accurate measure of the accidental rate. If $N_{0s}(N_{0c})$ and $N_{1s}(N_{1c})$ are the total number of singles (coincidence) events for the elastic and first excited state inelastic scattering, respectively, we have for the accidental coincidences:

$$N_A = N_{0c}\left(\frac{N_{1s}}{N_{0s}}\right) \tag{III.11}$$

since the probability that an inelastically scattered proton will produce an accidental coincidence is exactly the same as that for an elastic event.

Although the method just discussed enables accurate chance coincidence subtraction, it is still desirable to reduce the chance rate to a minimum to obtain increased statistical accuracy in the data. This was particularly true for the ^{120}Sn experiment, in which a low true coincidence rate and a high accidental rate due to the large background of gamma radiation coming from the target conspired to make data collection more difficult. For this experiment, a significant reduction in the accidental rate was achieved by monitoring the gamma detector output on an oscilloscope set to 50 milliseconds full scale horizontal deflection and triggered at the line frequency. Under these conditions, any 360 Hz modulation of the beam was clearly evident from the time distribution of detector pulses. Minor adjustments to the tune of the cyclotron and to the external beam handling system were then made during the course of a run to keep the modulation to a minimum. In practice it was possible to eliminate the 360 Hz modulation almost entirely by careful adjustment. Some idea of the improvement in the accidental rate obtained in this manner may be inferred from a comparison of the observed number of accidental coincidences to that calculated from (III.9) using an effective resolving time equal to the period of the beam bursts. The average value of the ratio of these quantities was 3.88 for the unmonitored runs, and 1.36 for the monitored runs.

Finally, it can be seen from (III.9) that the accidental rate is proportional to the product of the singles rates in the two detectors and therefore to the square of the beam current. This fact may be used to determine the optimum beam current to use in order to obtain the best statistics on the number of real coincidences in a given counting time. Let T be the total coincidence counting rate, and let A be the accidental rate. Then R = T-A is the real coincidence rate. The fractional error in the total number of real coincidences obtained in a time t is determined by the propagation of errors:

$$\frac{err(Rt)}{Rt} = \frac{1}{Rt}\sqrt{(T+A)t} = t^{-1/2}\sqrt{\frac{1}{R}+\frac{2A}{R^2}} \qquad \text{(III.12)}$$

Since R is directly proportional to the beam current I, while A is proportional to I^2:

$$\frac{err(Rt)}{Rt} = t^{-1/2}\sqrt{\frac{k_1}{I}+k_2} \qquad \text{(III.13)}$$

This rather surprising result indicated that, everything else being equal, the best statistics on the number of real coincidences is obtained for very large beam currents such that the first term in (III.13) vanishes. Actually, other problems such as dead-time losses at high count rates and the effects of beam modulation have to be considered so that it is not advisable to use extremely high currents.

III.D.5. Pulse Pileup and Dead Time Losses

There are several ways in which coincidence events can be lost due to dead time or pulse pileup in the coincidence circuitry. For example, the TAC has an average dead time of 4 μsec every time it is started. Losses from this source were reduced by starting the TAC with pulses from the detector having the lower average count rate. Even so, the average start rate in some cases was as large as 10^4 sec^{-1}, which corresponds to a dead time loss of 4% (for an unmodulated cyclotron beam). This was the major source of dead time losses for the ^{12}C experiment.

Coincidence losses may also occur if a time conversion started by a 'true' event is stopped by an accidental coincidence from a preceding beam burst, or from the uncorrelated background between bursts. The probability that this will occur depends on the location of the 'true coincidence' peak in the time spectrum. For the ^{12}C experiment, the maximum equivalent dead time introduced by this effect was 200 nsec, which corresponds to a negligible 0.2% counting loss at the typical 10^4 sec^{-1} count rate. Because of the large background in the ^{120}Sn gamma-ray spectrum (see Figure III-18), the average stop rate was higher in this case ($\sim 10^5$ sec^{-1}). Therefore, the TAC conversion gain was set to 100 nsec full scale so that only events from the 'true coincidence' peak and a part of the continuous background between peaks were analyzed. The equivalent dead time from this source could then be neglected. It should be mentioned that the recovery time of the fast discriminators was very small ($\sim$10 nsec), so that coincidence losses due to the dead time of these units were also negligible.

Finally, coincidence losses can occur due to pulse pileup in the slow coincidence circuit. The shaping amplifiers used in this experiment had time constants of 0.25 μ sec, so that the total width of the output pulse was approximately 1 μsec. Two pulses arriving within this interval are algebraically added by the amplifier

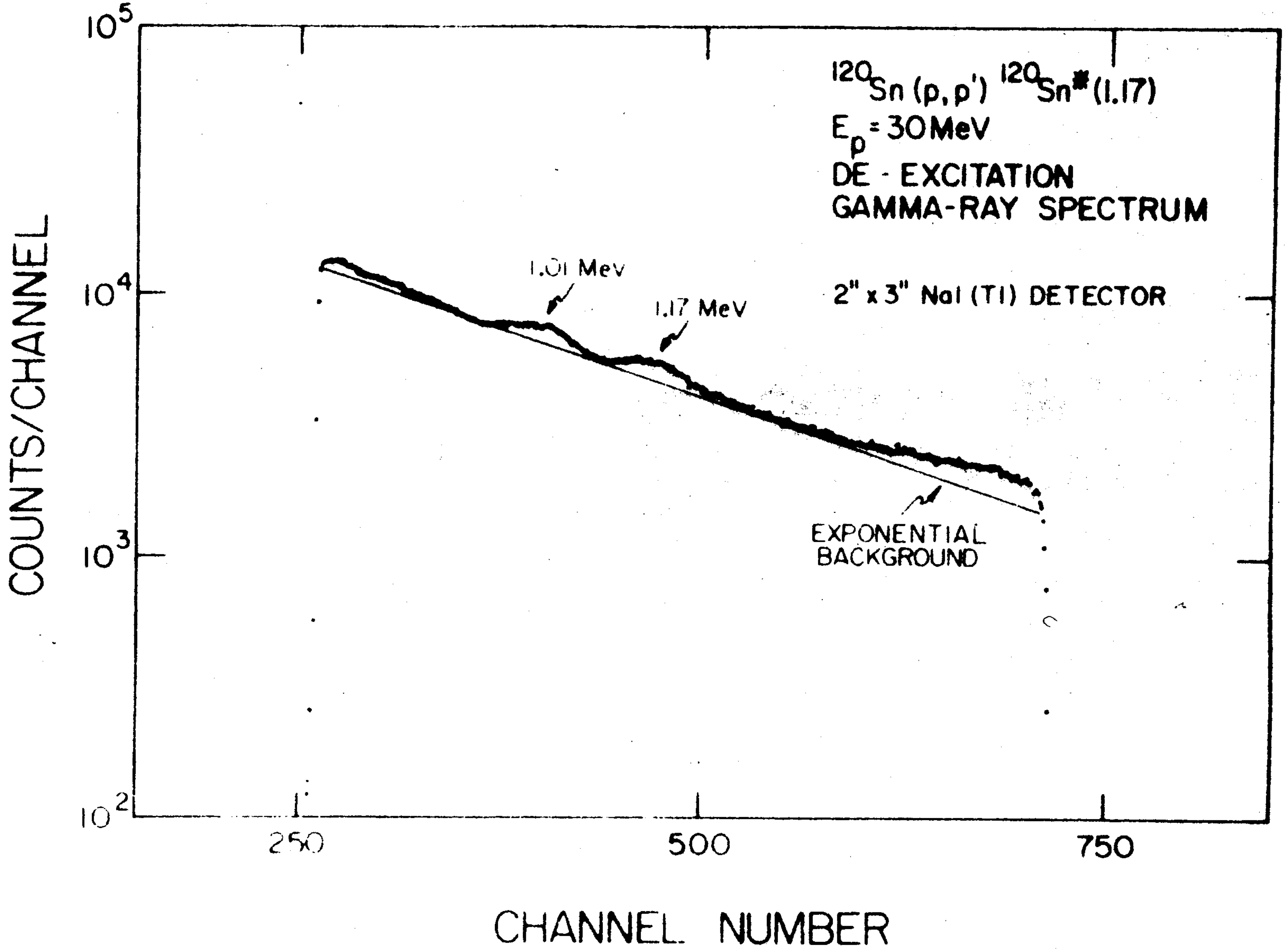

Figure III-18. Gamma-ray spectrum for the ^{120}Sn experiment, showing the exponential distribution assumed in the pileup calculations (Sec.III.D.5).

circuitry. The resulting output pulse will be rejected by the coincidence unit if it fails to satisfy the pulse height requirements or if the zero-crossover time is shifted by more than ±0.5 μsec (i.e., half the resolving time). This property has been used as the basis of pileup rejection circuits. A FORTRAN-IV code has been written for the SDS Σ7 computer at the cyclotron laboratory which simulates the behavior of the coincidence circuitry to calculate the rejection probability as a function of the count rate and the width of the pulse-height window. Two approximations were made in this calculation. First of all, the pulse shape at the output of the shaping amplifier was assumed to be of the form:

$$\begin{aligned} A(t) &= A_0\, t/t_0 & &(0 \leq t \leq t_0) \\ A(t) &= A_0 \left(2 - t/t_0\right) & &(t_0 \leq t \leq 2.5t_0) \\ A(t) &= -\frac{A_0}{2} \left(e^{-[2.5 - t/t_0]}\right) & &(2.5t_0 \leq t \leq 10t_0) \end{aligned} \qquad \text{(III.14)}$$

where A(t) is the amplitude of the pulse at a time t and t_0 is the amplifier time-constant (typically 0.25 μsec). This is a reasonably good approximation (see, for example, the ORTEC catalog #1001*). Secondly, the amplitude spectrum of the detector pulses was described by an exponential distribution (Figure III-18). A set of pulses with this amplitude spectrum was distributed in time according to the interval distribution (Ev 55) for the average count rate.

---

*ORTEC, Inc.; Oak Ridge, Tennessee.

Whenever one of these pulses overlapped a reference pulse corresponding to a 'true' event, the pulse shapes were added algebraically and the resulting sum pulse was rejected if it did not meet either the pulse-height or the zero-crossover time requirements. The results were used to correct for coincidence losses due to pulse pileup. A typical value of the rejection probability for the ^{120}Sn experiment was 2% at an average count rate of 10^5 sec^{-1} and for an unmodulated beam.

In the previous discussion, an unmodulated cyclotron beam was assumed. In point of fact, the beam was not steady (see Sec.III.D.4). A correction must be made for the effects of beam modulation. Fortunately, this correction can be expressed in terms of the ratio of experimental to calculated accidental coincidence rate. Let τ_d be the dead time of the coincidence unit, and let a(T) be the average count rate over the interval between T and T+dT, where dT $\gg \tau_d$. It is also assumed that dT can be selected so that the count rate does not vary appreciably over this interval. The fraction of intervals shorter than τ_d (i.e., the fraction of lost events) is (Ev 55):

$$f(T) = 1 - e^{-a(T)\tau_d} \approx a(T)\,\tau_d \qquad \text{(III.15)}$$

The approximation is quite good since a(T) τ_d is typically $<$ 0.1. The total number of events during dT is:

$$N_T = a(T)dT \qquad \text{(III.16)}$$

and the total number of lost events is simply:

$$N_L = a^2(T)\,\tau_d\,dT \qquad \text{(III.17)}$$

The fractional dead time loss f is obtained by integrating N_T and N_L over the counting period and dividing:

$$f = \frac{\int_0^{T_f} a^2(T)\,dT}{\int_0^{T_f} a(T)\,dT}\,\tau_d = \frac{<a^2>}{<a>^2}\,<a>\,\tau_d \qquad \text{(III.18)}$$

Since a(T) is proportional to q (T), the average charge per beam burst:

$$f = \frac{<q^2>}{<q>^2}\,<a>\,\tau_d \qquad \text{(III.19)}$$

In the case of uniform beam, the first factor reduces to one. For a modulated beam this correction factor can be easily related to the ratio of experimental to calculated accidental rates by applying a parallel argument to (III.9) above (Sc 64). The resulting expression for f is:

$$f = \frac{N_A^{Exp}}{N_A^{Th}}\,<a>\,\tau_d = f_0\,<a>\,\tau_d \qquad \text{(III.20)}$$

where N_A^{Th} is calculated from (III.9) and (III.10). The correction factor f_0 was applied to all dead-time and pulse pileup corrections. The maximum value of the corrected dead time was 14% for the ^{12}C experiment, and 8% for the ^{120}Sn experiment.

III.D.6. Analysis of Experimental Uncertainties

The major sources of error in the determination of the relative spin-flip probability are: (1) the statistical uncertainty in the number of real coincidence events, (2) the uncertainty in the solid-angle correction, (3) the uncertainty in the dead time correction, and (4) possible errors in the positioning of the two detectors. The first of these always made the largest contribution to the final experimental uncertainties quoted in this experiment.

The expression for the statistical uncertainty in the number of real events is readily derived using propagation of errors. In the notation of Sec.III.D.4 the number of real events R is;

$$R = N_{1c} - N_{oc}\left(\frac{N_{1s}}{N_{os}}\right) \qquad \text{(III.21)}$$

so that the uncertainty in R is:

$$\mathrm{err}\,(R) = \sqrt{N_{1c} + \left(\frac{N_{oc}\,N_{1s}}{N_{os}}\right)^2\left(\frac{1}{N_{oc}} + \frac{1}{N_{os}} + \frac{1}{N_{1s}}\right)} \qquad \text{(III.22)}$$

Since the number of singles events is always large compared to the number of coincidence events, this reduces to:

$$\mathrm{err}\,(R) = \sqrt{N_{1c} + \left(\frac{N_{oc}\,N_{1s}}{N_{oc}}\right)^2\left(\frac{1}{N_{oc}}\right)} = \sqrt{N_{1c} + \frac{A^2}{N_{oc}}} \qquad \text{(III.23)}$$

The uncertainty in the solid angle correction has been discussed before and a derivation of the relevant expressions appears in Appendix B. These formulae may also be used to determine the contribution from angular positioning errors. The estimated magnitude of these errors has already been mentioned in Sec.III.A and Sec.III.B. The corresponding uncertainties in the spin-flip probability were negligible in all cases, since the angular positioning uncertainties were always much smaller than the angle subtended by the detectors.

The uncertainty in the dead time correction is more difficult to determine. In particular, the quantity N_A^{Th} appearing in (III.20), which is the number of accidentals to be expected with an unmodulated cyclotron beam, is somewhat uncertain due to complications introduced by accidental coincidences occurring between beam bursts. These events were neglected in the calculation of N_A^{Th}. It is estimated from the time spectrum presented in Fig. III-11 that a possible ±10% uncertainty may be present in the calculated value. The corresponding 10% uncertainty in the dead time correction made only a very small contribution to the quoted errors, since the correction itself was always small (see Sec.III.D.5).

The only major source of error in the determination of the absolute spin-flip probability was the uncertainty in the gamma-ray detector efficiency. Contributions from other sources such as the target thickness or the current integration are canceled in taking the ratio of real coincidences to singles. In the case of the ^{12}C experiment, the error in the efficiency measurement was large (10-15%)

since it is not easy to make a calibrated source of 4.44 MeV gamma rays. The indirect method used (see Sec.III.D.2) provides many opportunities for error to creep in. The major sources of error were the integration of the proton and gamma-ray angular distributions, and the determination of the number of 4.44 MeV gamma rays in the window (a significant background was present (Figure III-16) and had to be subtracted). The uncertainties introduced were quite large as reflected in the final computed errors.

The ^{120}Sn normalization was much less uncertain because we could more easily prepare a calibrated source (see Sec.III.D.2). The only major sources of error were the statistical uncertainty in the number of true coincidences and the uncertainty in the solid-angle corrections. Both these errors were made small by reducing the solid angle and counting for a long time (~12 hours). The resulting uncertainty in the source strength was ±2%. An additional uncertainty was introduced into the efficiency calculation due to possible errors in locating the window on the gamma-ray spectrum (Figure III-18) so that the total uncertainty in the normalization was estimated to be ±5%.

In summary, it should be pointed out that the error bars in the spin-flip distributions to be presented in the following chapters take into account all the relative errors mentioned above and are to be treated as standard deviations. The errors in the absolute normalization are not included and must be treated as uncertainties in the indicated absolute scale.

CHAPTER IV

OPTICAL MODEL ANALYSIS

IV.A. Elastic Scattering Wave Functions and the Optical Model

The tacit assumption behind the perturbation method which forms the basis of the DWBA treatment of direct reactions is that the elastic scattering, i.e., the major part of the nucleon-nucleus interaction, can be treated exactly. In practice, this is not the case. The elastic scattering is treated in the optical model approximation (Jo 63). The n-body problem of a free nucleon (the projectile) scattering from an ensemble of bound nucleons (the target) is approximated by a much simpler one-body problem in which the total interaction is replaced by an equivalent complex spherical potential. The real part of this optical model potential represents an average elastic interaction between the projectile and the target nucleons and the imaginary part represents the absorption of the projectile into open channels other than elastic scattering, e.g., (p,n) reactions, inelastic scattering, etc.

The general form of the potential used is:

$$\begin{aligned} U(r) = {} & U_c(r) - V f(x_R) - i\left(W - 4W_D \frac{d}{dx_I}\right) f(x_I) \\ & + \left(\frac{\hbar}{m_\pi c}\right)^2 (V_{so} + iW_{so})\, \vec{\sigma}\cdot\vec{\ell}\, \left(\frac{1}{r}\frac{d}{dr}\right) f(x_{so}) \end{aligned} \qquad \text{(IV.1)}$$

The functions $f(x_k)$ are of the Woods-Saxon (or Fermi) form:

$$f(x_k) = (e^{x_k}+1)^{-1} \quad ; \quad x_k = (r - r_k A^{1/3})/a_k \; ; \quad k = (R, I, so)$$

representing a diffuse well of mean radius $r_k A^{1/3}$. The 'diffuseness' parameter a_k is a measure of the width of the transition region at the edge of the well where the potential is changing rapidly. The derivative of this form represents a 'surface' interaction since the derivative peaks at the mean radius. In this case, the diffuseness parameter is related to the width of the surface peak.

$U_c(r)$ is the Coulomb potential between a point charge (e) and a uniformly charged sphere of radius $r_c A^{1/3}$ and charge (Ze):

$$U_c(r) = \begin{cases} Ze^2/r & (r \geq r_c A^{1/3}) \\ \dfrac{Ze^2}{2 r_c A^{1/3}}\left(3 - \dfrac{r^2}{r_c^2 A^{2/3}}\right) & (r \leq r_c A^{1/3}) \end{cases} \qquad \text{(IV.2)}$$

The 'Coulomb radius' r_c is taken to be 1.20F for proton scattering (Sa 67).

The spin-orbit term is of the Thomas type; l and o refer to the orbital and spin angular momentum of the projectile, respectively. The normalization constant, which contains the pion mass m_π, has the convenient value $\left(\frac{\hbar}{m_\pi c}\right)^2 = 2.0\ F^2$.

The DWBA code computes the elastic scattering wave function as a solution to the Schrödinger equation for a projectile scattering from the potential U(r). The various parameters which must be specified in the input to the program are determined by fitting the appropriate elastic scattering data. This means that the exit channel parameters should be chosen to fit the elastic scattering data at the exit channel energy (the beam energy plus the Q-value for the reaction). If taken literally, it also means that one should fit elastic scattering data from the target in its excited state. The first of these requirements is relatively easy to meet. It involves a study of the energy dependence of the parameters over a reasonably small range of incident proton energies. Since the local potential U(r) is used to approximate the nonlocal projectile-nucleus interaction, one expects a variation of the parameters with the incident beam energy (Jo 63). The effect of this variation on the exit channel parameters could be significant in the case of ^{12}C because of the large Q-value to the first excited state (-4.44 MeV), and it should be less important for ^{120}Sn (Q=-1.17 MeV). The second requirement is clearly impossible to meet. Instead, it is assumed that the elastic scattering from the excited state is, in fact, not too dissimilar from scattering from the ground state. This neglects, for example, the effects of a possible spin-spin interaction in the exit channel where the target has nonzero spin. However, this type of coupling is expected to be small provided that the target mass is much greater than the spin of the state in question (Jo 63), and it has been shown to be negligible for nuclei as light as ^{24}Mg and ^{27}Al (Ro 61).

IV.B. The Search Procedure

Optical model analyses were performed with the search code GIBELUMP* on the SDS Σ 7 computer at the cyclotron laboratory. This code varies the potential depths and geometrical parameters, singly or in any combination, to obtain a fit to the experimental elastic scattering data. The criterion imposed on the fit is the minimization of the quantity $\chi_T^2 = \chi_\sigma^2 + \chi_P^2$, where:

$$\frac{\chi_\sigma^2}{N_\sigma} = \frac{1}{N_\sigma} \sum_i^{N_\sigma} \left\{ \left[\sigma_{th}(i) - \sigma_{exp}(i) \right] / \Delta\sigma_{exp}(i) \right\}^2$$

$$\frac{\chi_P^2}{N_P} = \frac{1}{N_P} \sum_i^{N_P} \left\{ \left[P_{th}(i) - P_{exp}(i) \right] / \Delta P_{exp}(i) \right\}^2 \qquad \text{(IV.3)}$$

N_σ (N_p) is the number of experimental cross section (polarization) data points, $\sigma_{th}(i)$ and $\sigma_{exp}(i)$ ($P_{th}(i)$ and $P_{exp}(i)$) are the theoretical and experimental cross section (polarization) at center-of-mass angle θ_i , and $\Delta\sigma_{exp}(i)$ ($\Delta P_{exp}(i)$) is the experimental uncertainty in $\sigma_{exp}(i)$ ($P_{exp}(i)$) .

It is well known (Ba 64) that the optical model parameters obtained in this way exhibit certain ambiguities. That is, there exist many sets of potentials which predict essentially the same elastic scattering. For example, if the depth of the real well V and the real radius r_R are

---

[*] Unpublished FORTRAN-IV computer code written by F.G. Perey and modified by R.M. Haybron at Oak Ridge National Laboratory.

varied in such a way as to keep the product Vr_R^2 constant, it is possible to obtain a series of potentials which give equivalent fits (Ba 64) to the elastic data. In addition, to this 'continuous' correlation, there exists a 'discrete' ambiguity in V corresponding to the fact that potentials with different numbers of half-wave-lengths of the optical model wave functions in the interior of the nucleus give the same asymptotic phase shifts, and hence predict the same elastic scattering. Finally, it should be mentioned that these ambiguities are by no means limited to the real part of the potential. The imaginary well depth and diffuseness are closely correlated (Gl 65), as are the imaginary volume (W) and surface (W_D) well depths (Sa 67).

The combined effect of these ambiguities is to make simultaneous searches on all the parameters unfeasible since the search procedure tends to become unstable. That is, the parameters rapidly become unreasonable while effecting no significant change in χ_T^2. It has been found that these 'runaway' searches can be avoided simply by doing a 'patterned' search using groups of uncorrelated or weakly correlated parameters (Pr 68). The parameters were divided into three groups, each of which contained a potential depth from one of the three parts of the potential (real, imaginary, spin-orbit), a radius parameter from another part, and a diffuseness parameter from the remaining part. The parameters in a particular group were varied simultaneously, with the remaining parameters held fixed.

When a minimum value for X_T^2 was found, the same procedure was followed for the other groups. The entire process was repeated until it converged, i.e., until no significant change in X_T^2 was evident after an iteration.

IV.C. Optical Model Parameters for $^{12}C(p,p)^{12}C$

The ^{12}C optical model potentials used in the DWBA calculations were determined from an analysis of published elastic cross section (Di 63,Fa 67,Bl 66a) and polarization (Bl 66a,Cr 66,Cr 66a) data taken at 26.2, 40.0, and 49.5 MeV. Preliminary searches were made with volume imaginary (W_D=0) and surface imaginary (W=0) potentials, and also with a mixture of the two forms. In the latter case, it was found that W and W_D were strongly correlated in such a way that the search code tended to drive one or the other of them to zero, depending on initial conditions. This correlation has been previously noted for elastic scattering from ^{9}Be and ^{12}C (Sa 67). For this reason, pure surface imaginary potentials, which seemed to give somewhat better fit than volume types, were used throughout the final analysis. Furthermore, it was found that the optimum value for the imaginary spin-orbit depth W_{so} tended to be very close to zero, in agreement with previous observations (Sa 67,Gl 67, Fr 67). It was therefore set equal to zero in the remaining searches.

The other nine parameters were allowed to vary, using the patterned search procedure outlined above. Since we were particularly interested in spin-dependent effects, it was decided to bias the searches toward fitting the polarization data. For this reason, whenever two sets of parameters gave equivalent X_T^2 preference was given to the set resulting in smaller X^2p. The results of this bias are apparent in the X^2 values for the final parameters, which appear in Table IV-1. The corresponding fits, shown in Figures IV-1 to IV-3, illustrate the fact that it is difficult to understand the ^{12}C elastic scattering data in terms of the optical model. It was possible to obtain good fits to either the cross section or the polarization data alone, but attempts to fit them simultaneously resulted in rather unsatisfactory compromises. Discrepancies of this nature have been noticed in previous analyses of ^{12}C elastic data (Sa 67). It has been suggested that they may be a result of the rather strong coupling between the ground state and the first excited state of ^{12}C. However, calculations in which the equations coupling these states were solved explicitly indicated that this was not the case (Sa 67). It seems, then, that these difficulties may be related to the failure of the assumptions of the optical model for such a light nucleus; in particular, the averaging implicit in the potential scattering model may be an invalid procedure for a system with only twelve nucleons.

The energy dependence of the parameters obtained is illustrated in Figure IV-4. The 'error bars' represent the limits over which the parameter can be varied with less

Table IV-1. Optical model parameters which produced the fits to the ^{12}C elastic data shown in Figures IV-1 to IV-3.[a]

E_p(MeV)	V(MeV)	r_R(F)	a_R(F)	W_D(MeV)	r_I(F)	a_I(F)	V_{SO}(MeV)	r_{SO}(F)	a_{SO}(F)	$\frac{X^2_\sigma}{N_\sigma}$	$\frac{X^2_p}{N_p}$[b]
26.2	48.48	1.07	0.634	3.33	1.34	0.682	7.34	1.01	0.485	22	7
40.0	45.06	1.08	0.689	5.19	1.25	0.533	7.45	1.08	0.485	22	18
49.5	43.36	1.08	0.712	6.61	1.21	0.527	8.16	1.02	0.531	56	6

---

[a] As mentioned in the text, the final calculations were performed with a surface imaginary form (W=0.0) and a real spin-orbit term (W_{SO}=0.0).

[b] The experimental uncertainties quoted in (Di 63, Fa 67, Bl 66a, Cr 66, and Cr 66a) were used in the computation of X^2_σ and X^2_p. N_σ (N_p) is the number of cross section (polarization) data points.

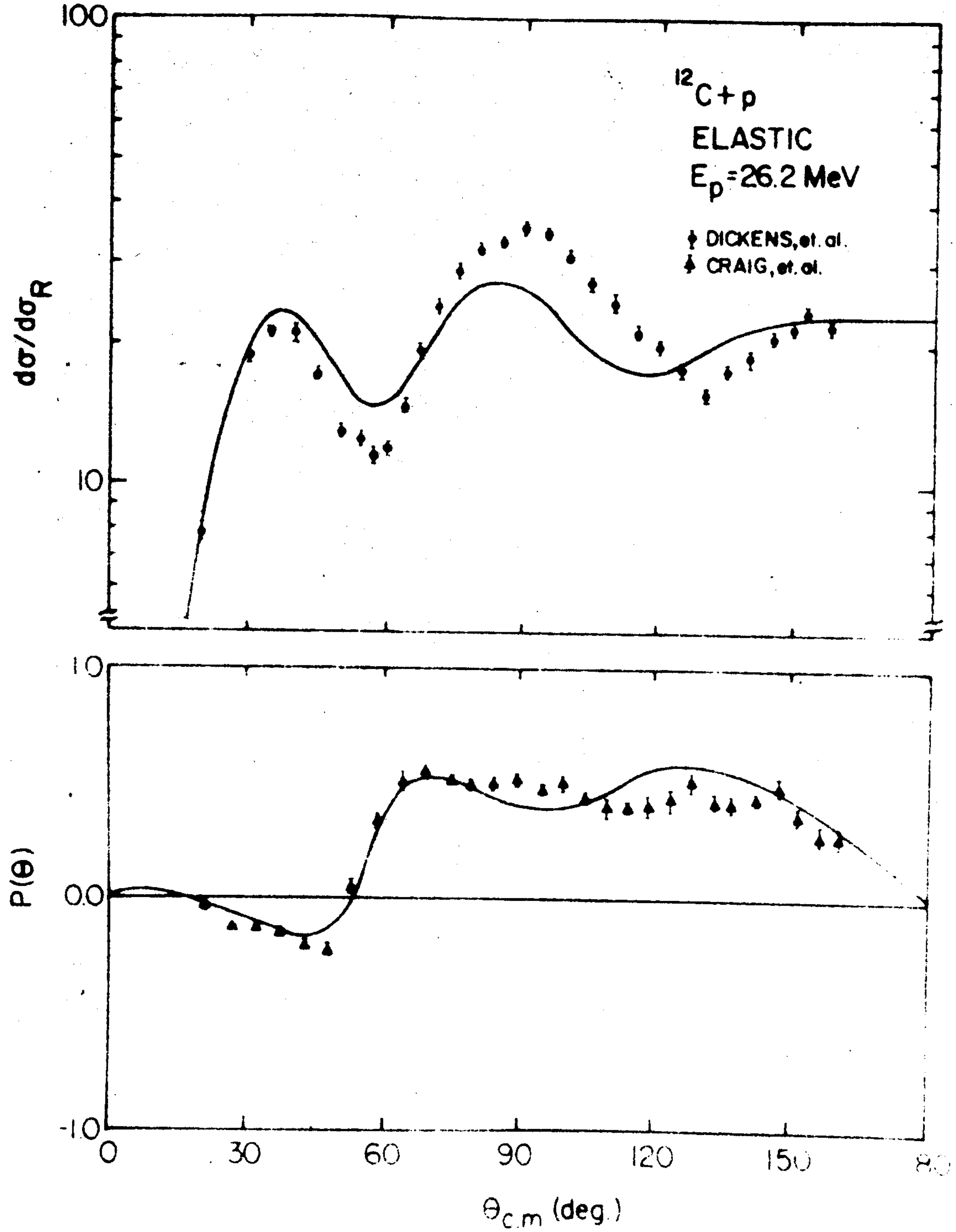

Figure IV-1. ^{12}C elastic cross section and polarization fits obtained for the 26.2 MeV data (Di 63, Cr 66) with the optical model parameters of Table IV-1. Cross sections shown in ratio to Rutherford scattering.

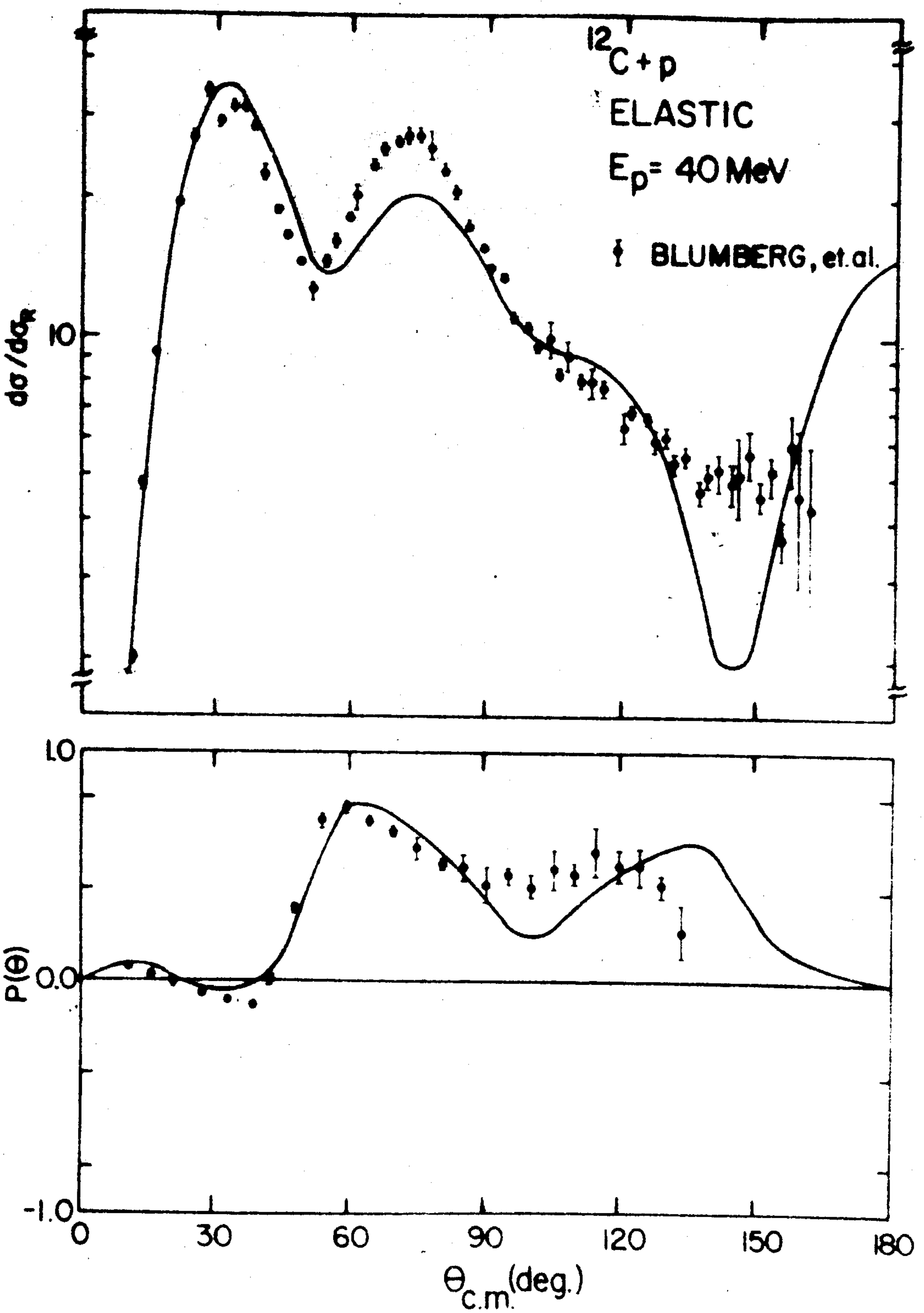

Figure IV-2. ^{12}C elastic cross section and polarization fits obtained for the 40.0 MeV data (Bl 66a) with the optical model parameters of Table IV-1.

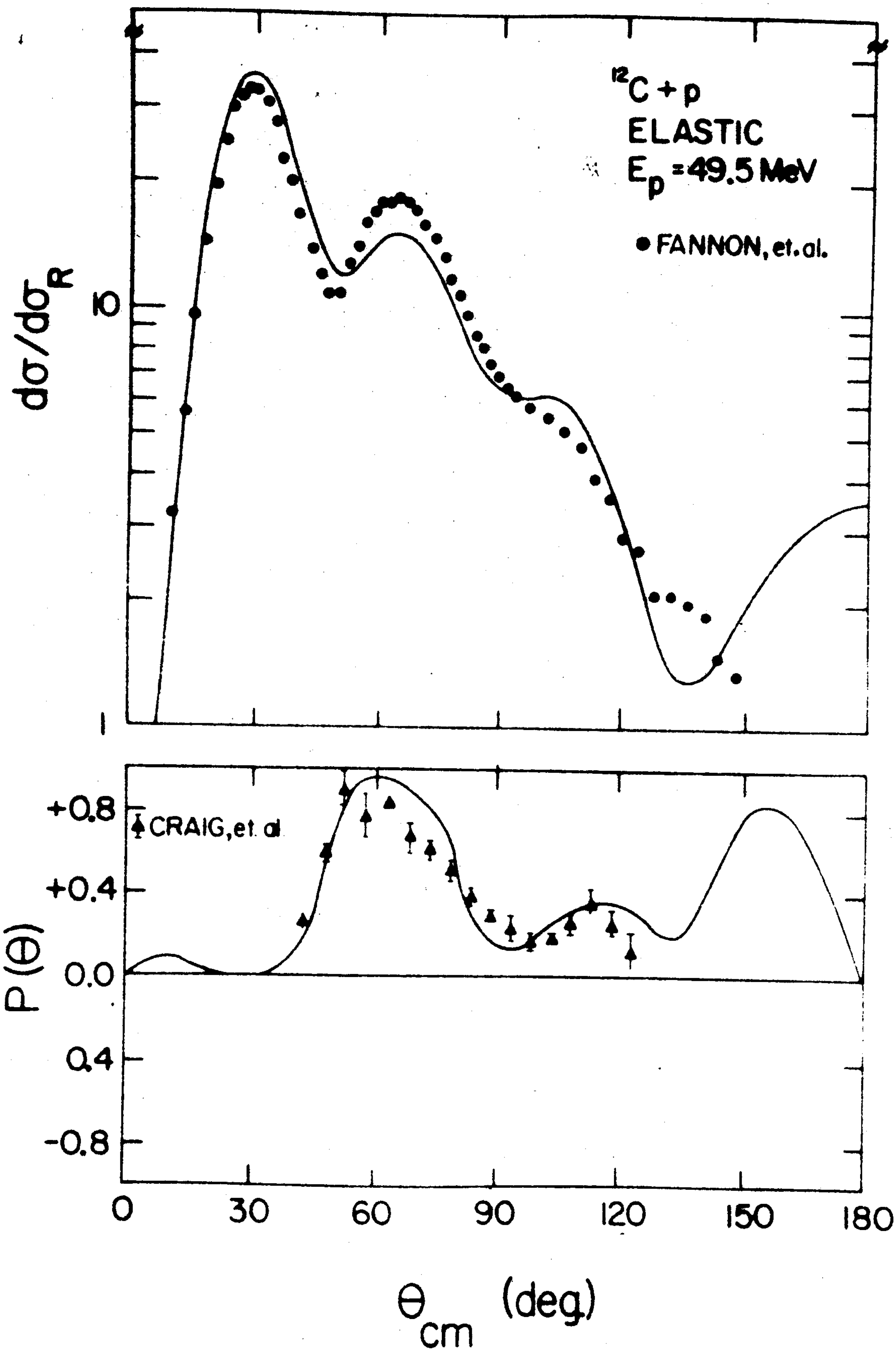

Figure IV-3. ^{12}C elastic cross section and polarization fits obtained for the 49.5 MeV data (Fa 67, Cr 66a) with the optical model parameters of Table IV-1.

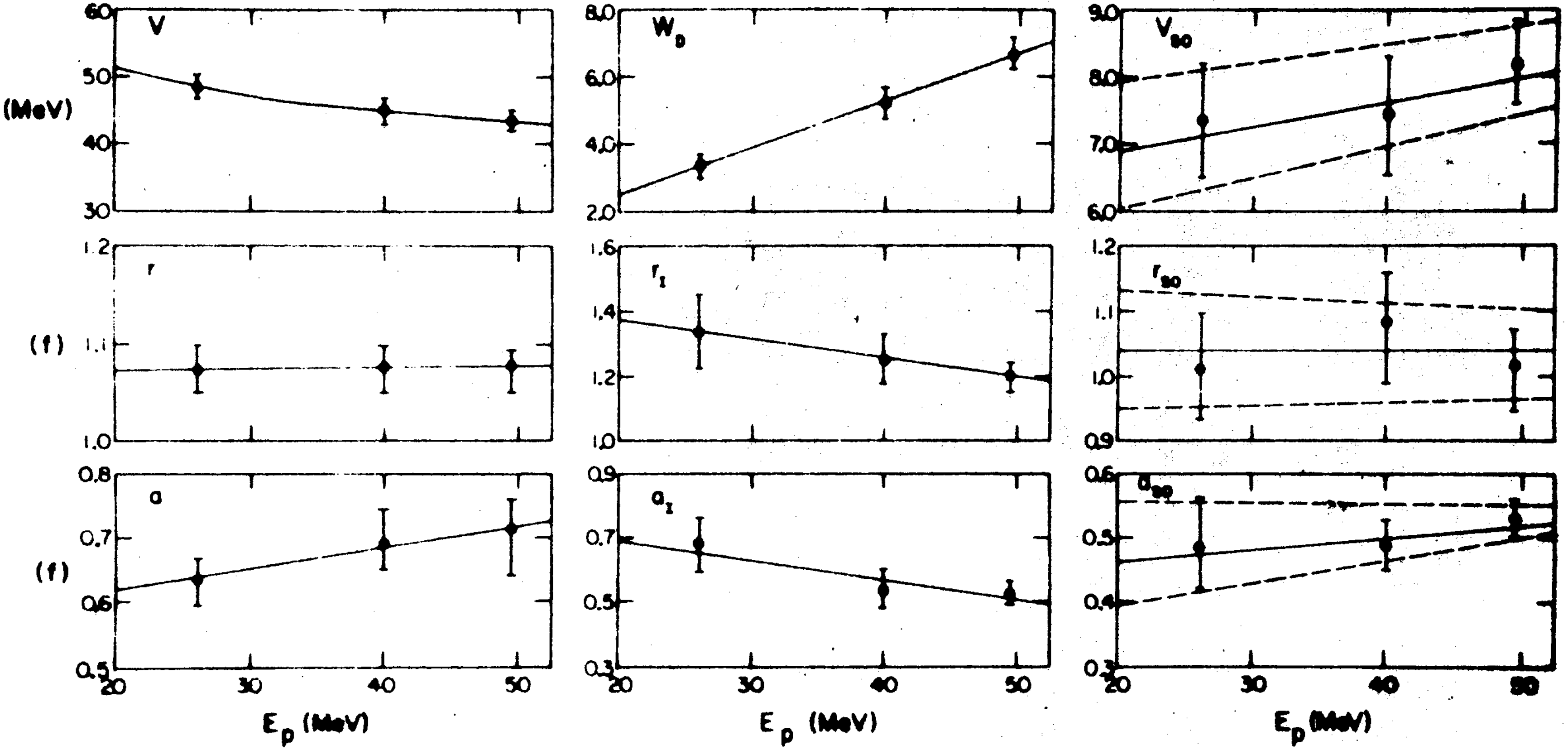

Figure IV-4. Energy dependence of ^{12}C optical-model parameters. 'Error bars' indicate the range over which the parameter can vary with less than 25% change in X_T^2.

than 25% increase in X^2_T. These limits were determined by searching on a single parameter, leaving all others fixed at their optimum values. A typical 'map' of X^2-space obtained in this manner is shown in Figure IV-5 for the spin-orbit diffuseness parameter.

IV.D. Optical Model Parameters for ^{120}Sn(p,p)^{120}Sn

Complete elastic scattering data (cross section and polarization) is available for ^{120}Sn at 30 MeV (Cr 64,Ri 64). The data have been analyzed in the optical model by several authors (Gr 66a,Sa 67b). The resulting potentials are all quite similar and the fits obtained are uniformly good. A selected list of some of these potentials appears in Table IV-2. Figure IV-6 illustrates a typical fit to the 30 MeV data.

The potentials of Table IV-2 were used in the ^{120}Sn DWBA analyses. The same parameters were used in both the entrance and exit channels since there is not enough experimental data to determine the energy dependence of the parameters. However, the low Q-value to the first excited state (-1.17 MeV) leads one to believe that this will not lead to serious error in the DWBA calculations.

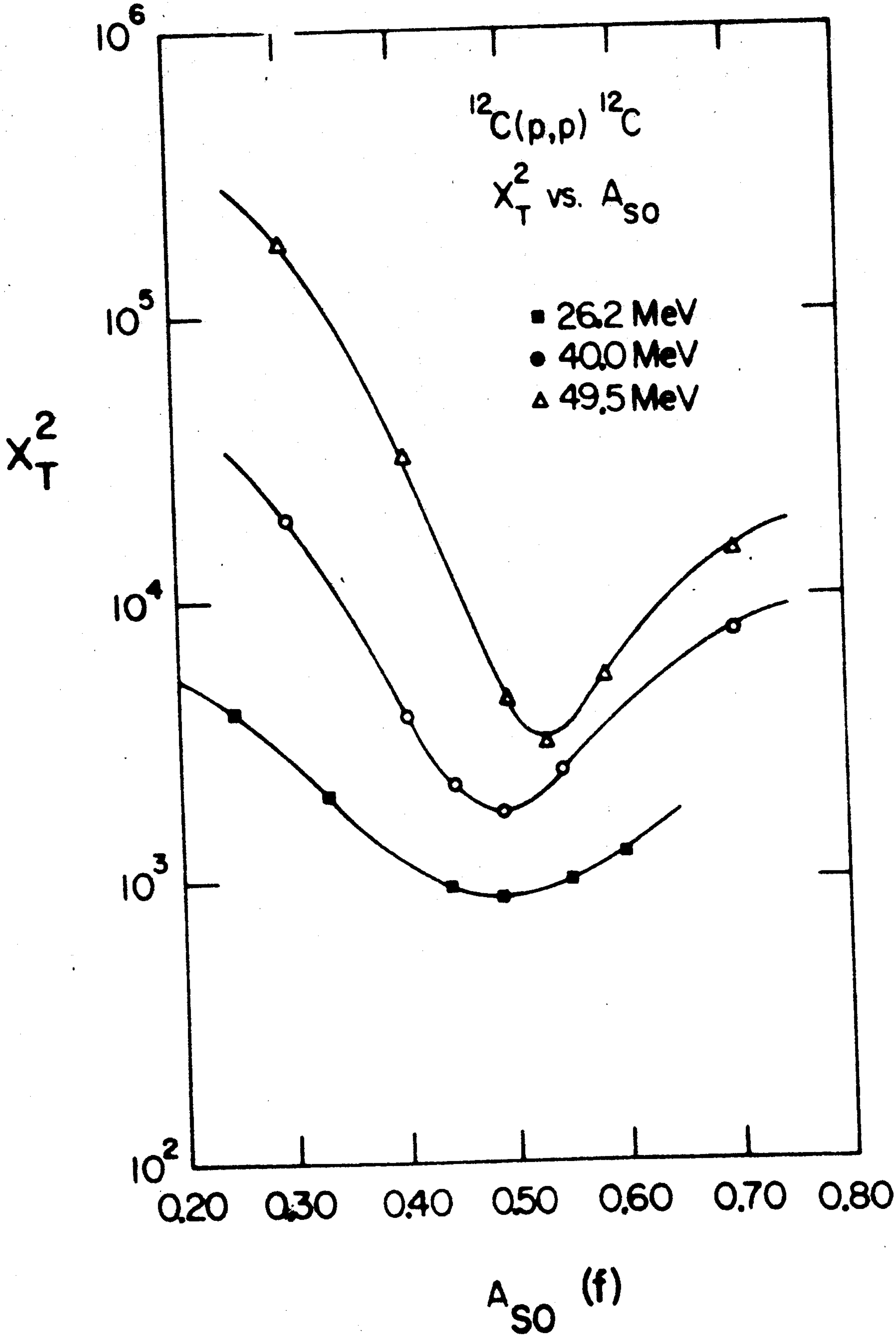

Figure IV-5. Typical 'map' of X^2 space for the spin-orbit diffuseness parameter.

Table IV-2. Optical-model parameters for elastic proton scattering from ^{120}Sn at 30 MeV.[a]

	V	r_R	a_R	W	W_D	r_I	a_I	V_{SO}	r_{SO}	a_{SO}	$\frac{X^2_\sigma}{N_\sigma}$	$\frac{X^2_p}{N_p}$
1A[b]	51.1	1.20	0.700	0.40	5.96	1.25	0.700	5.97	1.10	0.700	10.1	8.3
1B	50.7	1.20	0.700	1.25	8.51	1.25	0.700	6.20	1.17	0.700	7.1	6.9
2A	51.4	1.17	0.725	2.59	7.49	1.31	0.647	6.12	1.17	0.725	5.9	18.8
2B	52.0	1.16	0.703	3.00	7.23	1.33	0.643	6.19	1.16	0.703	7.7	15.6
2C	51.4	1.17	0.713	2.07	7.47	1.30	0.684	6.50	1.07	0.828	4.35	19.9
2D	51.5	1.17	0.720	2.57	7.53	1.31	0.650	6.17	1.16	0.744	5.5	18.8
2E	51.0	1.18	0.718	2.21	7.30	1.31	0.675	6.35	1.06	0.774	4.9	18.9

a) Well-depth parameters are given in MeV, and the geometrical parameters in units of fermis (F). In all cases, the imaginary part of the spin-orbit potential (W_{SO}) was set equal to zero and the Coulomb radius was taken to be 1.20F.

b) Reference numbers indicate the source of the parameter set. 1A and 1B were taken from (Gr 66a). The remaining parameter sets were taken from (Sa 67b).

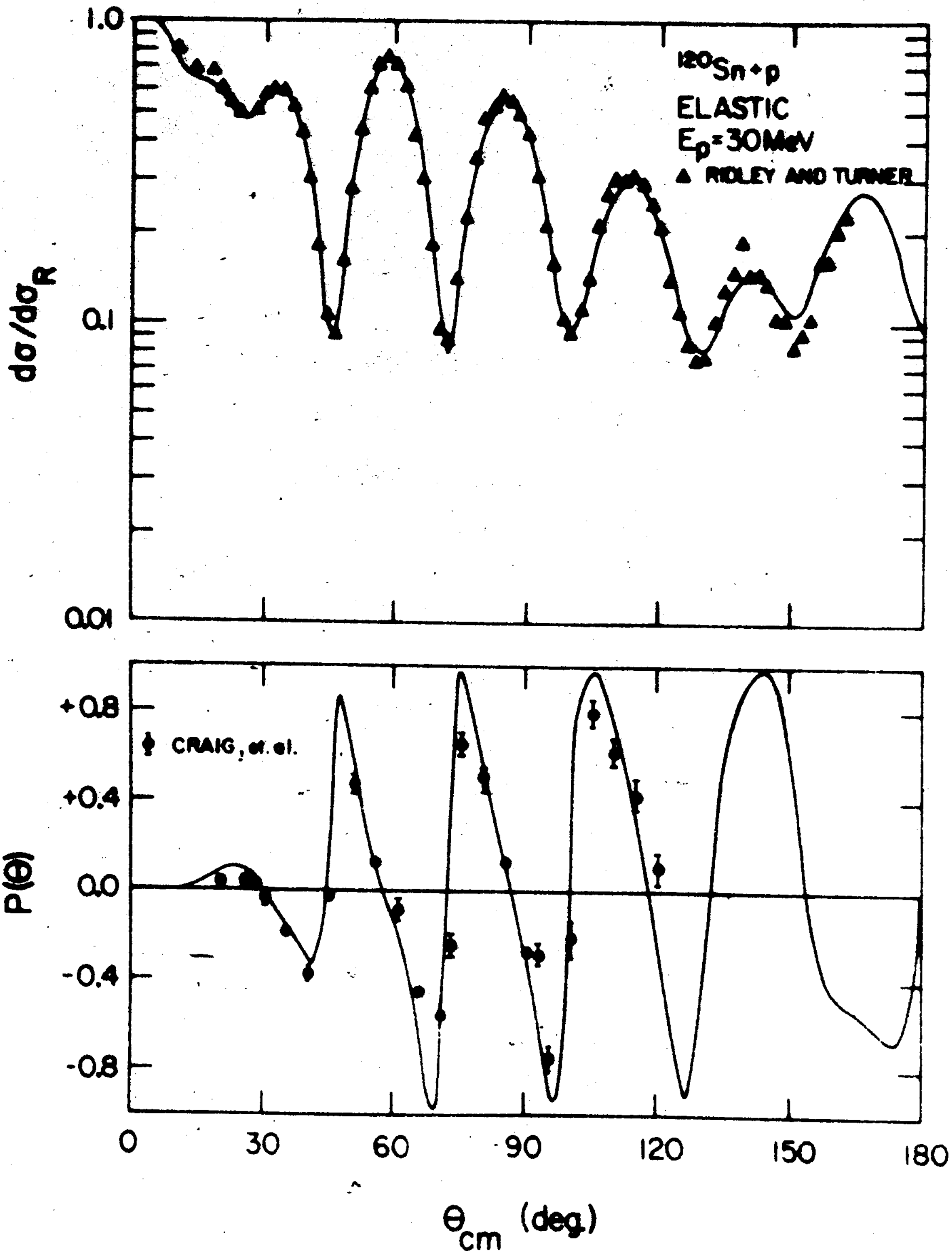

Figure IV-6. ^{120}Sn elastic cross section and polarization fits obtained for the 30 MeV data (Ri 64, Cr 64) with parameter set 2C of Table IV-2. This fit is typical of those obtained for ^{120}Sn.

CHAPTER V

EXPERIMENTAL RESULTS AND COMPARISON TO THEORY

V.A. $^{12}C(p,p')^{12}C^{*}$ (4.44)

V.A.1. Differential Cross Sections

Figure V-1 shows the differential cross sections predicted by the collective model ("COLL"), the impulse approximation ("HJIA"), and the Kallio-Kolltveit interaction ("KK2/3") along with the inelastic scattering data of (Di 63) and (Bl 66a). The optical-model parameters are listed in Table V-1 and V-2. The predictions of the collective model are normalized to the experimental total cross section. The value of the deformation parameter determined from the normalization was $\beta_2 = 0.66$ in agreement with previous results (Sa 67).

The best agreement with the experimental data at both energies was obtained from the collective-model calculations. The agreement was particularly good at 40 MeV, where the shape was quite accurately predicted between 0° and 110°. However, the small backward peak observed at this energy was not reproduced.

The microscopic-model calculations are in generally

Table V-1. Entrance channel optical-model parameters used in the DWBA calculations.[a)]

E_p(MeV)	V(MeV)	r_R(F)	a_R(F)	W_D(MeV)	r_I(F)	a_I(F)	V_{SO}(MeV)[b)]	r_{SO}(F)	a_{SO}(F)
26.2	48.5	1.07	0.636	3.38	1.34	0.648	8.10	1.13	0.555
							7.13	1.04	0.472
							6.30	0.96	0.415
40.0	45.0	1.08	0.685	5.15	1.26	0.570	8.50	1.10	0.550
							7.65	1.04	0.500
							7.00	0.96	0.465

a) These parameters were determined from the energy-dependence studies (see Figure IV-4). Well-depth parameters which do not appear in the table were set equal to zero. The Coulomb radius was taken to be r_c=1.20F.

b) For the spin-orbit parameters, the first (third) number given is the largest (smallest) value the parameter can have such that X_T^2 is increased by less than 25% from its minimum value. The second number given is the 'optimum' value of the parameter.

Table V-2. Exit channel optical-model parameters used in the DWBA calculations.[a]

E_p(MeV)	V(MeV)	r_R(F)	a_R(F)	W_D(MeV)	r_I(F)	a_I(F)	V_{SO}(MeV)[b]	r_{SO}(F)	a_{SO}(F)
26.2	50.0	1.07	0.626	2.77	1.36	0.675	8.00	1.13	0.555
							6.98	1.04	0.464
							6.10	0.96	0.400
40.0	46.0	1.08	0.670	4.65	1.28	0.594	8.30	1.15	0.550
							7.46	1.04	0.490
							6.75	0.96	0.450

[a] These parameters were determined from the energy-dependence studies (see Figure IV-4). Well-depth parameters which do not appear in the table were set equal to zero. The Coulomb radius was taken to be r_c=1.20F.

[b] For the spin-orbit parameters, the first (third) number given is the largest (smallest) value the parameter can have such that X_T^2 is increased by less than 25% from its minimum value. The second number given is the 'optimum' value of the parameter.

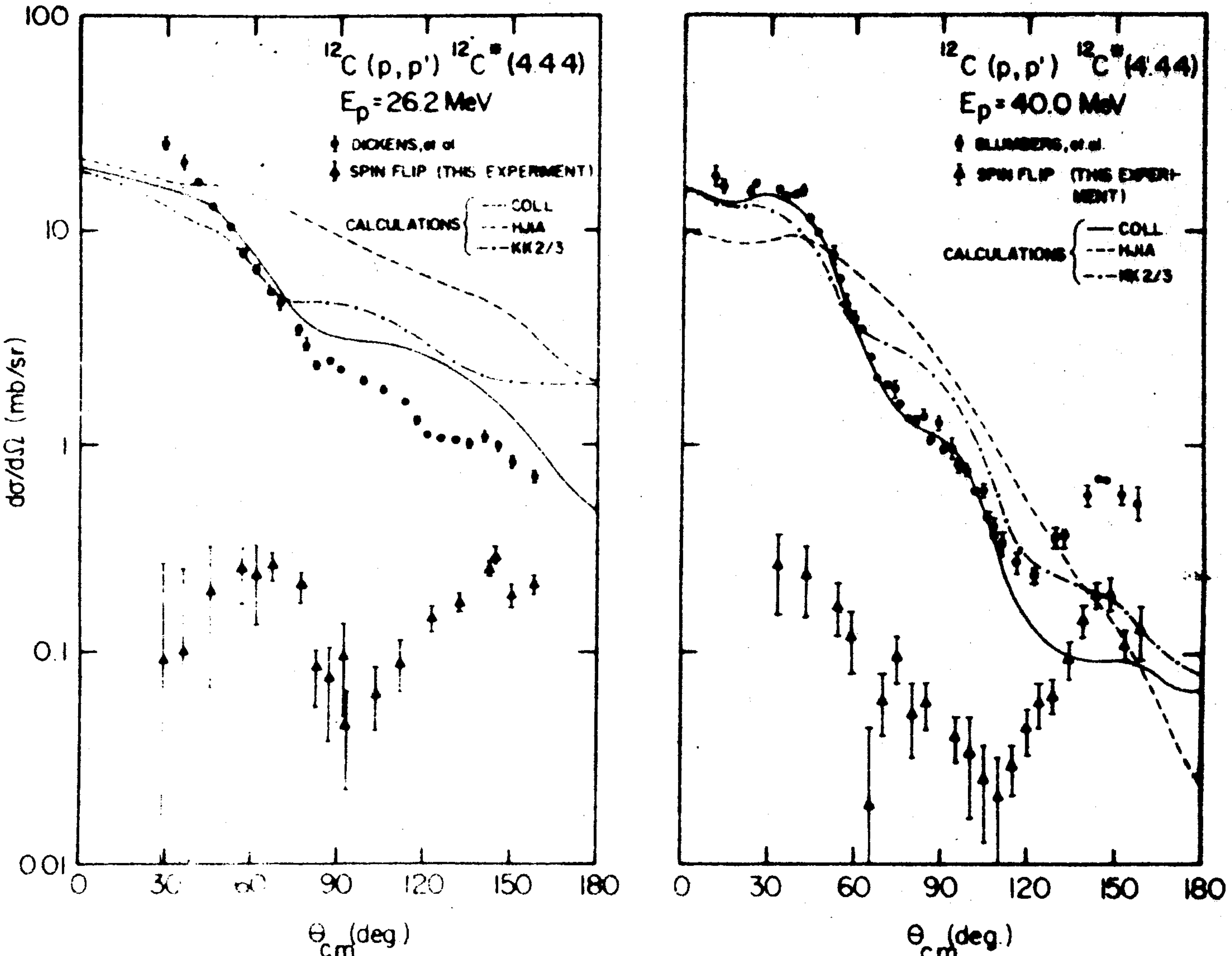

Figure V-1. DWBA fits to the ^{12}C inelastic cross section data at E_p=26.2 MeV (Di 63) and 40.0 MeV (Bl 66a). The optical-model parameters are listed in Tables V-1 and V-2.

poorer agreement with experiment. On the other hand, these models have no free parameters (all parameters are determined from nucleon-nucleon scattering data). In particular, the absolute magnitude of the cross section is predicted by theory so that the curves are not arbitrarily normalized to the total cross section as is the case for the collective model. It is interesting to note that the shapes predicted by the Kallio-Kolltveit interaction are similar to the collective-model predictions at both energies, and that the impulse-approximation prediction agrees somewhat better with the experimental data at the higher energy.

V.A.2. Inelastic Asymmetries

The inelastic asymmetries calculated with the three models are shown in Figures V-2 and V-3, along with the experimental data of (Cr 66) and (Bl 66a). Both microscopic-model calculations include the contributions of the $s=1$ amplitude arising from the spin-dependent part of the interaction potential (see Sec.II.C.2). The collective model in which the spin-orbit part of the optical potential is not deformed does not lead to such an amplitude.

The agreement obtained with the experimental inelastic asymmetry data was at best only qualitative even in the collective model. The phase predictions in this model are reasonably good at both energies, but the calculated magnitudes are far too small. The impulse-approximation predictions are again quite different from those of the

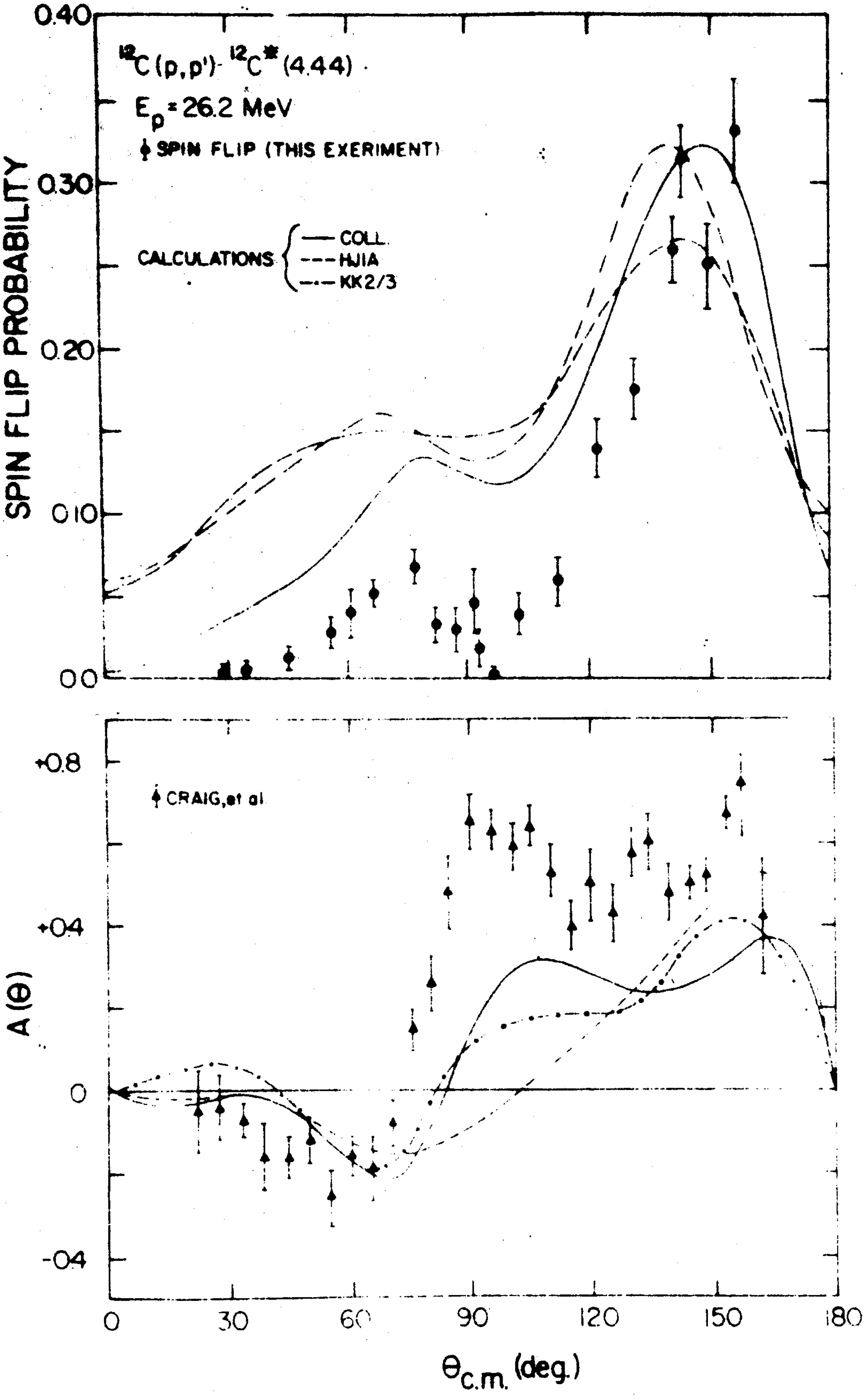

Figure V-2. DWBA fits to the ^{12}C spin flip, and to the inelastic asymmetry data (Cr 66), at E_p=26.2 MeV.

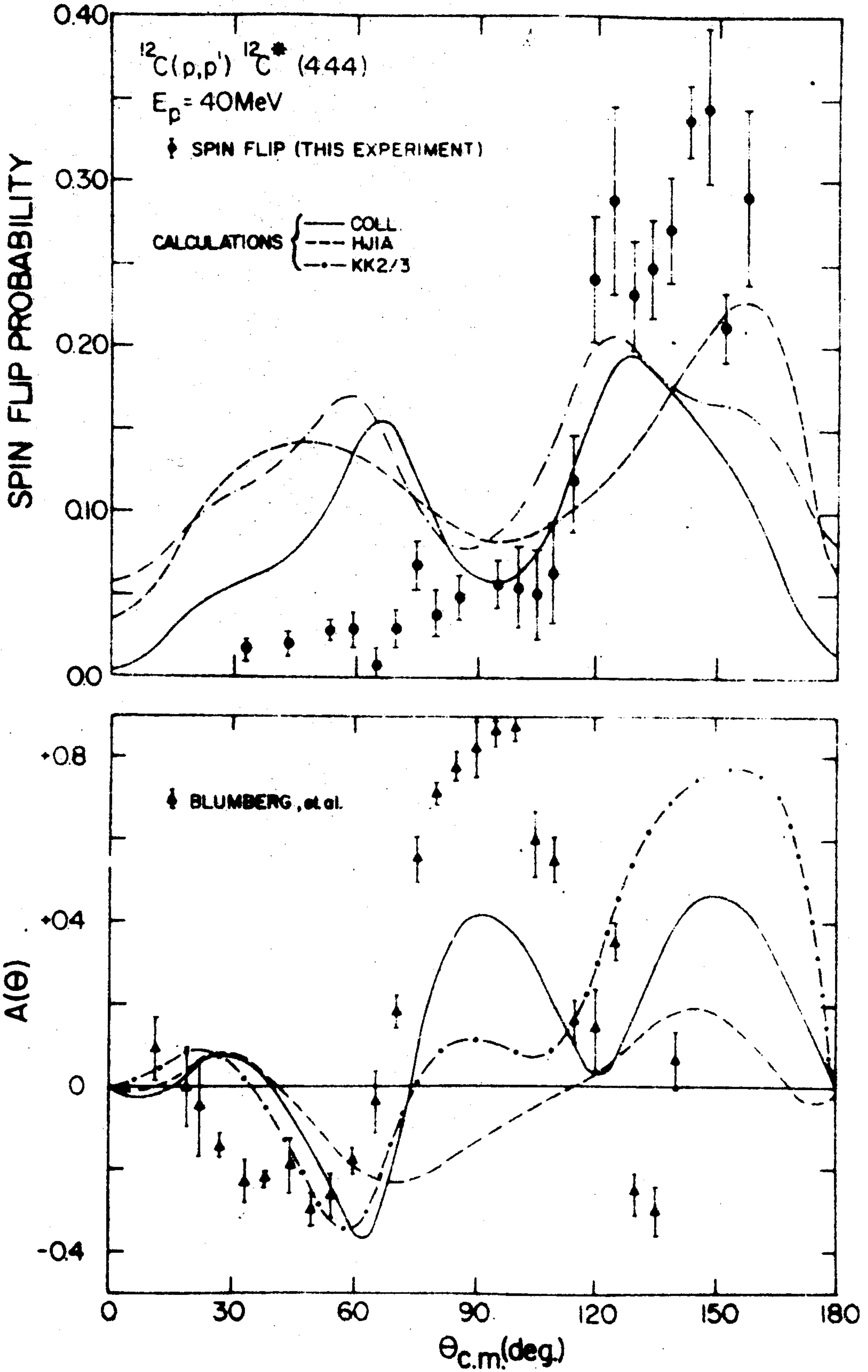

Figure V-3. DWBA fits to the ^{12}C spin flip, and to the inelastic asymmetry data (Bl 66a), at E_p=40.0 MeV.

collective model and are also in poor agreement with experiment. The quality of the predictions obtained in this model deteriorated at the higher energy where the cross section predictions, Figure V-1, improved. Finally, it should be noted that the predictions of the Kallio-Kollveit interaction again resemble those of the collective model.

V.A.3. Spin-Flip Probability

The spin-flip probabilities determined in this experiment are also shown in Figures V-2 and V-3. The average run time per datum point was approximately 30 minutes. As mentioned previously (Sec.III.D.2) there is an uncertainty in the absolute normalization of ±9% at 26 MeV and ±14% at 40 MeV. The data exhibit the characteristic backward peak of approximately 30% at 140° which has been observed at lower energies (Sc 64) and for other nuclei (Gi 68,Ee 68). The experimental total spin-flip probability, which is defined by:

$$P_T^{SF} = \frac{\int P(\theta)\,\frac{d\sigma}{d\Omega}(\theta)\,d\Omega}{\int \frac{d\sigma}{d\Omega}(\theta)\,d\Omega} \qquad \text{(V.1)}$$

where $\frac{d\sigma}{d\Omega}(\theta)$ is the differential cross section and $P(\theta)$ is the spin-flip probability at center-of-momentum angle θ, is given in Table V-3. Note that spin-flip events constitute only a very small fraction (~3%) of the total inelastic cross section.

The spin-flip predictions of the three models

Table V-3. Total spin-flip probability.

Experiment	E_p(MeV)	Measured Value	Theory(COLL)	Theory(HJIA)	Theory(KK)
^{12}C	26.2	0.0275 ± 0.0055	0.0875	0.1480	0.1420
^{12}C	40.0	0.0325 ± 0.0075	0.0720	0.1190	0.1190
^{120}Sn	30.0	0.077 ± 0.040	0.016	0.022	0.023

(Figures V-2 and V-3) are in semi-quantitative agreement with the experimental data. The largest discrepancies occur at the forward angles where the spin-flip probability is consistently over-estimated. The predicted total spin-flip probability is approximately four times the measured value (see Table V-3).

It is interesting that the collective model, which contains no s=1 amplitude, predicts a spin-flip probability in reasonable agreement with the experimental data. We conclude that the observed spin flip is almost entirely due to the distortions introduced into the entrance and exit elastic-channel wave functions by the spin-orbit term in the optical potential. This implies that if any meaningful information regarding the s=1 part of the inelastic interaction is to be obtained from spin-flip data, the experiment must be performed for nuclei having very well determined optical-model parameters so that the effects of the spin-orbit distortion can be separated from those of the s=1 amplitude of the inelastic interaction.

A series of calculations has been performed in which the parameters of the spin-orbit term in the optical potential were systematically varied in an attempt to determine the sensitivity of the spin-flip predictions to these parameters. First, we determined the range over which the parameters could be varied such that X_T^2 for the fits to the elastic data increased by less than 25% (see Sec.IV.C). The limits of this range appear in Tables V-1 and V-2 for each of the parameters. Distorted-wave calculations were then made using the upper or lower limits for one of the parameters while fixing the remaining parameters at their optimum values. In each case, the form factors given by the impulse approximation were used. The results of these calculations at 26.2 MeV appear in Figures V-4 and V-5. It appears that the spin-flip predictions are somewhat more sensitive than the inelastic asymmetries to the spin-orbit parameters. In fact, it should be possible to determine the spin-orbit term in the optical potential from spin-flip data in those cases for which a polarized beam is unavailable (Pa 68). A major difficulty is that it is not practical to program an automatic search routine for DWBA calculations.

In the same spirit, a number of calculations were performed in an attempt to determine the effect of the s=1 amplitude on the predictions of the microscopic model, again using impulse-approximation form factors. Two types of calculations were performed. In the first case, the optimum optical-model parameters of Tables V-1 and V-2 were used, but the s=1 amplitude was set equal to zero. In the second type of calculation the s=1 amplitude was that predicted by the impulse approximation and the spin-orbit depth V_{so} was set equal to zero. The results of these calculations at 26.2 MeV also appear in Figure V-5. It is clear that the s=1 amplitude has only a small effect on the spin-flip and asymmetry predictions. The predicted spin flip is increased by an amount which is almost independent of angle so that

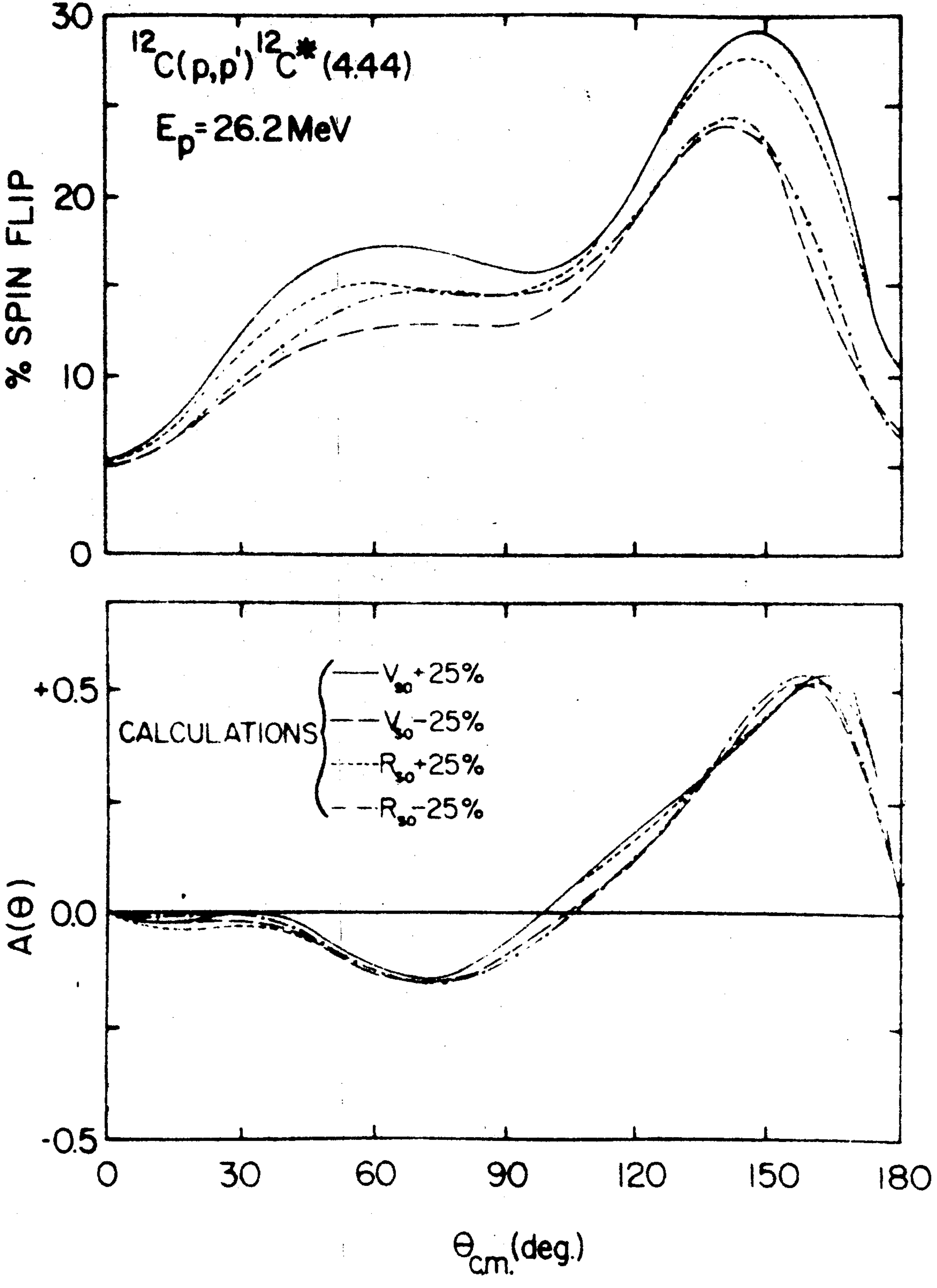

Figure V-4. Dependence of the spin-flip and inelastic asymmetry predictions on the spin-orbit optical parameters. The notation ('$\pm$25%') refers to the upper and lower limits for the parameters listed in Tables V-1 and V-2.

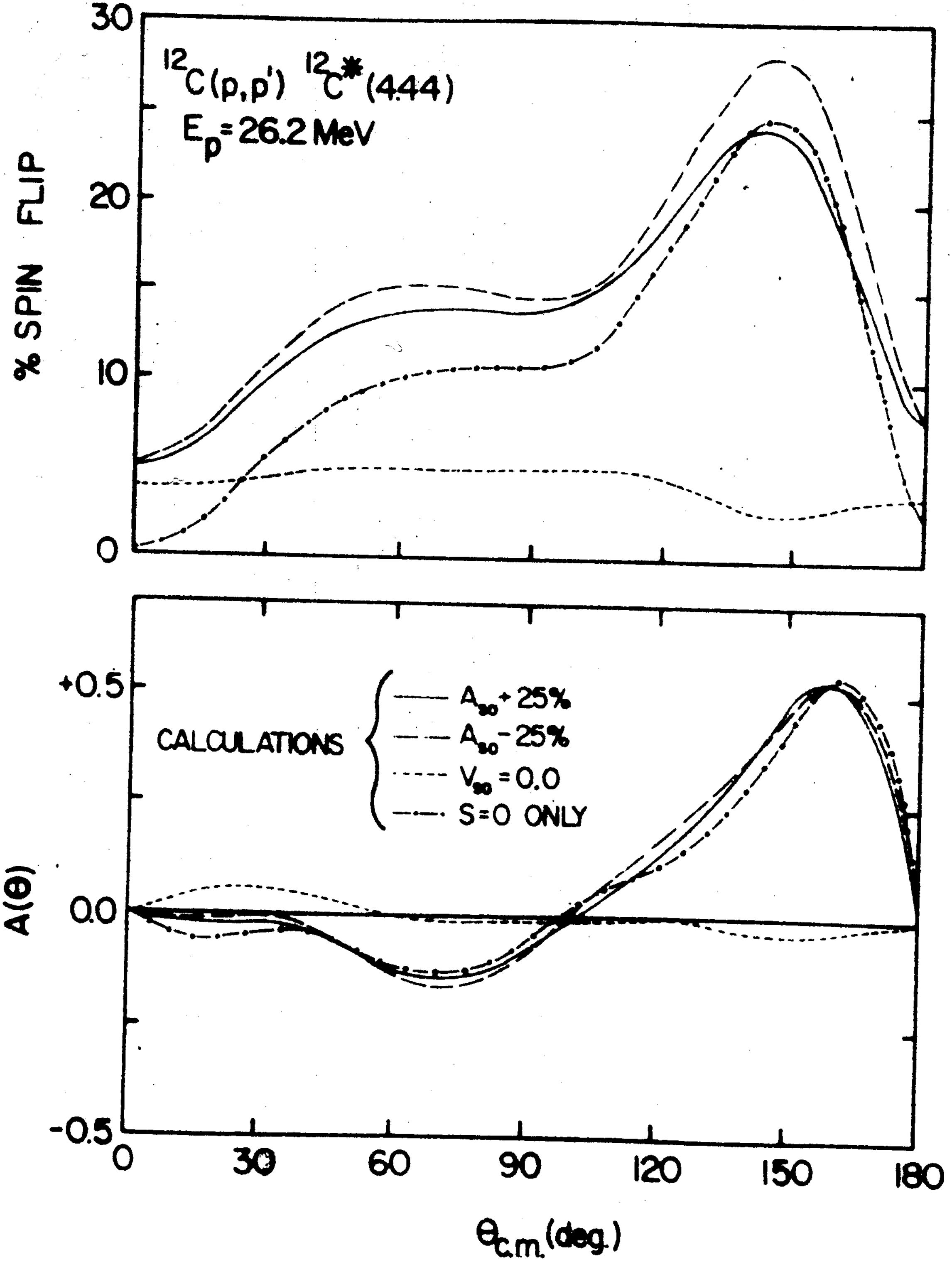

Figure V-5. Dependence of the spin-flip and inelastic asymmetry predictions on the spin-orbit optical parameters, and on the s=1 part of the

the greatest differences occur at the forward angles, where the spin flip is smallest.

No definite conclusions regarding the spin-dependent part of the inelastic interaction can be obtained from these results. The addition of an s=1 amplitude to the microscopic-model form factors seemed to make the agreement with the experimental data worse, in that it increased the predicted spin flip at the forward angles where it was already too large. However, in view of the inability of any of the models to reproduce the inelastic asymmetries, and considering the fact that optical-model parameters which adequately fit all of the elastic data could not be found, it would seem that the difficulty lies in the failure of the optical model for nuclei as light as ^{12}C.

V.B. $^{120}Sn(p,p')^{120}Sn^*$ (1.17)

V.B.1. Differential Cross Sections

The differential cross section predictions of the three models for 30 MeV inelastic proton scattering from the first 2^+ state of ^{120}Sn appear in Figures V-6 to V-8, along with the experimental data of (Ri 64a). Calculations were performed for all of the sets of optical-model parameters listed in Table IV-2, but the resulting predictions were very similar so that only two of them are shown for each model.

The collective-model predictions (Figure V-6) are in

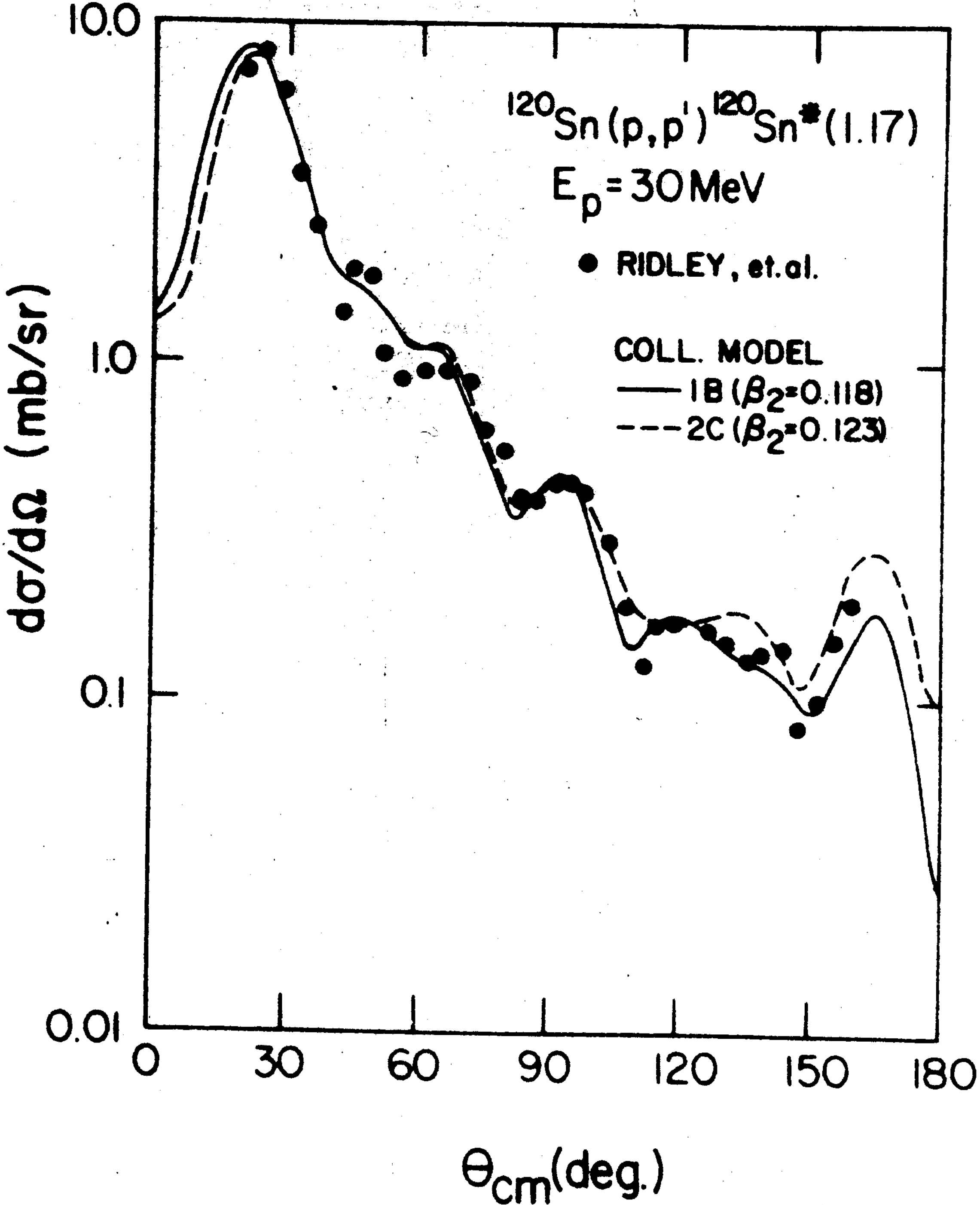

Figure V-6. Collective-model DWBA fits to the ^{120}Sn inelastic cross section data (Ri 64a) at 30 MeV. The identification numbers 1B and 2C refer to the optical-model parameter sets of Table IV-2. The deformation parameter is also given.

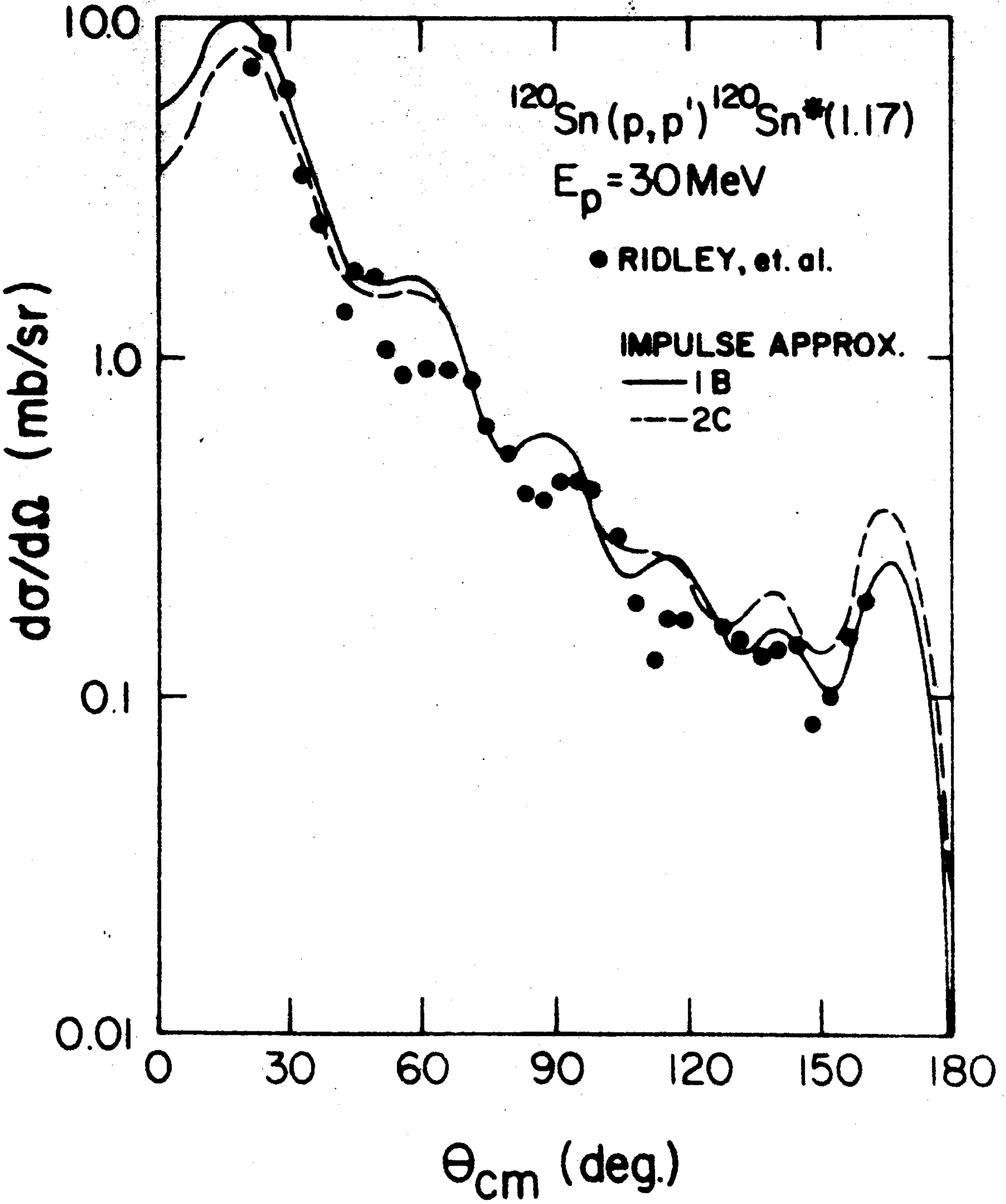

Figure V-7. Microscopic-model DWBA fits to the ^{120}Sn inelastic cross section data, using impulse-approximation form factors.

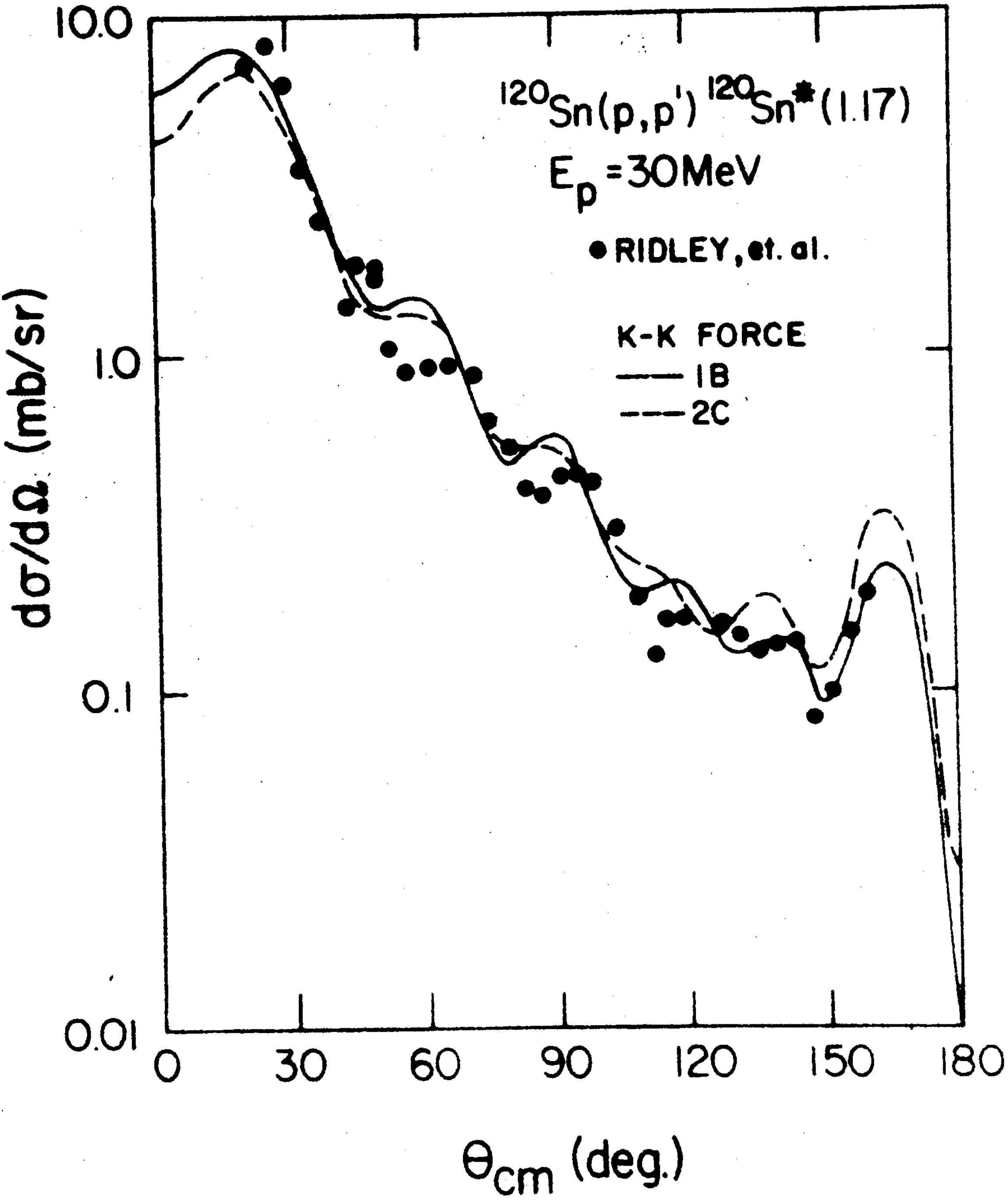

Figure V-8. Microscopic-model DWBA fits to the ^{120}Sn inelastic cross section data, using Kallio-Kolltveit form factors.

very good agreement with the experimental cross section data. The values obtained for the deformation parameter β_2 (Figure V-6) compare favorably with previous results (Ri 64a,Fu 68). Furthermore, the calculated value for the reduced transition strength B(E2) is in good agreement with gamma-ray measurements (St 58), and with theoretical predictions (Ra 67) as indicated in Table V-4. The microscopic-model predictions (Figures V-7 and V-8) are also in good agreement with the experimental data. As mentioned previously (Sec.II.C.3), these calculations were performed using the Yoshida wave functions (Yo 62) which include the effects of quasi-particle excitations from the closed neutron and proton cores as well as in the unfilled neutron shells (the 'nuclear cloud'). The results indicate that these wave functions give an adequate description of the ^{120}Sn nucleus.

V.B.2. Spin Flip

The predicted spin-flip probabilities appear in Figures V-9 to V-11, along with the data from this experiment. Each datum point represents an average run time of about two hours. The absolute normalization is uncertain by ±5% due to the uncertainty in the efficiency of the gamma-ray detector (Sec.III.D.2). The experimental and theoretical total spin-flip probabilities appear in Table V-1. In contrast to the case for ^{12}C, the theory here under-predicts the total spin flip by about a factor of three.

The theoretical predictions of all the models are very

Table V-4. Comparison of the B(E2) values obtained from proton inelastic scattering to the results of gamma-ray measurements and to the theoretical predictions.

$B(E2)^{a)}_{exp}$	$B(E2)^{b)}_{exp}$	$B(E2)^{c)}_{th}$
$(2.50 \pm 0.25) \times 10^3 e^2 F^4$	$(2.20 \pm 0.11) \times 10^3 e^2 F^4$	$1.865 \times 10^3 e^2 F^4$

[a)] Inelastic proton scattering.

[b)] Gamma-ray measurement (St 58).

[c)] Theoretical prediction (Ra 67).

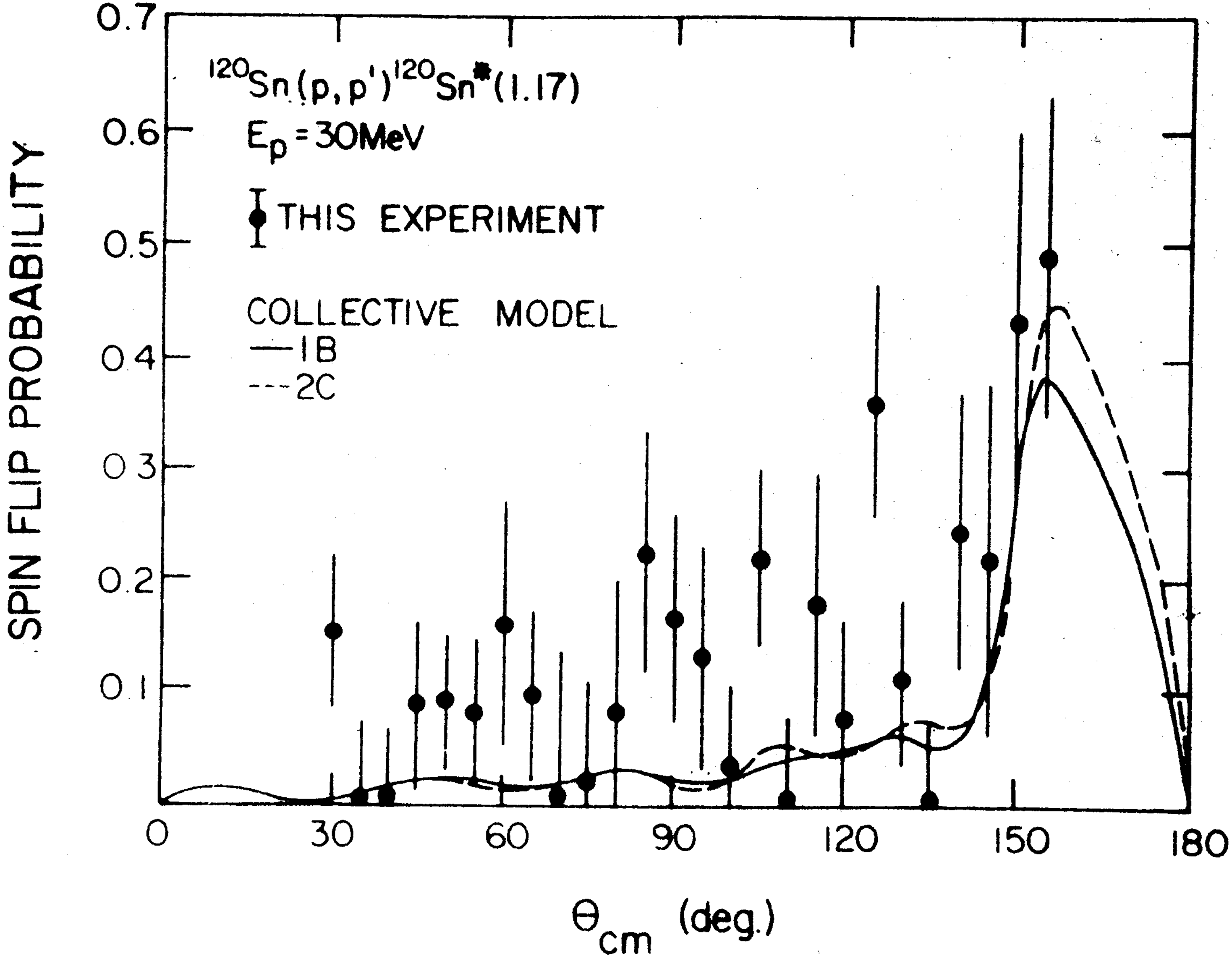

Figure V-9. Collective-model DWBA fits to the ^{120}Sn spin-flip data.

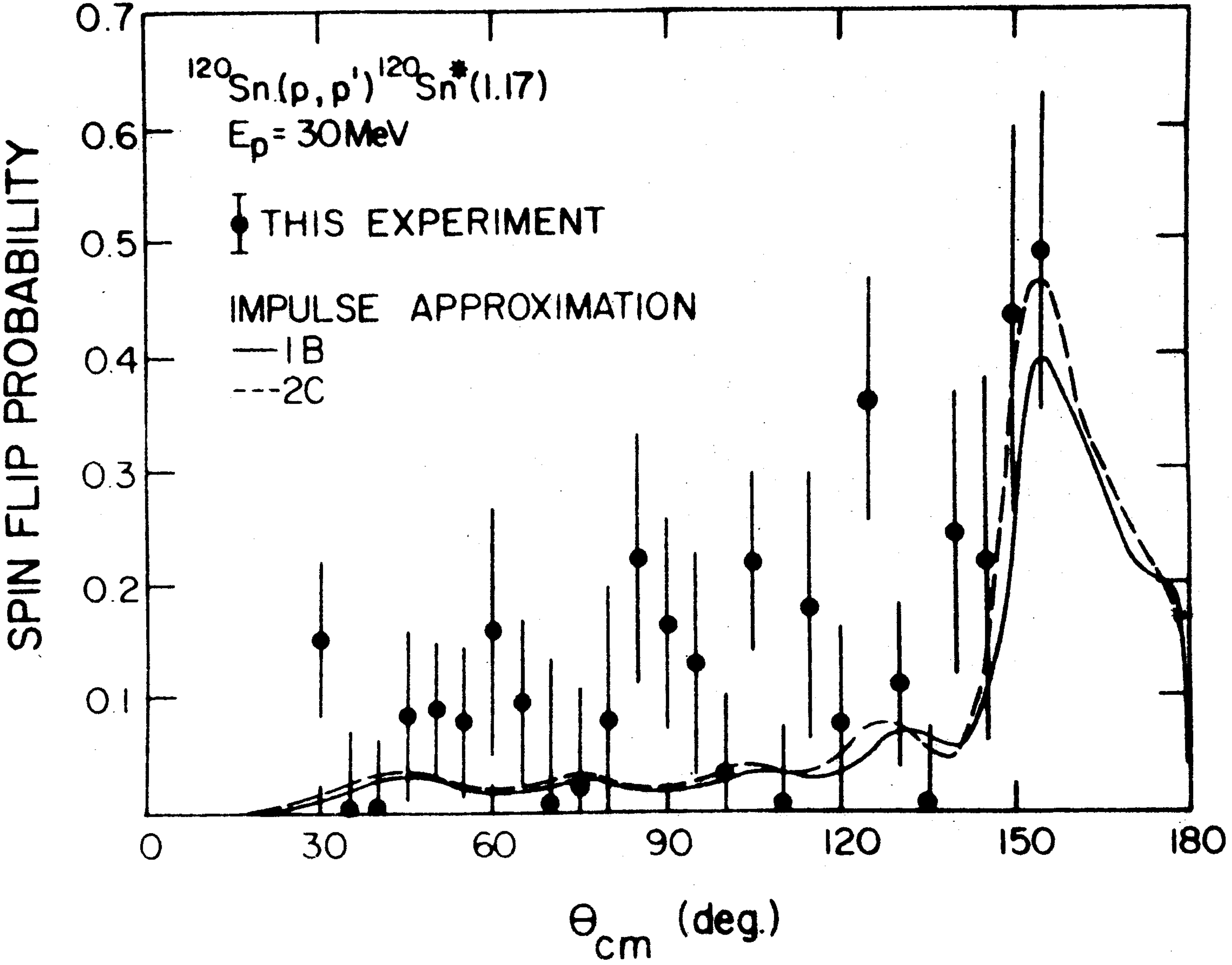

Figure V-10. Microscopic-model DWBA fits to the ^{120}Sn spin-flip data, using impulse-approximation form factors.

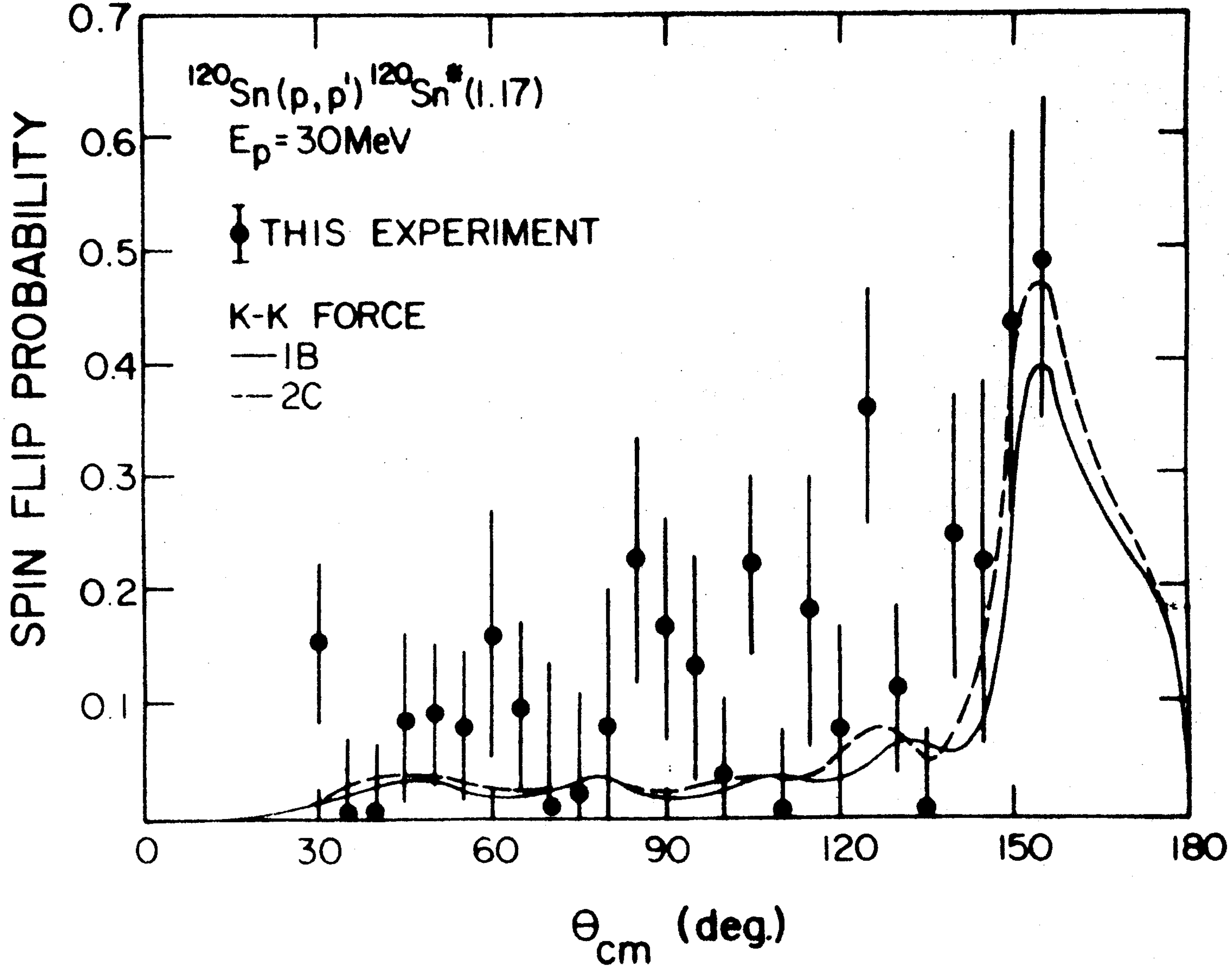

Figure V-11. Microscopic-model DWBA fits to the ^{120}Sn spin-flip data, using Kallio-Kolltveit form factors.

similar. The backward peak, which has previously been associated with the effects of distortions introduced into the elastic-channel wave functions by the spin-orbit term in the optical potential (Sec.V.A.3), is well reproduced in all cases. It is particularly interesting to note that the initial rapid rise in the spin-flip probability, which occurs at a center-of-momentum scattering angle of about 120° for the ^{12}C data at both 26.2 and 40.0 MeV and at about 130° for ^{58}Ni spin-flip data at 15 and 20 MeV (Ee 68,Ko 67a), occurs here at approximately 140°. This may indicate a systematic behavior in this feature of the distribution as a function of the mass number of the target. The location of this 'edge' is accurately predicted by the DWBA calculations.

The situation is quite different for angles away from the peak of the distribution. The spin-flip predictions of all the models are significantly smaller than the experimental data in this case. In particular, the average value for all the experimental points between 30° and 135° is 0.103 ± 0.020. The average predicted spin-flip probability over this angular range is about 0.025. Even if it is assumed that the acceptance-angle correction (Sec.III.D.3) takes on its maximum possible value at all angles, the experimental average is only reduced to 0.094 ± 0.020. Therefore, the discrepancy cannot be accounted for by the uncertainty in this correction. In addition, a comparison of the collective-model and microscopic-model predictions shows that the addition of an s=1 amplitude due to the spin-spin term in the two-body scattering (Sec.II.C.2) does not improve the agreement between theory and experiment. It happens that the various single-particle contributions to the form factor (Sec.II.C.3) add in phase for the s=0 part of the interaction but cancel almost completely for the s=1 part. As a result the s=1 amplitude makes little or no contribution to the predicted spin flip. Calculations were performed using the complete impulse-approximation form factor (s=0 and s=1) with the spin-orbit well depth in the optical-model potential set equal to zero. The predicted spin flip was essentially zero as expected from the comparison to the predictions of the collective model, which does not contain an s=1 amplitude.

It is possible that the forward-angle discrepancy may be removed by calculations which include some terms in the two-body scattering amplitude that have been neglected in this discussion. In particular, the two-body tensor and spin-orbit forces may make significant contributions to the predicted spin flip. The single-particle contributions from the latter, at least, are expected to add in phase (Mc 69a). It is particularly encouraging in this respect that collective-model calculations in which the spin-orbit term in the optical potential is deformed tend to predict larger spin-flip probabilities at the forward angles. (Sh 68,Gi 68). A microscopic-model calculation which includes the two-body tensor and spin-orbit forces should display the same behavior (Mc 69a).

CHAPTER VI

SUMMARY AND CONCLUSIONS

The spin-flip probability for protons inelastically scattered from the first 2^+ state in ^{12}C and ^{120}Sn has been measured at incident proton energies of 26.2 and 40.0 MeV for ^{12}C, and 30.0 MeV for ^{120}Sn. The data display the characteristic backward peak which has been observed at lower energies (Sc 64, Ko 67a) and for other nuclei (Ko 67a, Ee 68, Gi 68). The magnitude of this peak is about 0.30 for ^{12}C and 0.50 for ^{120}Sn, and the location of its rapidly rising edge seems to be correlated with the target mass number. The total spin-flip probability is approximately 0.03 for ^{12}C and 0.08 for ^{120}Sn.

The theoretical analyses of the data in the framework of the DWBA are in semi-quantitative agreement with experiment at the peak of the distribution. The most serious failure in this regard occurs for the ^{12}C data at 40.0 MeV, when the predicted peak spin flip is only about 0.20 compared to the measured value of 0.30. However, larger differences are observed for the forward angle data. In the case of ^{12}C spin flip, these discrepancies are of such a nature that no definite conclusions may be reached regarding the spin-dependent part of the inelastic interaction. The addition of an s=1 amplitude in this case made the agreement between experiment and theory somewhat worse, in that it significantly increased the predicted spin flip at the forward angles where it was already too large. However, these discrepancies are in large part bound up with the general failure of the optical model to give an adequate representation of a nucleus as light as ^{12}C. The situation is somewhat different with respect to the ^{120}Sn forward angle data. In this case, the spin flip is under-predicted by about a factor of three. The remarkably good fits obtained from the optical model for the elastic cross section and polarization, and the fact that the inelastic cross section and the backward peak in the spin-flip distribution are very well reproduced in the DWBA calculations, lead one to believe that the calculated contribution to the spin-flip probability from the elastic-channel wave functions is essentially correct. In addition, there is some evidence that a more adequate treatment of the spin-dependence of the inelastic interaction will lead to an increase in the predicted spin flip at the forward angles (Gi 68,Ko 67a). This suggests that further DWBA calculations should be performed including those spin-dependent parts of the two-body scattering amplitude which have been neglected here.

The present experiment was directed toward the determination of the type of information about spin-dependent nucleon-nucleus forces which can be obtained from spin-flip data. Two general conclusions can be reached in this regard from the previous discussion. First of all, the prominent backward peak which is characteristic of all the data presented has been associated with the distortions introduced into the elastic-channel wave functions by the spin-orbit term in the optical model potential. Therefore, this feature of the distribution may be used to determine the spin-orbit parameters when elastic polarization data are unavailable (Pa 68), and it can provide supplementary information in those cases for which the scattering of polarized protons has been measured. Secondly, it seems from the ^{120}Sn data that meaningful information concerning the spin dependence of the inelastic part of the interaction can be obtained by careful measurements in the forward direction for those cases in which the optical model parameters are reasonably well determined.

Two general types of spin-flip experiments are suggested by the results of the present study. First, ^{3}He inelastic scattering and spin flip could be investigated, leading to a determination of the spin-orbit parameters of the optical model (Pa 68). Secondly, it would be of great interest to have accurate forward angle data for a set of nuclei having essentially the same optical-model parameters and different detailed structure (such as the even-even isotopes of Sn, Cd, and Te) to investigate the dependence of the spin-flip probability on the nuclear wave functions and the two-body scattering parameters. This latter investigation should yield information on the spin dependence of the inelastic interaction which is difficult to obtain in any other way.

APPENDIX A

THE BOHR THEOREM

We wish to investigate the effect of a reflection in the scattering plane on a two-body scattering system which conserves total angular momentum and parity. Such a reflection may be obtained by a rotation of 180° about the normal to the scattering plane, followed by a parity inversion (Figure A-1). Denote the reflection operator by $\mathcal{R}$, the rotation operator by R, and the parity operator by P. Then:

$$\mathcal{R} = P R_z(\pi) \tag{A.1}$$

For a system with total angular momentum $\vec{J}$:

$$R_z(\pi) = e^{i(\vec{J}\cdot\hat{z})\pi} = e^{iM_J\pi} \tag{A.2}$$

where M_J is the z-component of the total angular momentum. The reflection operator becomes:

$$\mathcal{R} = P e^{iM_J\pi} \tag{A.3}$$

It is clear that the eigenvalue of this operator will be a constant of the motion for any system which conserves

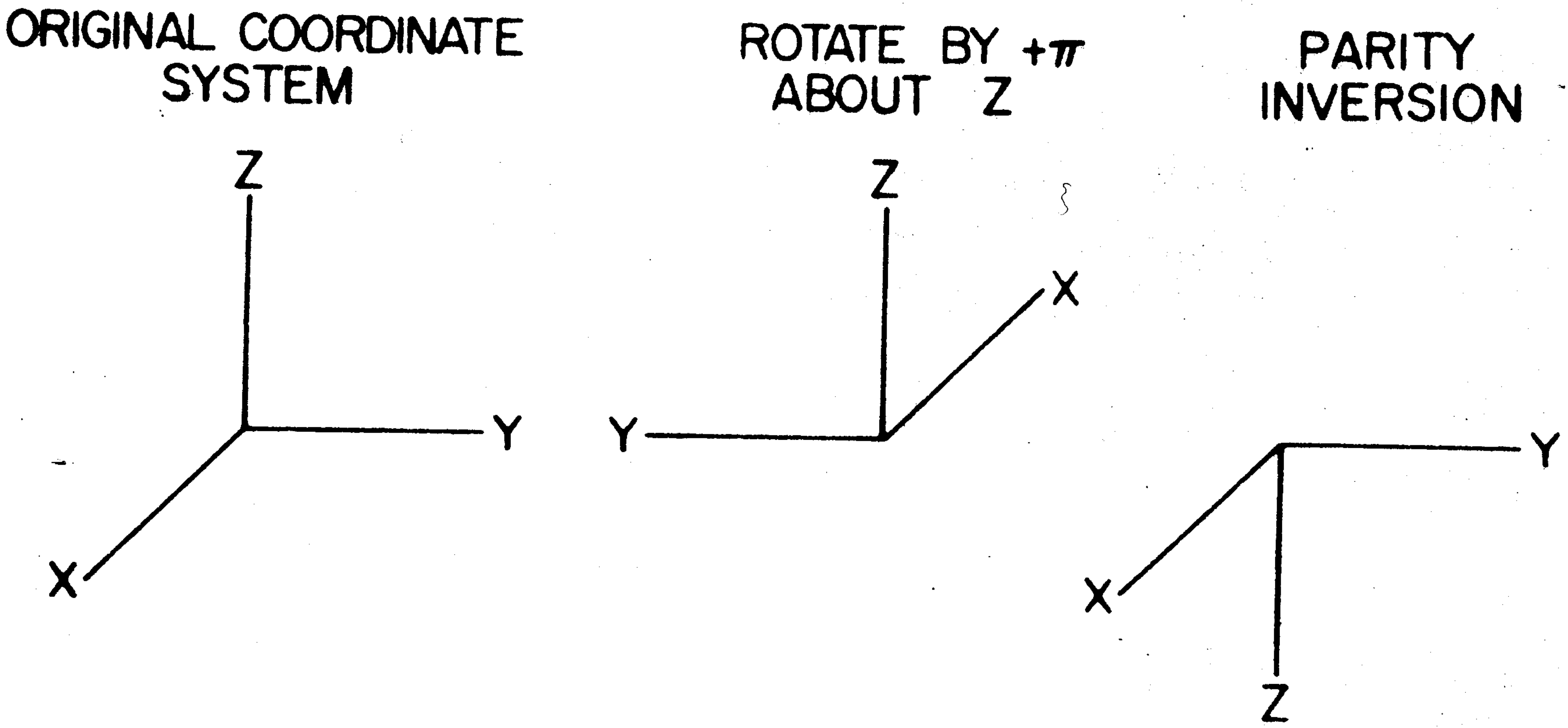

Figure A-1. Composition of a reflection in the scattering plane (x-y plane) by a rotation of 180° about the z-axis followed by a parity inversion.

total angular momentum and parity. In particular, if ψ_i and ψ_f refer to the (normalized) initial and final eigenstates of a two-body scattering system:

$$\langle \psi_i | \mathcal{R} | \psi_i \rangle = \langle \psi_f | \mathcal{R} | \psi_f \rangle \tag{A.4}$$

Now, the total angular momentum $\vec{J}$ is composed of an orbital and a spin part:

$$\vec{J} = \vec{L} + \vec{S} \tag{A.5}$$

Similarly, the parity operator can be divided into an orbital and a nuclear parity:

$$P = P_l P_n \tag{A.6}$$

so that the expression for the reflection operator becomes:

$$\mathcal{R} = P_l P_n e^{i(l_z + s_z)\pi} \tag{A.7}$$

where l_z (s_z) is the z-component of orbital (spin) angular momentum.

Next expand the state ψ_i in the spherical harmonics:

$$|\psi_i\rangle = \sum_{l m_l \alpha} C_{l m_l \alpha}(q_\alpha)\, Y_l^{m_l}(\theta,\phi) \tag{A.8}$$

where the functions $C_{l m_l \alpha}(q_\alpha)$ contain all the other coordinates describing the system, such as the spin eigenfunctions and the radial dependence. Because of the initial choice of axes, the coordinate Θ is always equal to 90°. We have:

$$\mathcal{R}|\psi_i\rangle = P_n\, e^{i\pi s_z} \sum_{l m_l \alpha} C_{l m_l \alpha}(q_\alpha)\, P_l\, e^{i\pi l_z}\, Y_l^{m_l}(\tfrac{\pi}{2},\phi)$$

$$= P_n\, e^{i\pi s_z} \sum_{l m_l \alpha} (-)^{l+m_l} C_{l m_l \alpha}(q_\alpha)\, Y_l^{m_l}(\tfrac{\pi}{2},\phi) \qquad \text{(A.9)}$$

Now, the spherical harmonic $Y_l^{m_l}(\pi/2,\phi)$ vanishes unless $l + m_l$ is an even integer. Therefore:

$$\mathcal{R}|\psi_i\rangle = P_n\, e^{i\pi s_z}|\psi_i\rangle \qquad \text{(A.10)}$$

A similar expansion can be made for the final state ψ_f. The detected particle is again in the scattering plane (by definition) so that the results are the same. Substituting into (A.4):

$$\langle\psi_i|P_n\, e^{i\pi s_z}|\psi_i\rangle = \langle\psi_f|P_n\, e^{i\pi s_z}|\psi_f\rangle \qquad \text{(A.11)}$$

We have recovered the Bohr theorem, which simply states that the eigenvalue of the operator:

$$\mathcal{R}' = P_n\, e^{i\pi s_z} \qquad \text{(A.12)}$$

is a constant of the motion for a two-body scattering system which conserves parity and total angular momentum.

APPENDIX B

ACCEPTANCE-ANGLE CORRECTION

The general angular correlation function W(φ_p , θ_γ , ϕ_γ) for the de-excitation of the 2^+ nuclear state to its 0^+ ground state is (Sc 64):

$$W(\varphi_p, \theta_\gamma, \varphi_\gamma) = \sum_{\nu m m'} P_\nu \, a_m(\nu) \, a^*_{m'}(\nu) \, \widetilde{\chi}_{2m} \cdot \widetilde{\chi}^*_{2m'} \qquad (B.1)$$

where $\widetilde{X}_{2m}$ is a normalized vector spherical harmonic (Bl 52) of order two, ν represents the possible combination of spin orientations of the projectile in its initial and final state, P_ν is the probability that a particular combination will occur, and $a_m(\nu)$ is the amplitude for exciting the m^{th} magnetic sublevel with that combination. For proton scattering there are four such combinations:

ν =1: incident spin up, outgoing spin down
ν =2: incident spin up, outgoing spin up (B.2)
ν =3: incident spin down, outgoing spin up
ν =4: incident spin down, outgoing spin down

If the quantization axis is chosen along the normal to the scattering plane, the Bohr theorem (Appendix A) requires that:

$$a_m(v) = 0 \quad \text{if} \quad m+v \text{ is odd.} \tag{B.3}$$

Applying this restriction and evaluating the spherical harmonics:

$$W = \frac{5}{16\pi}\Big[(4\cos^4\theta_\gamma - 3\cos^2\theta_\gamma + 1)\Big(P_1\{|a_1(1)|^2 + |a_{-1}(1)|^2\} + P_3\{|a_1(3)|^2 + |a_{-1}(3)|^2\}\Big)\Big]$$

$$+ \frac{15}{8\pi}\Big[\sin^2\theta_\gamma\cos^2\theta_\gamma\,(P_2|a_0(2)|^2 + P_4|a_0(4)|^2)\Big]$$

$$+ \frac{5}{16\pi}\Big[(1-\cos^4\theta_\gamma)\Big(P_2\{|a_2(2)|^2 + |a_{-2}(2)|^2\} + P_4\{|a_2(4)|^2 + |a_{-2}(4)|^2\}\Big)\Big]$$

$$+ \frac{5}{16\pi}\Big[2\sin^2\theta_\gamma(4\cos^2\theta_\gamma - 1)\Big(P_1\,\mathcal{R}e\{a_1(1)\,a^*_{-1}(1)\,e^{2i\phi_\gamma}\}$$

$$+ P_3\,\mathcal{R}e\{a_1(3)\,a^*_{-1}(3)\,e^{2i\phi_\gamma}\}\Big)\Big]$$

(B.4)

$$-\frac{5}{8\pi}\sqrt{\tfrac{3}{2}}\Big[2\sin^2\theta_\gamma\cos^2\theta_\gamma\,\Big(P_2\,\mathcal{R}e\{a_2(2)\,a^*_0(2)\,e^{2i\phi_\gamma}\}$$

$$+ P_2\,\mathcal{R}e\{a_0(2)\,a^*_{-2}(2)\,e^{2i\phi_\gamma}\}$$

$$+ P_4\,\mathcal{R}e\{a_2(4)\,a^*_0(4)\,e^{2i\phi_\gamma}\}$$

$$+ P_4\,\mathcal{R}e\{a_0(4)\,a^*_{-2}(4)\,e^{2i\phi_\gamma}\}\Big)\Big]$$

$$-\frac{5}{16\pi}\Big[2\sin^4\theta_\gamma\,\Big(P_2\,\mathcal{R}e\{a_2(2)\,a^*_{-2}(2)\,e^{4i\phi_\gamma}\}$$

$$+ P_4\,\mathcal{R}e\{a_2(4)\,a^*_{-2}(4)\,e^{4i\phi_\gamma}\}\Big)\Big]$$

Now, let:

$$S_0 = P_2\,|a_0(2)|^2 + P_4\,|a_0(4)|^2$$

$$S_1 = P_1\left\{|a_1(1)|^2 + |a_{-1}(1)|^2\right\} + P_3\left\{|a_1(3)|^2 + |a_{-1}(3)|^2\right.$$

$$S_2 = P_2\left\{|a_2(2)|^2 + |a_{-2}(2)|^2\right\} + P_4\left\{|a_2(4)|^2 + |a_{-2}(4)|^2\right\} \qquad (B.5)$$

$$a_m(\nu) = \alpha_m(\nu)\,e^{i\beta_m(\nu)}$$

The quantity S_1 is the probability that the $m=\pm 1$ magnetic substates of the 2^+ level will be excited, i.e., the spin-flip probability. The next step is to evaluate (B.4) for S_1 in terms of the measured angular correlation function W. For a detector at a small angle $\theta_\gamma = \epsilon$, (B.4) leads to:

$$\begin{aligned} S_1 = {} & \frac{8\pi}{5}\,W(\varphi_p, 0^\circ, 0^\circ) - \epsilon^2\left(3S_0 + S_2 - \frac{5}{2}S_1\right) \\ & - 3\epsilon^2\left[T_{1-1}(1)\cos\left(2\varphi_\gamma + \beta_{1-1}(1)\right) + T_{1-1}(3)\cos\left(2\varphi_\gamma + \beta_{1-1}(3)\right)\right] \\ & + \sqrt{6}\,\epsilon^2\left[T_{20}(2)\cos\left(2\varphi_\gamma + \beta_{20}(2)\right) + T_{0-2}(2)\cos\left(2\varphi_\gamma + \beta_{0-2}(2)\right)\right. \\ & \left. + T_{20}(4)\cos\left(2\varphi_\gamma + \beta_{20}(4)\right) + T_{0-2}(4)\cos\left(2\varphi_\gamma + \beta_{0-2}(4)\right)\right] \\ & + \mathcal{O}(\epsilon^4) \end{aligned} \qquad (B.6)$$

where:

$$T_{ij}(k) = P_K\,\alpha_i(K)\,\alpha_j(K)$$

$$\beta_{ij}(k) = \beta_i(K) - \beta_j(K)$$

The expression (B.6) must be averaged over the apertures of the proton and gamma-ray detectors. The first term is independent of ϵ and is unchanged by the averaging procedure. The quantity $8\pi/5$ is the normalization constant which gives the spin-flip probability in terms of the gamma-perpendicular correlation function. The rest of (B.6) may be divided into 'direct' terms, proportional to ϵ^2, and 'interference' terms, proportional to $\epsilon^2 \cos(2\phi_\gamma + \beta_{ij}(\kappa))$. When averaged over the apertures of the proton and gamma-ray detectors, these terms give the acceptance-angle corrections. In this development, the gamma detector is approximated by an 'equivalent' detector of zero thickness and the same intrinsic efficiency situated at the center of the actual cylindrical detector.

The effect of the finite aperture of the proton detector is to define a set of scattering planes whose normals are tilted from the axis of symmetry of the gamma-ray detector (Figure B-1). Let:

ϵ_p = angle of tilt of the normal to a given scattering plane relative to the center of the gamma-ray detector. (B.7)

ϵ_D = half-angle subtended by the gamma-ray detector.

ϵ_γ = integration variable defined in Figure B-1.

Then the edge of the gamma-ray detector referred to the point at which the normal to the scattering plane intersects the surface of the detector is described by the equation of

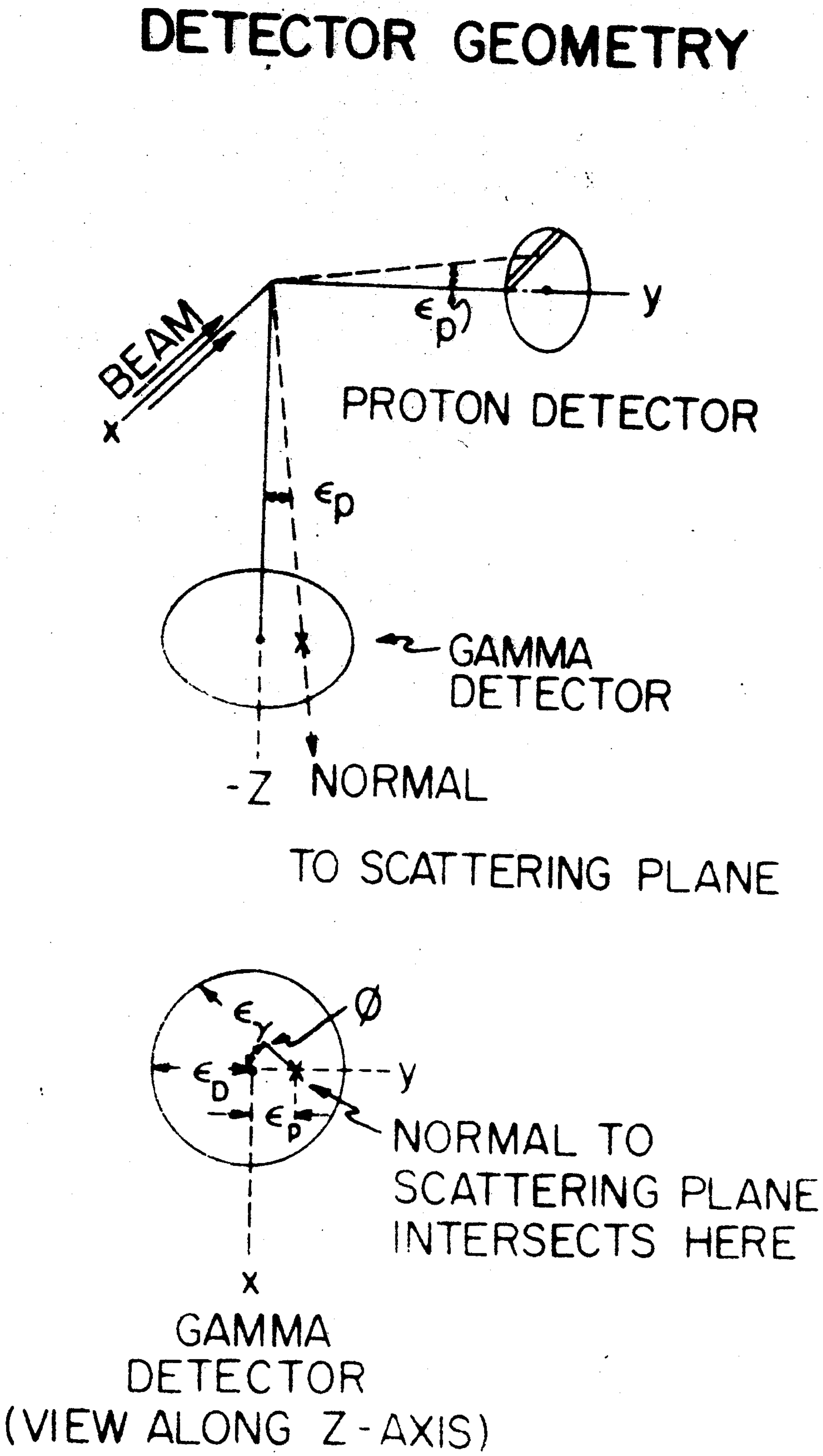
DETECTOR GEOMETRY

GAMMA DETECTOR (VIEW ALONG Z-AXIS)

Figure B-1. Detector geometry for the calculation of the acceptance-angle correction.

an off-center circle in polar coordinates:

$$\epsilon_{\gamma_{max}} = \epsilon_p \cos\varphi + \sqrt{\epsilon_D^2 - \epsilon_p^2 \sin^2\varphi} \qquad \text{(B.8)}$$

The average of the direct terms over the gamma-ray detector is proportional to:

$$\langle\epsilon_\gamma^2\rangle_\gamma = \frac{\int \epsilon_\gamma^2\, d\Omega_\gamma}{\int d\Omega_\gamma} = \frac{1}{\pi\epsilon_D^2}\int_0^{2\pi}\int_0^{\epsilon_{\gamma_{max}}} \epsilon_\gamma^3\, d\epsilon_\gamma\, d\varphi \qquad \text{(B.9)}$$

which reduces to:

$$\langle\epsilon_\gamma^2\rangle_\gamma = \epsilon_p^2 + \frac{\epsilon_D^2}{2} - \frac{1}{8}\,\frac{\epsilon_p^4}{\epsilon_D^2}$$

The interference terms are somewhat more difficult because of the dependence on $\Phi_\gamma = -(\phi + \frac{\pi}{2})$. In this case, the equation of the detector edge is written in the form:

$$\cos\Phi_{\binom{max}{min}} = (\pm)\,\frac{\epsilon_{\gamma max}^2 + \epsilon_p^2 - \epsilon_D^2}{2\epsilon_p\,\epsilon_\gamma}$$

$$\epsilon_{\gamma_{max}} = \epsilon_p + \epsilon_D \qquad \text{(B.10)}$$

Then, the average of the interference terms is:

$$\langle \epsilon_\gamma^2 \cos(2\Phi_\gamma + \beta_{ij}^{(k)}\rangle_\gamma = \frac{1}{\pi\epsilon_D^2}\int_0^{\epsilon_{\gamma max}}\int_{\Phi_{min}}^{\Phi_{max}} \epsilon_\gamma^3 \cos(2\Phi - \beta_{ij}^{(k)})\, d\Phi\, d\epsilon_\gamma \qquad \text{(B.11)}$$

which reduces to:

$$\langle \epsilon_\gamma^2 \cos(2\Phi_\gamma + \beta_{ij}^{(k)})\rangle_\gamma = \epsilon_p^2 \cos\beta_{ij}^{(k)}$$

The expressions (B.9) and (B.11) must now be averaged over the proton detector aperture. For a rectangular aperture, all values of ϵ_p are equally weighted. For a circular aperture of radius ϵ, the weighting is $\sqrt{\epsilon^2-\epsilon_p^2}$. The final results for the direct and interference terms are given in Table (B-1).

The acceptance-angle corrections are determined by substituting these results into (B.6) using the fact that $S_0 + S_1 + S_2 = 1$. For example, for a circular proton (gamma-ray) detector subtending an angle of 2ϵ ($2\epsilon_D$) radians the maximum and minimum values of the correction terms are given by:

$$MAX = -\left(\frac{\epsilon^2}{4}+\frac{\epsilon_D^2}{2}-\frac{1}{64}\frac{\epsilon^4}{\epsilon_D^2}\right)\left(3-\frac{11}{2}S_1\right)-\frac{3}{8}\epsilon^2 S_1-\sqrt{\frac{3}{8}}\,\epsilon^2(1-S_1)$$

$$MIN = -\left(\frac{\epsilon^2}{4}+\frac{\epsilon_D^2}{2}-\frac{1}{64}\frac{\epsilon^4}{\epsilon_D^2}\right)\left(1-\frac{7}{2}S_1\right)+\frac{3}{8}\epsilon^2 S_1 \tag{B.12}$$

where it is assumed that the $\beta_{ij}(k)$ are independent quantities.

Table B-1. Average of direct and interference terms over the acceptance angle of the gamma-ray and proton detectors.

APERTURE [a]	TERM	
	Direct	Interference
RECTANGULAR	$\frac{\epsilon^2}{3} + \frac{\epsilon_D^2}{2} - \frac{1}{40}\frac{\epsilon^4}{\epsilon_D^2}$	$\frac{1}{3}\epsilon^2 \cos\beta_{ij}^{(k)}$
CIRCULAR	$\frac{\epsilon^2}{4} + \frac{\epsilon_D^2}{2} - \frac{1}{64}\frac{\epsilon^4}{\epsilon_D^2}$	$\frac{1}{4}\epsilon^2 \cos\beta_{ij}^{(k)}$

a) Refers to the proton-detector aperture. The quantity ϵ equals half the height for a rectangular aperture, and is equal to the radius for a circular aperture. The gamma-ray detector is assumed to be circular, with radius ϵ_D, in all cases.

APPENDIX C

DERIVATION OF THE FORM FACTOR IN THE QUASI-PARTICLE MODEL

The form factor is proportional to the reduced matrix element:

$$< J \| V_{\ell s j} \; T_{\ell s j} \| 0 > \tag{C.1}$$

taken between the initial and final nuclear states which are to be described as quasi-particle states (Yo 62). Applying the Wigner-Eckart theorem (Me 65):

$$< J \| V_{\ell s j} \; T_{\ell s j} \| 0 > = < J \, M_J | V_{\ell s j} \; T_{\ell s j}^{M_J} | 0 > \tag{C.2}$$

The single-particle operator $V_{\ell s j} \; T_{\ell s j}^{M_J}$ may be written in second-quantization notation (Ma 65):

$$V_{\ell s j} \; T_{\ell s j}^{M_J} = \sum_{\substack{jj' \\ mm'}} < j'm' | V_{\ell s j} \; T_{\ell s j}^{M_J} | jm > a^{\dagger}_{j'm'} \, a_{jm} \tag{C.3}$$

where a^{+}_{jm} (a_{jm}) creates (destroys) a particle in the shell-model orbital jm.

The transition to the quasi-particle formalism is accomplished through the Boguliubov-Valatin transformation (Bo 58, Bo 58a, Va 58):

$$a_{jm} = U_j \alpha_{jm} + (-)^{j-m} V_j \alpha^{+}_{j-m} \quad . \tag{C.4}$$

where α^{+}_{jm} (α_{jm}) creates (destroys) a quasi-particle with quantum numbers jm, and U_j and V_j are the usual occupation parameters (Ba 63). Substituting into (C.3) we find:

$$V_{lsj} T^{M_J}_{lsj} = \sum_{\substack{jj' \\ mm'}} < j'm' | V_{lsj} T^{M_J}_{lsj} | jm > \tag{C.5}$$

$$\times \left[U_{j'} V_j (-)^{j-m} \alpha^{+}_{j'm'} \alpha^{+}_{j,-m} + V_{j'} U_j (-)^{j'-m'} \alpha_{j',-m'} \alpha_{jm} \right]$$

+ (terms which have zero matrix element between the ground state and the two quasi-particle excited states).

Following Yoshida (Yo 62), the two quasi-particle operators are defined by:

$$A^{+}(j_1 j_2 JM) = \sum_{m_1 m_2} < j_1 j_2 m_1 m_2 | JM > \alpha^{+}_{j_1 m_1} \alpha^{+}_{j_2 m_2}$$

$$A(j_1 j_2 JM) = \sum_{m_1 m_2} < j_1 j_2 m_1 m_2 | JM > \alpha_{j_2 m_2} \alpha_{j_1 m_1} \tag{C.6}$$

In terms of these operators:

$$V_{lsj} T^{M_J}_{lsj} = \sum_{jj'} \hat{j}' \hat{J}^{-1} < j' \| T_{lsj} \| j > < j' | V_{lsj} | j > \tag{C.7}$$

$$\times \left[U_{j'} V_j A^{+}(j'j JM_J) + V_{j'} U_j (-)^{J+M_J} A(j'j J,-M_J) \right]$$

where $\hat{j} = \sqrt{2j+1}$. The matrix element $\langle j' | V_{\ell s j} | j \rangle$ is a radial integral of the interaction potential taken between shell model states which are assumed to be harmonic oscillator wave functions.

Next the phonon creation operator is defined:

$$Q^{+}_{JM_J} = \frac{1}{2} \sum_{j_1 j_2} \left[\psi^{J}_{j_1 j_2} A^{+}(j_1 j_2 J M_J) - \phi^{J}_{j_1 j_2} (-)^{J-M_J} A(j_1 j_2 J, -M_J) \right] \tag{C.8}$$

where $\psi^{J}_{j_1 j_2}$ and $\varphi^{J}_{j_1 j_2}$ are normalization coefficients (Yo 62). Then:

$$A^{+}(j' j J M_J) = (-)^{J-M_J} \varphi^{J}_{j' j} Q_{J,-M_J} + \psi^{J}_{j' j} Q^{\dagger}_{JM_J}$$

$$A(j' j J M_J) = \psi^{J}_{j' j} Q_{JM_J} + (-)^{J-M_J} \varphi^{J}_{j' j} Q^{+}_{J,-M_J} \tag{C.9}$$

so that:

$$V_{\ell s j} T^{M_J}_{\ell s j} = \sum_{jj'} \hat{j}' \hat{J}^{-1} \langle j' \| T_{\ell s j} \| j \rangle \langle j' | V_{\ell s j} | j \rangle$$

$$\times \left[\psi^{J}_{j' j} U_{j'} V_{j} + \varphi^{J}_{j' j} V_{j'} U_{j} \right] Q^{\dagger}_{JM_J} \tag{C.10}$$

+ (phonon destruction terms).

The Q operators satisfy the boson commutation relations:

$$[Q_{JM}, Q^{+}_{J'M'}] = \delta_{JJ'} \delta_{MM'} \tag{C.11}$$

and the one-phonon excited states $|JM_J\rangle$ are given by:

$$|JM_J\rangle = Q^{+}_{JM_J} |0\rangle \tag{C.12}$$

where $|0\rangle$ is the ground state (phonon vacuum). Thus, the reduced matrix element (C.1) is:

$$\langle J \| V_{\ell sj} T_{\ell sj} \| 0\rangle = \sum_{j_1 j_2} \hat{j}_1 \hat{J}^{-1} \langle j_1 \| T_{\ell sj} \| j_2\rangle$$

$$\times \langle j_1 | V_{\ell sj} | j_2\rangle \left[\psi^{J}_{j_1 j_2} U_{j_1} V_{j_2} + \phi^{J}_{j_1 j_2} V_{j_1} U_{j_2} \right] \tag{C.13}$$

A FORTRAN-IV code has been written to calculate the reduced matrix element (C.13). The normalization coefficients $\psi^{J}_{j_1 j_2}$ and $\phi^{J}_{j_1 j_2}$ were computed according to the work of Yoshida. The values obtained were checked by comparing to the data given in (Yo 62), and found to be in good agreement.

REFERENCES

Ba 57 M.K. Banerjee and C.A. Levinson, Ann. of Phys. 2, 499 (1957).

Ba 62 R.H. Bassel, R.M. Drisko, and G.R. Satchler, Oak Ridge National Laboratory Report ORNL-3240 (1962) unpublished.

Ba 62a R.H. Bassel, G.R. Satchler, R.M. Drisko, and E. Rost, Phys. Rev. 128, 2693 (1962).

Ba 63 M. Baranger, in the Cargese Summer School Lectures (W.A. Benjamin, 1963).

Ba 64 R.H. Bassel, R.M. Drisko, G.R. Satchler, L.L. Lee, J.P. Schiffer, and B. Zeidman, Phys. Rev. 136, B960 (1964).

Be 66 R.E. Bell, Nucl. Inst. Methods 42, 211 (1966).

Bi 53 L.C. Biedenharn and M.E. Rose, Rev. Mod. Phys. 25, 729 (1953).

Bl 52 J.M. Blatt and V.F. Weisskopf, Theoretical Nuclear Physics (John Wiley and Sons, Inc., 1952).

Bl 61 J.S. Blair and L. Wilets, Phys. Rev. 121, 1493 (1961).

Bl 66 H.G. Blosser and A.I. Galonsky, IEEE Trans. Nucl. Sci., NS-B, No. 4, 466 (1966).

Bl 66a L.N. Blumberg, E.E. Gross, A. VanDerWoude, A. Zucker, and R.H. Bassel, Phys. Rev. 147, 812 (1966).

Bo 58 N.N. Boguliubov, J. Exptl. Theoret. Phys. 34, 58 (1958).

Bo 58a N.N. Boguliubov, Nuovo Cimento 7, 843 (1958).

Bo 59 A. Bohr, Nucl. Phys. 10, 486 (1959).

Br 61 T.H. Braid, J.L. Yntema, and B. Zeidman, Argonne National Laboratory Report ANL-6358, p.11 (1961) unpublished.

Br 62 D.M. Brink and G.R. Satchler, Angular Momentum (Oxford University Press, 1962).

Ch 61 R.L. Chase, Nuclear Pulse Spectrometry (McGraw-Hill Book Company, Inc., 1961).

Cr 64 R.M. Craig, J.C. Dore, G.W. Greenlees, J.S. Lilley, and J. Lowe, Nucl. Phys. 58, 515 (1964).

Cr 66 R.M. Craig, J.C. Dore, G.W. Greenlees, J. Lowe, and D.L. Watson, Nucl. Phys. 79, 177 (1966).

Cr 66a R.M. Craig, J.C. Dore, G.W. Greenlees, J. Lowe, and D.L. Watson, Nucl. Phys. 83, 493 (1966).

Da 58 A.S. Davydov and G.F. Filippov, Nucl. Phys. 8, 237 (1958).

DeB 64 S. DeBenedetti, Nuclear Interactions, (John Wiley and Sons, Inc., 1964).

Di 63 J.K. Dickens, D.A. Haner, and C.N. Waddel, Phys. Rev. 132, 2159 (1963).

Ee 68 J. Eenmaa, T.D. Hayward, W.A. Kolasinski, R.H. Lewis, D.M. Patterson, F.H. Schmidt, and J.R. Tesmer, University of Washington Nuclear Physics Laboratory Report (1968) unpublished.

Ev 55 R.D. Evans, The Atomic Nucleus (McGraw-Hill Book Company, Inc., 1955).

Fa 67 J.A. Fannon, E.J. Burge, D.A. Smith, and N.K. Ganguly, Nucl. Phys. A97, 263 (1967).

Fr 67 M.P. Fricke, E.E. Gross, and A. Zucker, Phys. Rev. 163, 1153 (1967).

Fu 68 S.A. Fulling and G.R. Satchler, Nucl. Phys. A111, 81 (1968).

Gi 64 V. Gillet and N. Vinh Mau, Nucl. Phys. 54, 321 (1964).

Gi 68 R.O. Ginaven, E.E. Gross, J.J. Malanify, and A. Zucker, Phys. Rev. Letters 21, 552 (1968).

Gl 65 C.M. Glashausser, thesis (Princeton University, 1965) unpublished.

Gl 67 C. Glashausser, R. DeSwiniarski, and J. Thirion, Phys. Rev. 164, 1437 (1967).

Go 62 L.J.B. Goldfarb and D.A. Bromley, Nucl. Phys. 39, 408 (1962).

Gr 66 R.J. Griffiths, E.A. McClatchie, A.R. Johnston, and W.R. Gibson, Nucl. Inst. Methods 40, 181 (1966).

Gr 66a G.W. Greenlees and G.J. Pyle, Phys. Rev. 149, 836 (1966).

Gr 67 A.M. Green, Phys. Letters 24B, 384 (1967).

Ha 62 T. Hamada and I.D. Johnston, Nucl. Phys. 34, 383 (1962).

Hr 67 A.Z. Hrynkiewicz, S. Kopta, S. Szymczyk, and T. Wolczak, Nucl. Inst. Methods 49, 229 (1967).

Jo 63 P.B. Jones, The Optical Model in Nuclear and Particle Physics (Interscience Publishers, 1963).

Jo 66 M.B. Johnson, L.W. Owen, and G.R. Satchler, Phys. Rev. 142, 748 (1966).

Ka 64 A. Kallio and K. Kolltveit, Nucl. Phys. 53, 87 (1964).

Ke 59 A.K. Kerman, H. McManus, and R.M. Thaler, Ann. of Phys. 8, 551 (1959).

Kl 53 E.D. Klema and F.K. McGowan, Phys. Rev. 91, 616 (1953).

Ko 67 R.L. Kozub, thesis (Michigan State University, 1967) unpublished.

Ko 67a W.A. Kolasinski, thesis (University of Washington, 1967) unpublished.

La 53 J.S. Lawson and H. Frauenfelder, Phys. Rev. 91, 649 (1953).

La 62 K.E. Lassila, M.H. Hull, Jr., H.M. Ruppel, F.A. McDonald, and G. Breit, Phys. Rev. 126, 881 (1962).

La 67 A. Lande and J.P. Svenne, Phys. Letters 25B, 91 (1967).

Lo 68 FORTRAN-IV computer code written by P. Locard (Michigan State University, 1968) unpublished.

Ma 65 V.A. Madsen and W. Tobocman, Phys. Rev. 139, B870 (1965).

Ma 67 G.H. Mackenzie, E. Kashy, M.M. Gordon, and H.G. Blosser, IEEE Trans. Nucl. Sci. 14, 450 (1967).

Mc 67 H. McManus, F. Petrovich, and D. Slanina, Bull. Am. Phys. Soc. 12, 12 (1967).

Mc 69 H. McManus and F. Petrovich, private communication and to be published.

Mc 69a H. McManus, private communication.

Me 65 A. Messiah, Quantum Mechanics (John Wiley and Sons, Inc., 1965).

Pa 68 D.M. Patterson and J.G. Cramer, Phys. Letters 27B, 373 (1968).

Pa 69 R.A. Paddock, S.M. Austin, W. Benenson, I.D. Proctor, and F. St.Amant, Phys. Rev. (to be published).

Pe 64 F.G. Perey and D.S. Saxon, Phys. Letters 10, 107 (1964).

Pe 67 F. Petrovich, D. Slanina, and H. McManus, Michigan State University Report MSPT-103 (1967) unpublished.

Pe 68 FORTRAN-IV computer code written by F. Petrovich, (Michigan State University, 1968) unpublished.

Pr 68 B.M. Preedom, private communication.

Ra 67 R. Raj, Y.K. Gambir, and M.K. Pal, Phys. Rev. 163, 1004 (1967).

Ri 64 B.W. Ridley and J.F. Turner, Nucl. Phys. 58, 497 (1964).

Ri 64a B.W. Ridley, J.F. Turner, and J.C. Kerr, Rutherford High Energy Laboratory Report NIRL/R/81 (1964) unpublished.

Ro 61 L. Rosen, J.E. Brolley, Jr., and L. Stewart, Phys. Rev. 121, 1423 (1961).

Sa 55 G.R. Satchler, Proc. Phys. Soc. A68, 1037 (1955).

Sa 60 G.R. Satchler and W. Tobocman, Phys. Rev. 118, 1566 (1960).

Sa 64 G.R. Satchler, Nucl. Phys. 55, 1 (1964).

Sa 66 G.R. Satchler, Nucl. Phys. 77, 481 (1966).

Sa 67 G.R. Satchler, Nucl. Phys. A100, 497 (1967).

Sa 67a G.R. Satchler, Nucl. Phys. A95, 1 (1967).

Sa 67b G.R. Satchler, Nucl. Phys. A92, 273 (1967).

Sc 64 F.H. Schmidt, R.E. Brown, J.B. Gerhart, and W.A. Kolasinski, Nucl. Phys. 52, 353 (1964).

Sh 68 H. Sherif and J.S. Blair, Phys. Letters 26B, 489 (1968).

Sn 66 J.L. Snelgrove and E. Kashy, Nucl. Inst. Methods 52, 153 (1966).

St 58 P.H. Stelson and F.K. McGowan, Phys. Rev. 110, 489 (1958).

To 61 W. Tobocman, Theory of Direct Nuclear Reactions (Oxford University Press, 1961).

Va 58 J.G. Valatin, Nuovo Cimento 7, 843 (1958).

Yo 60 H. Yoshiki, Phys. Rev. 117, 773 (1960).

Yo 62 S. Yoshida, Nucl. Phys. 38, 380 (1962).